Processing and interpretation of satellite and terrestrial gravity data for the lithospheric structure of Egypt and the Saharan Metacraton

Dissertation
zur Erlangung des akademischen Grades
eines Doktors der Naturwissenschaften (Dr. rer. nat.)
der Mathematisch-Naturwissenschaftlichen Fakultät
der Christian-Albrechts-Universität zu Kiel

vorgelegt von

Mohamed Sobh Emam Mohamed Salem

Kiel, April 2019

Institut für Geowissenschaften
Abteilung Geophysik

Erstgutachter:	Prof. Dr. Jörg Ebbing
Zweitgutachter:	Prof. Dr. Hans-Jürgen Götze
Tag der Disputation:	16. April 2019
Zum Druck genehmigt:	
gez. Prof. Dr. Lutz Kipp, Dekan	

Declaration

I hereby certify that this thesis is my own composition, except the German abstract, which was translated by Peter Haas, all sources have been acknowledged, and my contribution to the thesis is clearly identified. The thesis has not previously been submitted or accepted for a degree at this or another institution. I certify that the work has been undertaken in compliance with the rules of good academic practice of the German Research Foundation.

Ort, Datum	Mohamed Sobh Salem

Abstract

A reliable density structure modelling is essential for a good lithospheric study that is, in turn, a milestone to understand the geodynamics of the study region. Achieving such a reliable model is limited by the availability of a high-quality regional gravity field developed merging together heterogeneous gravity data acquired by various observational techniques whose spectral content, coverage, and spatial resolution are not the same. On the other hand, the global geopotential models derived from satellite observations can only contribute to the long wavelength signal. This study presents a recent combined regional gravity field model over Egypt, developed by integrating satellite and terrestrial data via applying the remove-compute-restore principle and the least-squares collocation procedure.

For the development of the combined gravity model, the long wavelength signal from the GOCE satellite-only model computed with the space-wise solution has been integrated with the terrestrial data retrieved from approximately 56000 gravity stations of the Getech data, acquired in the framework of the African Gravity Project. Ultimately, the combined gravity model is used to prepare a comprehensive three-dimensional model of the crustal density structure for Egypt in order to mapping the Moho depths.

The 3D crustal density model for Egypt is constraining by available deep seismic refraction, receiver functions analysis, borehole, and geological information. In Egypt, seismic data are sparsely and irregularly distributed. Consequently, we developed the crustal thickness model by integrating seismic and gravity data. Satellite gravity data was inverted to build an initial model, which was followed by a detailed 3D forward gravity modelling. The initial crustal thickness is determined by applying seismically constrained non-linear inversion. Moreover, the gravity inversion-based Moho depth estimates are in good agreement with results of seismic studies and are exploited for the 3D forward modelling. The developed 3D crustal thickness model provides high-resolution Moho depth estimates that closely resembles the major geological and tectonic features.

The model part of the thesis was linked to the tectonics of Egypt with the regional North Africa enigmatic tectonic unit "Saharan Metacraton" by study the underlying (deep) structures. We model variations in the crustal and lithospheric thickness as well as variation in temperature, composition, S-wave seismic velocity and density of the lithosphere beneath the Saharan Metacraton using three-dimensional (3D) integrated petrological-geophysical modelling. The Saharan Metacraton was once an intact Archean-Paleoproterozoic craton, but was remobilized (metacratonized) during the Neoproterozoic due to partial loss of its sub-continental lithospheric mantle

(SCLM) during collisions along its margin. The partial loss of the SCLM might have allowed for the preservation of cratonic remnants within the metacraton.

We discuss the possible preserved three cratonic remnants within the Saharan Metacraton by integrated modelling using geophysical, petrological and geological information for the crust and the lithospheric mantle. The cratonic remnants are overlain by Paleozoic-Mesozoic sedimentary basins and are surrounded and separated by topographic swells with known Cenozoic volcanism including the Hoggar Swell, the Tibesti Massif, and the Darfur Dome. We find that the three cratonic remnants are underlain by a relatively thicker lithosphere (the thickest being beneath Al-Kufra reaching $\sim$ 200 km) compared to the surrounding Saharan Metacraton which has an average lithospheric thickness of $\sim$ 150 km. We also find that the SCLM of the cratonic remnants to be relatively colder and denser, as seen by faster S-wave velocity compared to the surrounding Saharan Metacraton. Our preferred model is approached with considering different lithospheric thickness beneath the Saharan Metacraton with uniform moderately depleted composition (Proterozoic SCLM composition). We suggest that the presence of relatively thinner lithosphere beneath the Saharan Metacraton outside the cratonic remnants was due to a combination of Precambrian events (partial SCLM delamination during the Neoproterozoic) and Phanerozoic events (Mesozoic-Cenozoic rifting and Cenozoic mantle volcanism).

Zusammenfassung

Eine zuverlässlige Modellierung der Dichtestruktur ist Grundlage für ein fundiertes Studium der Lithosphäre. Dieses ist wiederum unerlässlich für das Verständnis der Geodynamik im jeweiligen Untersuchungsgebiet. Die Entwicklung eines verlässlichen Modells hängt von der Verfügbarkeit eines qualitativ hochwertigen, regionalen Schwerefeldes ab. Dieses muss aus verschiedenen heterogenen Beobachtungsdaten Zusammengefügt werden, deren Spektralgehalt, Abdeckung und räumliche Auflösung oft unterschiedlich sind. Auf der anderen Seite können die aus Satellitenbeobachtungen abgeleiteten globalen Potentialmodelle nur zum langwelligen Signal beitragen. Diese Studie präsentiert ein neues kombiniertes Regional-Schweremodell für Ägypten, welches durch die Integration von Satelliten- und terrestrischen Daten unter Anwendung des "Remove-Compute-Restore" Prinzips und der Kollokation nach kleinsten Fehlerquadraten bestimmt wurde.

Für die Entwicklung des kombinierten Schweremodells wurde zunächst das langwellige Signal des Schwerefeldes verwendet, das ausschließlich aus den Beobachtungen des GOCE Satelliten berechnet wurde (satellite-only model mit flächenhafter Lösung); es wurde mit einem terrestrischen Datensatz von 56.000 Schweremessungen der Firma "Getech" gemischt, die im Rahmen des "African Gravity Project" erhoben wurden. Schließlich wird dieses kombinierte regionale Schweremodell genutzt, um ein umfangreiches dreidimensionales Modell der Krusten-Dichtestruktur in Ägypten zu erstellen, das auch die Tiefe der Moho abbildet.

Das 3D Dichtemodell der Kruste in Ägypten wird mit verfügbaren Informationen aus tiefen seismischen Refraktionsmessungen, aus der Analyse von "receiver-functions", Bohrlochdaten und geologischen Informationen abgesichert. In Ägypten sind seismische Daten nur spärlich vorhanden und unregelmäßig verteilt. Aus diesem Grund wurde die Krustenmächtigkeit durch die Kombination von seismischen und gravimetrischen Daten ermittelt. Dazu wurden die Satellitendaten invertiert, um ein Anfangsmodell zu generieren. Später folgte eine detaillierte 3D Vorwärtsmodellierung der Schwere. Die initiale Krustenmächtigkeit wurde durch Daten aus einer nichtlinearen Inversion der Seismik abgesichert. Der durch Schwereinversion bestimmte Verlauf der Moho ist in guter Übereinstimmung mit den Ergebnissen der seismischen Untersuchungen und wird für die 3D Vorwärtsmodellierung weiter verwendet. Das 3D Krustenmodell zeigt eine hochaufgelöste Tiefenstruktur der Moho, die die wesentlichen geologischen und tektonischen Merkmale abbildet.

Im "Modellierteil" der Arbeit wird die Tektonik der tieferliegenden Schichten Ägyptens verknüpft mit dem tektonisch enigmatischen "Sahara Metakraton" im Norden Afrikas. Dabei werden die Variationen der Krusten- und Lithosphärenmächtigkeit,

sowie der Temperatur, Komposition, S-Wellen Geschwindigkeit und Lithosphärendichte unter dem "Sahara Metakraton" durch die Anwendung einer 3D petrologisch-geophysikalischen Modellierung modelliert. Ursprünglich war der Sahara Metakraton ein intakter archaisch-paläoproterozoischer Kraton. Aufgrund des partiellen Verlusts seines subkontinentalen lithosphärischen Mantels (SCLM) wurde er während des Neoproterozoikums remobilisiert bzw. "meta-kratonisiert"; verursacht wurde dies durch eine Kollisionen entlang des ehemaligen Kontinentalrands.

Der partielle Verlust des SCLM könnte die Konservierung kratonaler Relikte innerhalb des Metakratons begünstigt haben. Die Existenz dieser möglicherweise noch bestehender Reste im Bereich des "Sahara Metakratons" wird mit Hilfe einer integralen Modellierung auf der Grundlage von geophysikalischen, petrologischen und geologischen Informationen über die Kruste und den lithosphärischen Mantel untersucht. Die kratonalen Relikte sind von paläozoisch-mesozoischen Sedimentbecken überlagert und von topografischen Erhebungen markiert, die im Zusammenhang mit dem känozoischen Vulkanismus stehen: hierzu zählt das Ahaggar-Gebirge, Tibesti und Darfur Dome. Es konnte nachgewiesen werden, dass die drei kratonalen Überreste mit einer relativ dicken Lithosphäre unterlagert sind (mit der größten Mächtigkeit von ca. 200 km unter Al-Kufra). Im Vergleich dazu beträgt die durchschnittliche Mächtigkeit der Lithosphäre im "Sahara Metakraton" etwa 150 km. Außerdem ergaben die Untersuchungen, dass der subkontinentale lithosphärische Mantel im Kraton-Bereich relativ kalt und dicht ist. Dies konnte aus der höheren S-Wellengeschwindigkeit im Vergleich zum umliegenden "Sahara Metakraton" abgeleitet werden.

In dem bevorzugten Modell besteht unterhalb des Sahara Metakratons also eine unterschiedliche Lithosphärenmächtigkeit mit einer gleichförmig moderat abgereicherten Komposition (die proterozoische SCLM-Komposition). Es wird vorgeschlagen, dass das Vorhandensein der relativ dünnen Lithosphäre unterhalb des "Sahara Metakratons" außerhalb der kratonalen Überreste auf zeitlich verschiedene Ereignisse zurückzuführen ist: im Präkambrium auf eine teilweise Delamination des subkontinentalen lithosphärischen Mantels im Zeitalter des Neoproterozoikums und später durch phanerozoische Prozesse wie dem mesozoisch- känozoischen Rifting und känozoischen Mantelvulkanismus.

Acknowledgements

All praise is due to Almighty God for his guidance and helping me to bring forth the present study.

First and more foremost I would like to express my sincere appreciation and thanks to my supervisors Prof. Dr. Jörg Ebbing and Prof. Dr. Hans-Jürgen Götze for their instant guidance and kind supervision at the highest standards during my study. Your advice, discussions, critical comments have shaped this thesis and dramatically improved my research and academic skills. Jörg, I would like to thank you for encouraging me to explore research areas that I feel most interested in, and to broaden my scientific vision through participating in conferences and workshops. Hajo, thank you for always taking the time to meet and for providing the encouragement I needed, your unlimited patience in our discussion.

I would like to describe my sincere gratitude to Prof. Dr. Mohamed Abdelsalam for his valuable comments and discussions on the Saharan Metacraton tectonics. I am also grateful to Dr. Sabine Schmidt for her assistance with the IGMAS+ software. Thanks should also go to Folker Pappa for helpful discussions in LitMod3D.

I would like to thank Eva Bredow and Wolfgang Szwillus for proofreading my thesis and their valuable comments. Peter Haas, I want to thank you for translating my abstract into German, excellent work.

Special thanks to all members of the Satellite and Aerogeophysics working Group. Andreas, it was great to share the same office with you. Thank you guys for the nice time and the lively discussions during the coffee breaks and at lunchtime.

I would like also to thank Getech, UK for providing the terrestrial gravity data over Egypt. I want to acknowledge the German Academic Exchange Service (DAAD) for funding my stay at CAU-Kiel through the grant (DAAD-57030312).

My deep gratitude goes to all staff members and my researcher assistant friends of Geodynamics Department, National Research Institute of Astronomy and Geophysics (NRIAG), Cairo, Egypt. Special thanks are to my colleagues Dr. Basem El-Saka, Karem Abdelmohsen, Dr. Nadia AbouAly for their help and encouragement to finish this study. My sincere gratitude goes to my dear friend Ahmed Hamdi Mansi for our great and productive collaborations.

I would like to express appreciation for the support I have received over the duration of my PhD journey to my friends Amr El-sharkawy and Islam Fadel.

Finally, special thanks go to my family especially my parents for their encouragement and support, I owe you everything. To my wife, Shaimaa, thank you for your love and inspiration, for being so understanding and putting up with me through this tough journey. To my two lovely children, Omar and Loreen, I love you more than anything and I appreciate all your patience and support during my Ph.D. journey.

Contents

List of Figures

List of Tables

Chapter 1

Introduction

High-resolution gravity field interpretations became of greater importance for both geophysical and geodynamical models of the Earth. Such a high-resolution gravity model is typically compiled from terrestrial gravity measurements. However, they are not always available with suitable coverage. Today, terrestrial gravity data are supplemented by equally high-resolution gravity fields from satellite gravimetry, which also allow the modelling of the gravity potential at a more regional scale. This information allows also large-scale interpretation due to the long wavelengths which are imaged in these fields. In this thesis, interdisciplinary three-dimensional modelling approaches are used for static and kinematic interpretations of the lithospheres of North Africa. The quality and coverage of the terrestrial gravity data for the North Africa region as a whole were considered insufficient as it limited to a specific area. Focusing on Egypt, since I have access to the consistent terrestrial gravity data which covering most part of the Egyptian territory provided by the GETECH (Geophysical Exploration Technology). However, these terrestrial gravity data over Egypt suffer data gaps as well as being heterogeneously distributed, which lead to a low-resolution gravity field model, which, in turn, is not practical for a reliable density structure modelling. Consequently, for Egypt and similar regions (e.g., the entire North Africa area), there is a persistent need to develop high-resolution regional combined gravity models based, mainly, on the terrestrial gravity data that have recently become available. In the framework of my PhD thesis these studies were carried out in the research group "Satellite- and Aerogeophysics" at Christian-Albrechts-University in Kiel, because their members have many years of experience in gravity data processing and the interpretation of large-scale tectonic structures, as well as many years of experience in the acquisition of satellite gravity data.

For the development of the combined gravity model, the long wavelength signal from GOCE satellite-only model developed with the space-wise solution has been integrated with the terrestrial data retrieved from approximately 56000 gravity stations of the Getech data, acquired in the framework of the African Gravity Project (Fairhead et al., 1988). The newly combined gravity model was used to build a detailed density model for Egypt in order to mapping the Moho depths. GOCE satellite gravity data is inverted in order to build an initial crustal thickness map precedent to performing a detailed, three-dimensional density model of Egypt constrained by available deep seismic refraction, receiver functions analysis, borehole, and geological information. This model was prepared by using the Interactive Geophysical

Modelling Assistant (IGMAS+) software, which is a 3D geo-modelling package developed based on the simultaneous forward modelling of gravity, gravity gradients, and magnetic fields (Götze and Lahmeyer, 1988; Schmidt et al., 2010; Alvers et al., 2014; Alvers et al., 2015; Schmidt, Barrio-Alvers, and Götze, 2015). In general, high-resolution mapping of Moho depths is fundamental and results in a better understanding of the geometrical structure of the subsurface and the geodynamical evolution of the study area and, consequently, it can be used for both the prediction and mitigation of geohazards, e.g., earthquakes. Moreover, the knowledge of a precisely modelled crust would increase the potential to target and extract natural resources as well as to understand regional dynamics. A better understanding of the deep structures can help to improve also heat flow modelling and the prediction of source rock maturity and hydrocarbon accumulations (Allen and Allen, 2005; Hantschel and Kauerauf, 2009; Bouman et al., 2015).

From the theoretical viewpoint, each interpretation of gravity data is ambiguous. Therefore, it is an important concern of the presented thesis to find data constraints for the forward modelling and data inversion: thus data of deep seismic refraction, wide-angle reflection, receiver functions, and ambient noise tomography have been compiled from recent publications and a few from fieldwork. Temperature and the composition of the lithosphere are key parameters in modern lithospheric modelling, since they determine the physical properties (elasticity, rheology, density, etc.) which control the dynamics of the Earth's interior. The modelling in the present work is based on both static interactive forward modelling techniques and integrated geophysical-petrological methodology. Elevation, geoid, gravity, its gradients, surface heat flow, and seismic and upper mantle petrological data will be combined and interpreted simultaneously and compared with results of earlier modelling.

The model part of the thesis was linked to the tectonics of Egypt with the regional North Africa enigmatic tectonic unit "Saharan Metacraton" by study the underlying (deep) structures in the crust and upper mantle. In general, cratons are stable tectonic units that have not been affected by major tectonic or magmatic events for a long time, possibly since the time of their formation (e.g., (Black and Liégeois, 1993)). The stability of cratons has been largely attributed to the presence of thick, cold, depleted and anhydrous sub-continental lithospheric mantle that is isolated from the surrounding convecting mantle. However, it has been realized that cratons can lose their long-lasting stability through geodynamic processes leading to their total destruction (referred to as decratonization by (Yang et al., 2008) or partial destruction (referred to as metacratonization by (Abdelsalam, Liégeois, and Stern, 2002)). The Saharan Metacraton is a former craton that has been remobilized during tectonic and/ or thermal events but can still be recognized through its rheological, geochronological and isotopic characteristics (Abdelsalam, Liégeois, and Stern, 2002). It was once an intact Archean-Paleoproterozoic craton but was remobilized (metacratonized) during the Neoproterozoic due to partial loss of its sub-continental lithospheric mantle during collisions along its margin. The partial loss of the sub-continental lithospheric mantle might have allowed for the preservation of cratonic remnants within the metacraton. Consequently, the three-cratonic blocks (Al-Kufra, Murzuq, and Chad) are escaped the metacratonization process and preserved as cratonic remnants.

In terms of the origin and development of the Saharan Metacraton lithosphere, there are some challenging questions: Are we able to model these three cratonic remnants? Are these cratonic blocks different from the density and temperature properties than the surrounding Metacraton? At which depth can we still model the three cratonic remnants? How compatible are our model with the recent seismic tomography model?

What is the role of the thermal anomaly for cratonic modifications along the Saharan Metacraton? The presence of magmatism along the cratonic blocks boundaries, where the Cenozoic volcanic field is present might have induced the process that modified the lithospheric mantle beneath the SMC, which may finally lead to the gravitational instability and destruction of the lower part of the lithosphere (Fezaa et al., 2010; Liégeois et al., 2013). Moreover, a high-temperature anomaly is imaged around the cratonic blocks within the SMC and its distribution correlates well with the location of the recent volcanism in the region. This anomaly seems to be related to the upwelling of the sub-lithospheric material, which creates forced downwellings and erosion of the basal parts of the lithosphere.

At present, there is no general agreement as to the actual causes, processes, and extent of lithospheric modification associated with the removal/modification of the SCLM beneath SMC (Abdelsalam, Liégeois, and Stern, 2002). Proposed geodynamic models include, but are not limited to delamination of cratonic root (Lemnifi et al., 2017), thermomechanical erosion due to asthenospheric upwelling, to that the craton was subjected to collisional events in the Neoproterozoic along its entire margins and potential mantle plumes in the underlying asthenosphere (Burke, 1996). In order to answer these questions, we study the density, thermal, and compositional structure of the Saharan Metacraton lithosphere. A model of the thermal and compositional structure of the lithosphere provides crucial information for understanding the present-day lithospheric features and geodynamic processes. Therefore, a reliable crustal structure model needs to be defined throughout the modelling process.

Thesis objectives

This thesis has the following major objectives:

- Compile and homogenize the existing gravity database for Egypt.
- Develop a combined regional gravity field model of Egypt which can serve as a base of geodetic and geophysical applications.
- Build a detailed 3D density model for Egypt from the high-resolution gravity data, constraining with the available seismic data (e.g., Receiver function, deep seismic profiles) and geological information.
- Providing a 3D crustal and lithospheric thickness map of the area of Egypt and Saharan Metacraton that are consistent with the available seismic data and tomography models.

- Modelling the lithospheric mantle structure, combining geophysical and petrological data. This task will allow the characterization of the lithospheric mantle in the Saharan Metacraton, through the definition of the geometry of the lithosphere-asthenosphere boundary, mantle compositional variations, and distribution of mantle temperature, density, and seismic velocity anomalies.
- Understanding the regional lithospheric structure of SMC with related to the geodynamic history of the region.

Thesis Structure

This thesis includes five chapters, three main chapters in addition to the introduction and conclusion. Each chapter includes a published or ready for submission manuscript; a brief outline of each chapter is given here:

Chapter 1 represents the research framework of the thesis and the research objectives. It also includes a description of the thesis structure.

Chapter 2 presents the development of the combined regional gravity model by integrating satellite and homogenous terrestrial data applying the remove-compute-restore technique and least-square collocation procedure. The study presented here is from an article published in Pure and Applied Geophysics (Sobh et al., 2018).

Chapter 3 discuss how the crustal thickness model of Egypt was developed based on the gravity inversion and 3D forward gravity modelling. This chapter is written based on a published paper in Tectonophysics (Sobh et al., 2019).

Chapter 4 presents the density, thermal, compositional, and velocity structure of the Saharan Metacraton lithosphere through an integrated petrological-geophysical modelling using LitMod3D. This chapter is based on a manuscript in preparation.

Chapter 5 provides the main conclusions of the dissertation. Additionally, it discusses the suggestions for the future directions of research.

Contributions

The two published manuscripts and the other manuscript, which is ready for submission, form the core of this thesis and constitute the main scientific effort developed therein.

Manuscript I (Sobh et al., 2018): Regional Gravity Field Model of Egypt Based on Satellite and Terrestrial Data. Pure Appl. Geophys. 2018, 1–20.
https://doi.org/10.1007/s00024-018-1982-y.
Authors: Mohamed Sobh, Ahmed H. Mansi, Simon Campell, and Jörg Ebbing.
Contributions: Mohamed Sobh made the computations, created the figures and wrote the main part of the paper. Jörg Ebbing verified the method and supervised the findings. Simon Campell provided the terrestrial gravity data from Getech Company. Ahmed H. Mansi computed the terrain corrections using the GTE program. All authors discussed the results and contributed to the final manuscript.

Manuscript II (Sobh et al., 2019): Inverse and 3D forward gravity modelling for the estimation of the crustal thickness of Egypt. Tectonophysics, 752, 52-67.
https://doi.org/10.1016/j.tecto.2018.12.002

Authors: Mohamed Sobh, Jörg Ebbing, Ahmed H. Mansi, and Hans-Jürgen Götze.
Contributions: Mohamed Sobh made the computations, created the figures and wrote the main part of the paper with help from all other authors. All authors jointly contributed to discussions. Jörg Ebbing, Ahmed H. Mansi, and Hans-Jürgen Götze provided critical feedback and helped shape the research, modelling, and manuscript.

Manuscript III in preparation: Lithospheric structure of the Saharan Metacraton from 3D integrated petrological-geophysical modelling.
Authors: Mohamed Sobh, Jörg Ebbing, Ahmed H. Mansi, Hans-Jürgen Götze, and Mohamed G. Abdelsalam.
Contributions: Mohamed Sobh did all modelling and inversion, created the figures, participated in discussions and interpretations and wrote the manuscript with support from Jörg Ebbing. All authors jointly contributed to discussions.

Chapter 2

Manuscript I: Regional Gravity Field Model of Egypt Based on Satellite and Terrestrial Data

Abstract

This study presents a recent combined regional gravity field model over Egypt, developed by integrating satellite and terrestrial data via applying the remove-compute-restore (RCR) principle and the least-squares collocation (LSC) procedure. A high-resolution digital terrain model was exploited for the computation of the terrain and residual terrain corrections. Hereby, all the signals that can be modelled or deterministically computed are considered known and then removed in order to reduce the order of magnitude of the input gravity data prior to applying the LSC. Several GOCE-only and combined global geopotential models (GGMs) have been thoroughly investigated with respect to the EGM2008, in which the space-wise (SPW) solution, namely the SPW-R5 model, demonstrated the best performance. For the development of the combined model, the SPW-R5 GGM has been integrated with both the EGM2008 GGM and the terrestrial data retrieved from 56,250 gravity stations of the Getech data, acquired in the framework of the African Gravity Project. The combined regional gravity model was compared to the state-of-art XGM2016 global gravity model. The standard deviation of the differences is 18.0 mGal in terms of Bouguer anomalies. The combined regional model fits well with the terrestrial gravity data along the chosen North-South oriented profile through the Nile Delta region. The improvements of the developed combined regional model over the XGM2016 are due to the use of a more extensive terrestrial dataset. In conclusion, our model is more suitable than solely using ground data or GGMs for regional density modelling over Egypt. As an example, the comparison of using a global or regionally defined gravity model with the forward gravity modelling based on Saleh (Acta Geodaetica et Geophysica Hungarica 47(4):402–429, 2012) density model is performed.

2.1 Introduction

High-resolution regional gravity field models are of great importance for both geophysical and geodynamical applications, e.g. reliable density structure modelling of

the crust and lithosphere (Shih et al., 2015; Sampietro, Mansi, and Capponi, 2018b). Such a high-resolution gravity model can be typically estimated from terrestrial gravity measurements, which are not always available with a suitable coverage density. On the other hand, the global geopotential models (GGMs) derived from satellite observations can only contribute to the long wavelength signal.

There is a distinction between satellite-only models, e.g. the Laser Geodynamics Satellites (LAGEOS) (Yoder et al., 1983), CHAllenging Minisatellite Payload (CHAMP) (Reigber, Schwintzer, and Lühr, 1999), Gravity Recovery And Climate Experiment (GRACE) (Tapley et al., 2004), and, recently, the Gravity Field and Steady-State Ocean Circulation Explorer (GOCE) (Drinkwater et al., 2003; GOCE, 2010), and combined ones. Currently, several different combined GGMs such as the Gravity Observation Combination solutions (GOCO) (Pail et al., 2010), the European Improved Gravity models of the Earth by New techniques (EIGEN6C4) (Bruinsma et al., 2014), and the GOCE and EGM2008 combined model (GECO) (Gilardoni, Reguzzoni, and Sampietro, 2016) have been produced. These models comprise non-homogeneous terrestrial datasets, which is reflected as biases and distortions within the final gravity field model (Gatti, Reguzzoni, and Venuti, 2013). On the one hand, in the last decade, the International Association of Geodesy (IAG) has been interested in establishing a reliable geoid for the African continent as a whole (for instance, see (Abd-Elmotaal et al., 2018), where the Getech data, utilised in the current research, were not available), and accurate local/regional geoids for each state. For the geoid determination and geodetic applications, the interested reader is referred to (Abd-Elmotaal, 2008; Hanafy and El Tokhey, 1993; Alnaggar, 1986; Dawod, 2008), where the Egyptian geoid has been estimated exploiting the available terrestrial and the GGMs built utilising the CHAMP and GRACE missions.

In particular, the terrestrial gravity data over Egypt suffers large data gaps as well as being heterogeneously distributed, which lead to a low-resolution gravity field model, which, in turn, is not practical for a reliable density structure modelling. Consequently, for Egypt and similar regions, there is a persistent need to develop high-resolution regional combined gravity models based, mainly, on the recently-made-available terrestrial gravity data.

Hence, the best-fitting regional gravity models are derived by implementing the Remove-Compute-Restore (RCR) procedure and the Least-Squares Collocation (LSC) algorithm to integrate the available ground-based gravity data (Sec. 2.2.1) with GOCE-based GGMs (Sec. 2.2.2).

As a preliminary step, the GOCE-based GGMs were evaluated/assessed using independent ground-based gravity data in order to exclusively concentrate on those models that closely-describe the gravity field over Egypt and to understand within which spectral bands they deliver improved information. Accordingly, after the evaluation and modelling processes, the capabilities of the developed combined model were assessed by forward-compute the Bouguer anomaly field along a North-South oriented transversal profile that passes through the Nile Delta region based on the well-constrained density model proposed by (Saleh, 2012).

This paper is organized as follows: Sec. 2.2 gives a brief description of the various

utilised datasets. Then, the methodology to evaluate the performance of GOCE-based GGMs with respect to the XGM2016 (Pail et al., 2016) model and terrestrial gravity data is reviewed in Sec. 2.3. Sec. 2.4 reviews the computation of the regional gravimetric model, integrating the terrestrial data, the SPW-R5 solution, and the EGM2008 global model, via the RCR method and LSC algorithm. Sec. 2.5 discusses the model validation, whereas details on the forward density modelling process are given in Sec. 2.6. Finally, some relevant conclusions regarding the assessment of the regional gravity modelling using combined GOCE-based data and terrestrial gravity observations are drawn in Sec. 2.7.

2.2 Datasets

The datasets used in this study consist of (1) terrestrial free-air (FA) gravity anomalies, (2) gravity field in terms of gravity anomalies derived from the GOCE-based GGMs and the XGM2016 (Pail et al., 2016) model, and (3) high-resolution ($3'' \times 3''$ arc-second) topographic heights provided in terms of a digital terrain model (DTM) over the study area.

2.2.1 Terrestrial Gravity Data

A regular $5' \times 5'$ arc-minute grid of FA gravity anomalies, extended over Egypt, was provided by the Getech. This grid was developed using a simple interpolation algorithm over the 56250 observation stations, acquired in the framework of the African Gravity Project (Fairhead et al., 1988). Fig. 2.1 shows the distribution of those gravimetric stations projected onto a topographic map. As some of these data were collected long before the GNSS/GPS era, the major sources of errors that contaminate the data are the inaccurate estimates of the positions and heights of the stations. For most surveys, details on the accuracy and/or errors are neither separately provided nor reported within the acquisition logs metadata. The data provider has suggested an accuracy of 1.0 mGal. However, it is expected that the accuracy of the provided FA gravity anomalies, based on the noticeable high-inhomogeneity should be substantially lower in the majority of the study area.

Since the processing of the Getech gravity data is not clearly understood, by the common user, and that the data provider recommends the 1.0 mGal accuracy, it is difficult to assess the actual accuracy of the data used for creating the FA grid. However, considering that the BGI (Bureau Gravimétrique International) gravity data over the Egyptian territory have been included for the generation of the previous $5' \times 5'$ arc-minute grid of gravity anomalies, we have attempted to assess the prediction accuracy by comparing each validated BGI gravity observation with its corresponding Getech grid-based predicted value using the Spline interpolation. Fig. 2.2-a shows the spatial distribution of the 320 BGI gravity stations used for such a validation. The residuals range between -20.83 and 20.26 mGal with a mean value of about -0.43 mGal and a standard deviation (STD) of 7.01 mGal. Fig. 2.2-b shows the histogram of the Getech grid data evaluation, where the residuals show a Gaussian normal distribution. The analysis of the results proves that such a gridded gravity dataset is suitable for geophysical applications such as the purpose of this research, i.e. regional density modelling.

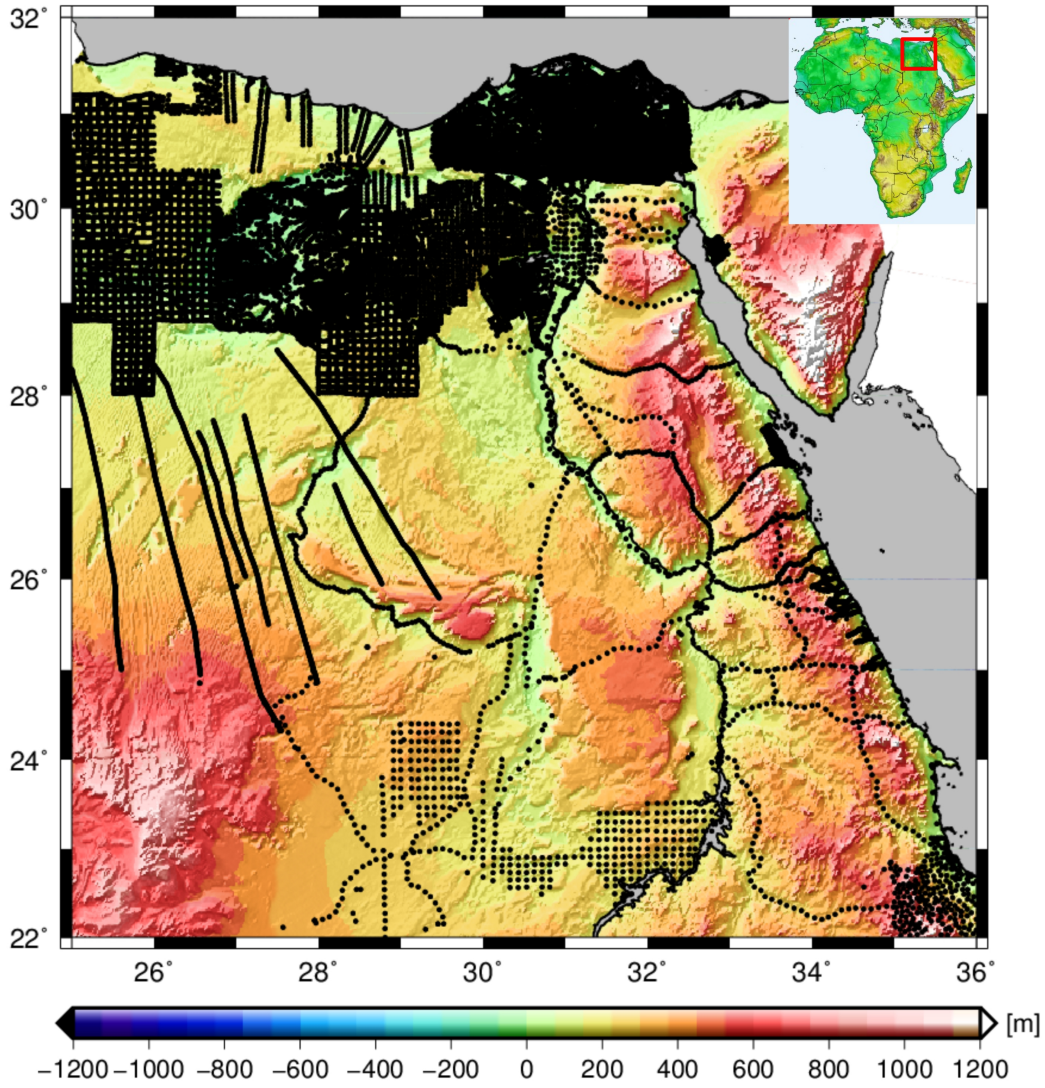

Figure 2.1: The spatial distribution of the available terrestrial gravity stations over Egypt projected onto a topographic map; unit [m].

2.2.2 GOCE-Based GGMs and XGM2016

The various existing GOCE-based GGMs are globally optimized, therefore they, generally, exhibit similar characteristics when the gravitational signal is analysed on a global scale. Still, these models can differ, especially, when the gravity field is studied on a local or regional scale. Hence, three recent GOCE-based GGMs, based on the space-wise (SPW) (Gatti et al., 2016), direct-wise (DIR) (Bruinsma et al., 2013), and time-wise (TIM) (Pail et al., 2010) approaches, have been utilized in order to cross-validate the terrestrial FA gravity anomalies. While the development of the SPW-R5 solution exploited the full GOCE gradiometry mission, both the DIR-R5 and TIM-R5 solutions only used about 42 months of GOCE measurements. In details, the latter, namely the TIM-R5, has been considered the core data in developing the GOCO5S combined model (Mayer-Güerr, 2015). These models are available in terms of spherical harmonic (SH) coefficients. For more details about the model differences, see

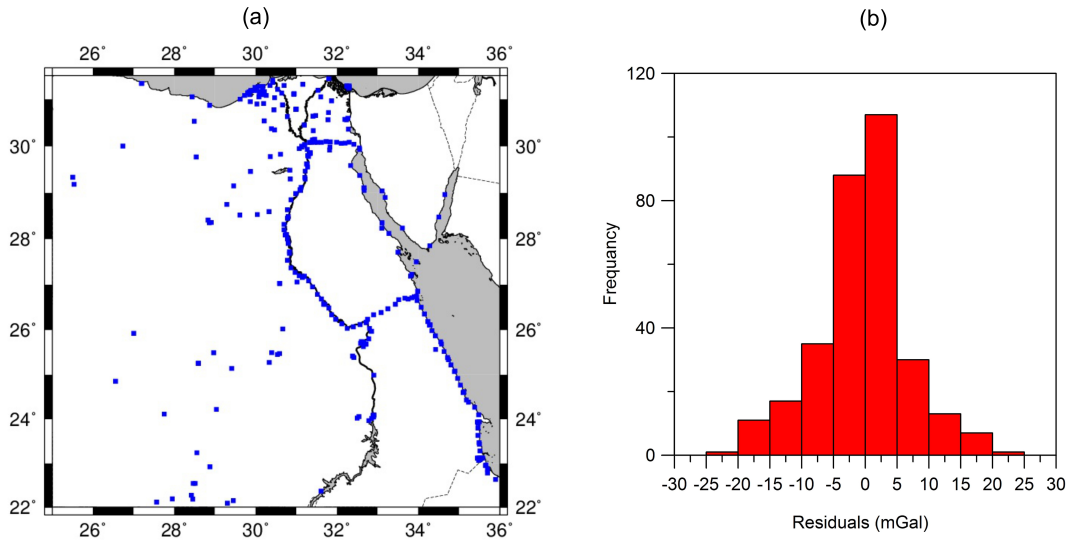

Figure 2.2: A- The spatial distribution of the 320 BGI gravity stations; Unit [degree] and B- the histogram of the discrepancies between the BGI dataset and the Getech-based predicted values; unit [mGal].

(Pail et al., 2011).

The XGM2016 model (Pail et al., 2016) has been used as the state-of-the-art high-resolution GGM in order to assess the considered GOCE-only and combined GGMs. The XGM2016 is a preparation release of the planned Earth Gravitational Model 2020 (EGM42020) that will succeed EGM2008 (Pavlis et al., 2008). For instance, the XGM2016 combines recent terrestrial gravity data with the latest satellite gravity observations from GRACE, GOCE, and altimetry up to a maximum SH degree/order (d/o) of 719.

2.2.3 Digital Terrain Model

The availability of a high-resolution DTM is essential when locally/regionally comparing GOCE-based GGMs with the terrestrial gravity data since it would be used to fill in the remaining gravity signals beyond those provided by the maximum d/o of GOCE-based models by computing the so-called Residual Terrain Model (RTM) (Forsberg, 1984). The topographic heights collected by the Shuttle Radar Topography Mission (SRTM) with a resolution of 3 arc-second ($\approx$ 90 m), shown in Fig. 2.1, have been used. Such data are freely distributed via the public web service (https://lta.cr.usgs.gov/SRTM) (Farr et al., 2007). Due to the low resolution of the terrestrial gravity data, equivalent to 5 arc-minute, the 3 arc-second spatial resolution DTM was preferred over the other available high-resolution products, e.g. the 1 arc-second, in order to avoid the propagation of any uncorrected artefacts (Walker, Kellndorfer, and Pierce, 2007; Arrell et al., 2008).

2.3 Processing Strategy

2.3.1 Overview

The processing scheme that consists of three main steps, in which the output of one step will serve as the input to the succeeding one, is explained as follows:

1. Comparison: cross-compare the performance of the investigated GOCE-based GGMs, the XGM2016, and the terrestrial FA gravity signals, where the latter takes the terrain reduction, i.e. the RTM method, into consideration;

2. Regional modelling: the gravity field, sewing together the ground observations, GOCE-based SPW solution, and the EGM2008 model, is estimated on the basis of the RCR method and LSC technique;

3. Validation: the performance of the combined regional gravity model is validated using the high-resolution XGM2016 GGM and the well-constrained density model built for a transversal profile oriented North-South along the Nile Delta region.

In order to decide which of the investigated GOCE-based GGMs would better model the gravity field over Egypt, the synthesized signals, at least in theory, must be validated using gravity-independent data. In practice, both the XGM2016 and a few independent gravity stations that took the spectral consistency into consideration, i.e. the short and very short wavelengths signals beyond the maximum d/o of the GOCE-based GGMs, were used.

GOCE-based GGMs and the XGM2016 models are cross-compared at the same spectral bands, where their SH syntheses have been constructed from d/o= 2 up to $N_{max} = 250$ (with a step of d/o= 10). More attention was given to the d/o ranging from 100 to 250, corresponding to a regional spatial resolution that approximately varies between 200 and 80 km (20000 km/degree), respectively, to examine which GGM closely-approximated and better-described the gravity field over Egypt, especially at the medium-to-short wavelength spectral bands where they are expected to deliver their improved information (Bruinsma et al., 2013; Sampietro, Mansi, and Capponi, 2018a).

The performance of the various investigated GOCE-based GGMs and the EGM2008, with respect to a reference model, for instance, the XGM2016, in terms of degree difference amplitude ($\Delta\sigma_n$) are presented in Fig. 2.2. Such differences have often been computed in order to quantify the powers of the signal and its corresponding gravity field estimation error at various spatial wavelengths using Eq. 2.1.

$$\Delta\sigma_n = \frac{GM}{R_E^2} \cdot \sqrt{\sum_{m=0}^{n} (\Delta c_{nm}^2 + \Delta s_{nm}^2)} \tag{2.1}$$

where G is the Newtonian gravitational constant, M is the bulk-mass of the Earth, Δc_{nm} and Δs_{nm} are the differences of the SH sine and cosine coefficients between the GOCE-based GGMs and the corresponding ones of the XGM2016, n and m are the SH degree and order, respectively, and R_E is the mean radius of the Earth at the reference ellipsoid $\equiv$ 6378.137 km.

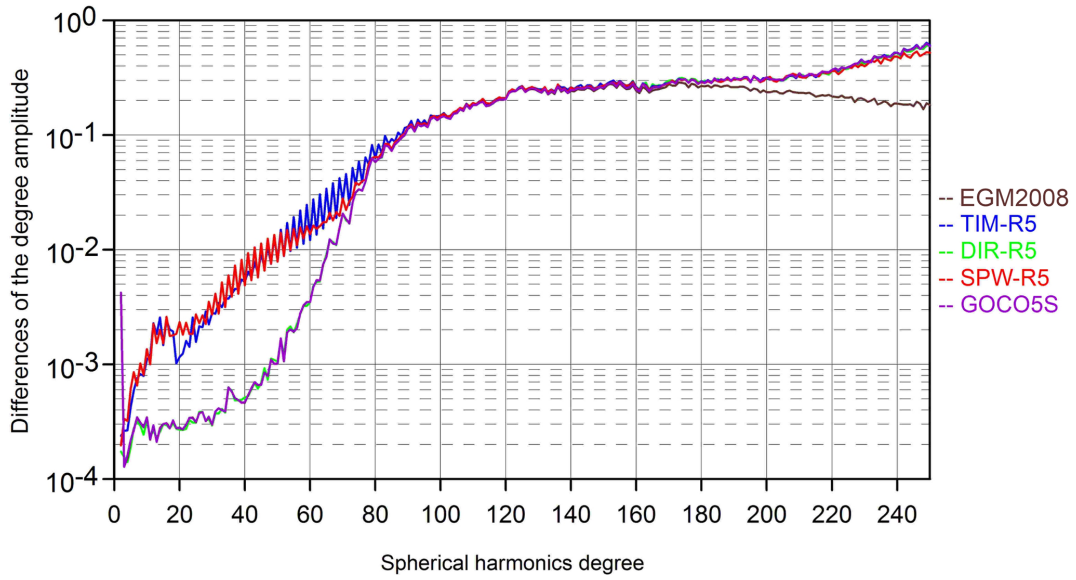

Figure 2.3: Degree difference amplitude of the gravity field anomalies of the various investigated GOCE-based GGMs as well as the EGM2008 model (from d/o= 2 to N_{max} = 250) with respect to the corresponding signal from the XGM2016 model truncated at the same SH d/o; unit [mGal].

From d/o 200 onward, the monotonic STD has rapidly increased for all the GOCE-based GGMs solutions, since the coefficients beyond d/o 180-200 were estimated with the use of Kuala's rule (Kaula, 1966) and the signal-to-noise ratio (SNR) noticeably diminished over d/o equivalent to 200 (Rummel, 2015). The SPW-R5 GGM, the fifth release of the SPW solution, provides a small degree difference amplitude at lower SH degrees and, on the meantime, outperforms the other two official European Space Agency (ESA) products, namely the DIR-R5 and TIM-R5 solutions, as well as the GOCO5S GGM. The EGM2008 model has the least degree difference amplitudes especially at higher SH degrees as a direct consequence of the usage of the altimetry/terrestrial data into its development. Therefore, all above mentioned GOCE-based GGMs will be analysed but only the plots related to processing the SPW-R5 model, expected to deliver the best results, will be plotted.

2.3.2 Validations and Pre-processing of the Terrestrial Data

As a start, a quality assurance step is necessary as the terrestrial data were acquired over a long time span with different measurement techniques without any quality control/assurance metadata. Therefore, the data were first cross-validated (i.e., filtered) and the existing outliers were tagged and removed. All the heights of the 56250 gravity stations were compared with the commensurate ones from the SRTM-based DTM. The height discrepancies range between -685 m and 369 m with a mean and STD of 5.9 and 72.9 m, respectively. All gravity stations with height differences beyond ± 100 m, which corresponds to about 30 mGal in terms of FA anomaly values, were flagged and then filtered. Applying such an empirical outlier detection, a total number of 6000 stations were identified and then removed as reported in Fig. 2.4.

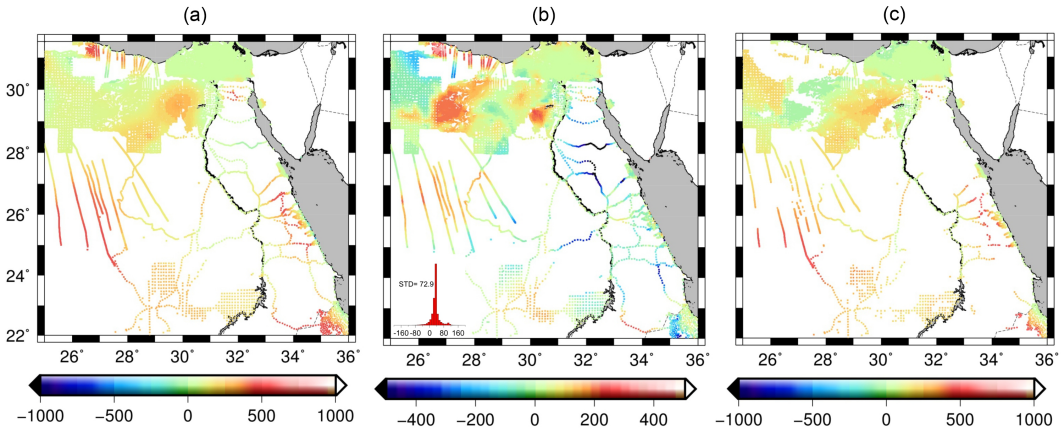

Figure 2.4: Comparison of gravity station heights provided by the Getech dataset, (a) the absolute heights, (b) the differences to the SRTM-based DTM, where the histogram of these height differences, whose standard deviation equals 72.9 m, is reported on the lower left corner, (c) the remaining heights after the removal of outliers; unit [m].

In order to evaluate the topographic effects by means of RTM, two DTMs were used, namely the detailed and reference ones. The former is the actual high-resolution DTM (a spatial resolution of 3 arc-second), while the latter is a smoothed DTM (of 5 arc-minute resolution that is consistent with the spatial resolution of the terrestrial gravimetric data) obtained via applying a moving average window over the detailed one. The two terrain correction signals, exploited to evaluate the RTM, are computed by means of the Gravity Terrain Effects (GTE) software package (Sampietro et al., 2016; Capponi, Mansi, and Sampietro, 2018).

The GTE software is an integration of the deterministic prism modelling and fast Fourier transformation (FFT) techniques in order to maximize the accuracy of the computed gravitational effects, at any given altitude as well as the surface of the topography, minimizing the computational time (Sampietro et al., 2016). The topography potential induced by the residual topographical masses between those two DTMs is taken into account within the reduction process (Sampietro et al., 2017; Zaki et al., 2018a). The topography effects on gravity in terms of RTM reduction dg_{RTM} is approximated in (Forsberg, 1984).

First, the syntheses of the investigated GOCE-based GGMs, truncated at various d/o, are compared to the XGM2016 signal, in terms of FA gravity anomalies, where within Tab. 2.1, the statistics of only d/o 200 and 240 are reported for the sake of simplicity. The STD of the differences for d/o 200 and 240 are at the level of 0.72 and 2.76 mGal, respectively. Therefore, d/o 200, in which all GGMs delivered the minimum STD values, will be used as the integration SH threshold. Also, the SPW-R5 will be exploited in the development of the combined model as it illustrated the minimum statistics, in terms of minimum, maximum, and mean error values as well as the lowest STD value.

After checking the height information and before the application of the LSC procedure, the acquired gravity values had to be validated. This validation was accomplished by thoroughly comparing the terrestrial observations to the syntheses of the

Table 2.1: The statistics of the differences between the free-air gravity anomalies obtained from GOCE-based GGMs truncated to d/o 200 and 240 and the corresponding signal calculated from the XGM2016 model; units [mGal].

Model	$\delta\Delta g_{FA}$ ($N_{max} = 200$)				$\delta\Delta g_{FA}$ ($N_{max} = 240$)			
	Min	Max	Mean	STD	Min	Max	Mean	STD
SPW-R5	-2.86	4.07	0.02	0.72	-10.02	9.59	0.55	2.76
DIR-R5	-3.29	4.49	0.13	0.79	-8.43	8.20	0.25	3.33
TIM-R5	-3.42	4.28	0.07	0.66	-9.13	8.98	0.35	3.41
GOCO5S	-4.64	5.34	0.20	1.40	-16.99	15.81	1.49	6.16

SPW-R5 and XGM2016 GGMs in a restricted spectral bandwidth, up to d/o 200 and 719, respectively, without using the RTM signal. Consequently, the results of the mutual-comparison of the data to the SPW-R5 and XGM2016 are shown in Fig. 2.5. As expected, the differences resulting from the utilization of the SPW-R5 are high in several regions, because GOCE resolution does not cover the short wavelengths signals. The small differences obtained from the XGM2016 are justified as it contains the medium-to-short wavelengths. Tab. 2.2 documents the main statistical properties of such a validation.

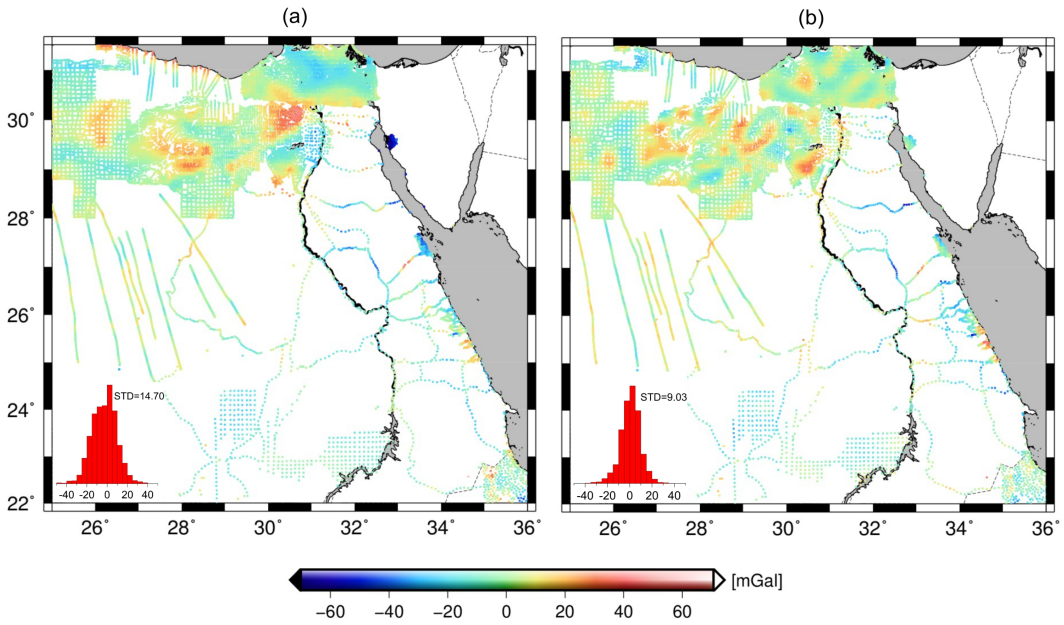

Figure 2.5: The differences of the terrestrial gravity data with respect to (a) the SPW-R5 synthesized to d/o 200 and (b) the XGM2016 synthesized to d/o 719. The histogram of the residuals whose standard deviation are 14.70 and 9.03, respectively, are reported on the lower left corner; unit [mGal].

Table 2.2: Statistical parameters of the differences between the terrestrial gravity data and the global gravity field synthesised by the SPW-R5 and XGM2016 models up to $N_{max} = 240$; units [mGal].

Anomaly	Min	Max	Mean	STD
SPW-R5 [d/o 200]	-78.31	57.90	-3.90	14.70
XGM2016 [d/o 719]	-60.17	43.02	0.72	9.03

2.4 Combined Gravity Field Modelling over Egypt

In order to compute the combined regional gravity model integrating together the available terrestrial data over Egypt with the SPW-R5 GGM, the classical RCR principle has been applied. For more details on the application of the RCR technique in geodesy, the interested reader is referred to (Moritz, 1980). In physical geodesy, the RCR is considered one of the most widely applied Methods to remove the long and very-short wavelengths contributions from the ground-based FA gravity anomalies, then after performing the LSC process, all the removed signals are restored back. Fig. 2.6 depicts the flowchart of the RCR principle followed for the evaluation of the combined regional gravity model. In the following subsections, the remove, compute, and restore steps are explicitly explained.

2.4.1 Remove Step

The effects of both the long and very-short wavelengths components of the gravity field should be removed from the terrestrial FA gravity anomalies in order to compute the residual field. Also, the data should be downward continued from their actual altitude to the geoid, in theory, or the surface of the Earth, in practice, by performing a downward continuation, but such a reduction step is out of the scope of this work, and the interested reader is directed to (Mansi, Capponi, and Sampietro, 2018; Sansò and Sideris, 2016). The syntheses of all the investigated GOCE-based GGMs truncated at d/o 200 are used to calculate the long wavelengths components. Furthermore, the very-short wavelengths contributions of the gravity signal were computed and removed exploiting the RTM method as shown in Fig. 2.7. The statistics of the observed and residual gravity anomalies are reported in Tab. 2.3.

Table 2.3: Statistics of the observed gravity anomalies reduced for the gravity anomalies, Δg_{black} of the SPW-R5 model; units [mGal].

Anomaly	Min	Max	Mean	STD
Δg_{obs}	-62.399	72.80	-2.76	19.33
$\Delta g_{red} = \Delta g_{obs} - \Delta g_{GGM}$	-59.190	43.29	0.75	9.03
$\Delta g_{red} = \Delta g_{obs} - \Delta g_{GGM} - \Delta g_{RTM}$	-97.960	65.45	-8.35	14.27

The results clearly show that removing the long wavelengths components yields a substantial diminution of the data of about 53%, in terms of STD that dropped from 19.33 to 9.03 mGal. However, a further reduction step that accounts for the

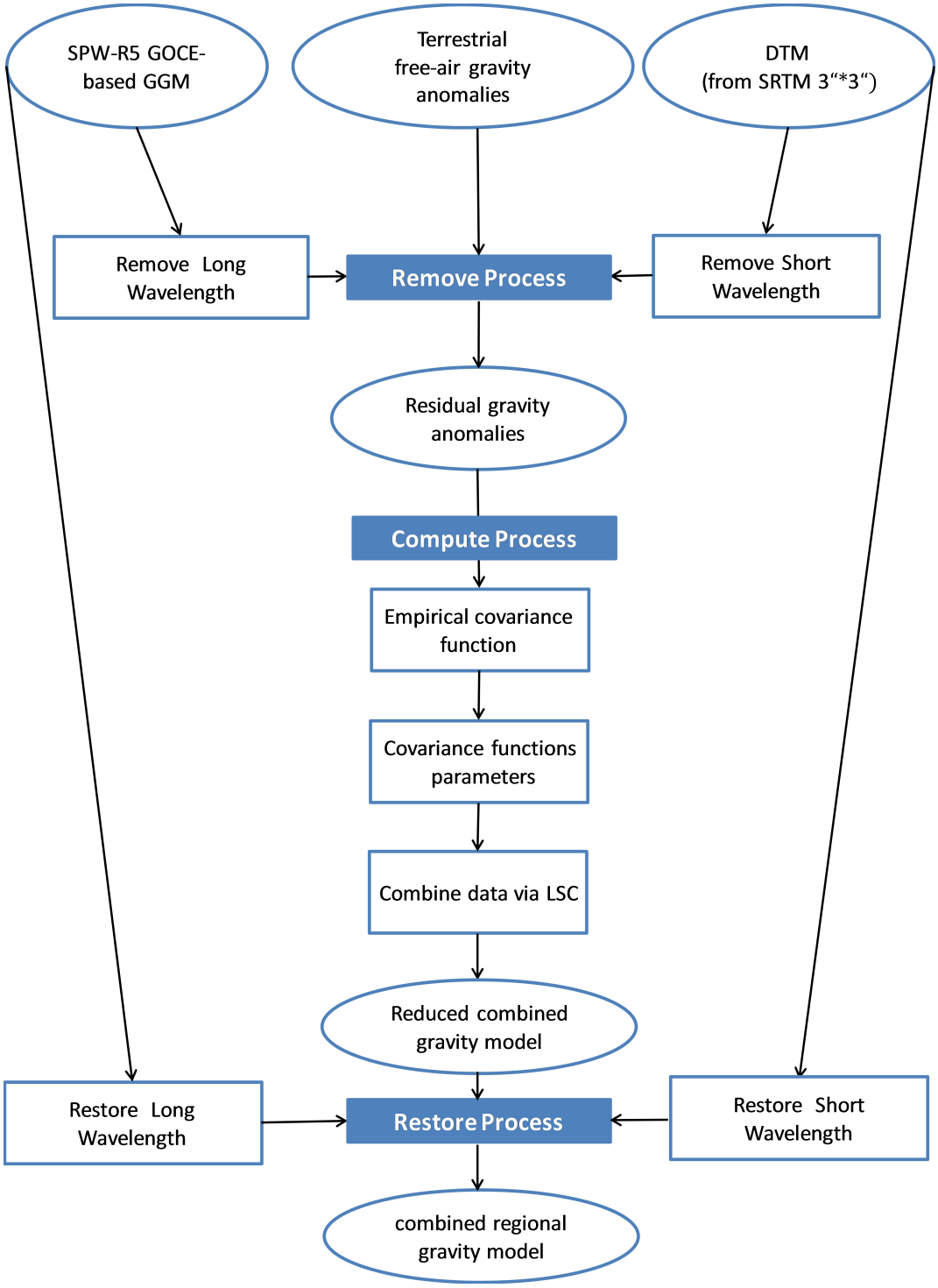

Figure 2.6: Flowchart describing the computation of the regional gravity model based on the RCR approach.

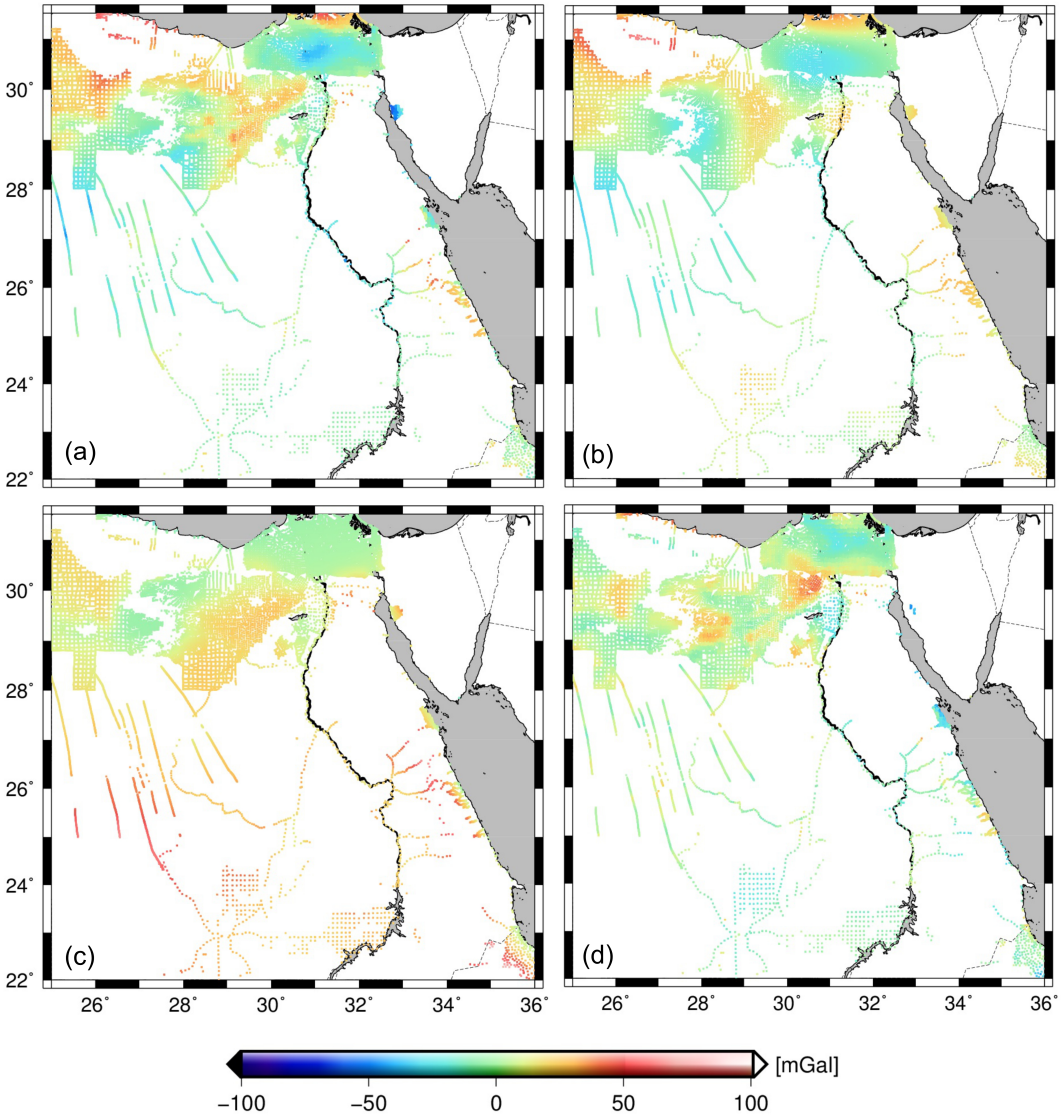

Figure 2.7: Data preparation (remove step) for the LSC. (a) The terrestrial FA anomalies; (b) the SPW-R5 (long wavelength component of the SPW GOCE solution); (c) the RTM and (d) the final reduced signals; unit [mGal].

RTM signal, i.e. the removal of the very-short wavelengths contributions, increased the variation of the data of about 58%, where the STD increased to 14.27 mGal, hence additional improvements were not gained. Such abnormal results could be due to limitations in the quality of the terrestrial gravity data provided by the Getech for Egypt. Consequently, in our study case, the RTM reduction is not a beneficial step and will not be accounted for within the development of the combined model. A similar behaviour was observed during the geoid computation of Sudan using Getech data (Godah and Krynski, 2015). Fig. 2.7 reports the reduced gravity signals, the SPW-R5 GGM as well as the RTM contributions.

2.4.2 Compute Step (LSC and Covariance Information)

The LSC method, introduced to geodesy by (Moritz, 1972; Moritz, 1978), is the most used stochastic modelling technique to perform an optimal linear estimation for gravity field parameters integrating different heterogeneous gravity data both in spatial and frequency domains (Barzaghi et al., 1993; Gilardoni, Reguzzoni, and Sampietro, 2012). (Krarup, 1969) gave a formula for the best linear unbiased estimate of the signal (predictable stochastic part of a target quantity) in a Hilbert space with a reproducing kernel as follows:

$$S = C_{sl}(C_{ll} + C_{vv})^{-1} \cdot l \tag{2.2}$$

where S is the target quantity to be estimated from the vector of observations l, C_{sl} is the cross-covariance matrix that represents the signal covariance between the input signals l and the target quantity S. C_{ll} is the auto-covariance matrix of the observation vector, and C_{vv} is the variance-covariance matrix of the noise, which represents the standard error of the observed gravity anomalies (in practice a diagonal matrix). The covariance matrices C_{ll} and C_{vv} describe the statistical correlations of the signal and noise components, respectively.

One of the key advantages of LSC is that it provides information about the errors alongside with the estimated regional gravity field and geoid models in forms of variances or even full variance-covariance matrix $C_{\epsilon\epsilon}$ (Moritz, 1989):

$$C_{\epsilon\epsilon} = C_{ss} - C_{sl}(C_{ll} + C_{vv})^{-1} \cdot C_{ls} \tag{2.3}$$

with C_{ss} represents the autocovaiance matrix of the signal. The LSC toolbox used in this research is based on an algorithm developed by (Tscherning, 1992).
Regarding the modelling step, the quality of the inversion of gravity data highly depends on the covariance function of the observations, i.e. the residual gravity signal, (Knudsen, 1987) as well as the covariance that accounts for the noise, if it exists (Tscherning, 1985). Thereupon, such a task could be easily fulfilled by computing the empirical covariance function (see Fig. 2.8) using the residual gravity signal by the Empirical Covariance toolbox described in (Sampietro et al., 2017).

Then, one of the well-known covariance functions that best-fits the empirical covariance function computed from the data has to be chosen as the theoretical covariance function. In our case, the empirical covariance function estimated for the whole area of Egypt using the reduced gravity signal, Δg_{red}, is fitted with a set of n Bessel functions of the first order and zero degree (Kreh, 2012; Braitenberg et al., 2016). Bessel functions exploit all the stochastic properties of the residual gravity signal to its utmost, which, in turn, reduces the mis-fitting/modelling between the empirical and theoretical covariance functions that can be mistakenly considered as coloured noise (Braitenberg et al., 2016).

As a consequence, the theoretical covariance function is built as a linear combination (with positive coefficients) of these n Bessel functions in the frequency domain, as shown in Fig. 2.8, exploiting the well-known relation between the 2D-power spectral densities and Bessel functions (Watson, 1995), which guarantees to obtain a positive definite covariance matrix (Mansi, 2016). Details on the theoretical aspects

related to this procedure are reported in (Sampietro et al., 2017). Once the theoretical covariance function is estimated, it can be used to build the covariance matrix for the LSC procedure. In this step, the combination of the terrestrial data and the SPW-R5 GGM signal, synthesized at the same coordinates of terrestrial stations, can be straightforwardly performed if an estimate of the error of the SPW-R5 model is available.

The empirical and theoretical covariance functions, represented in Fig. 2.8, exhibit a good agreement up to 0.65° of spherical distance, before it reaches zero. These estimated parameters were then utilized to calculate the residual gravity anomalies on a regular grid of $5' \times 5'$ spatial resolution. Having prepared all its constituents, the LSC was performed according to Eq. 2.2 to generate the targeted combined regional gravity field over Egypt.

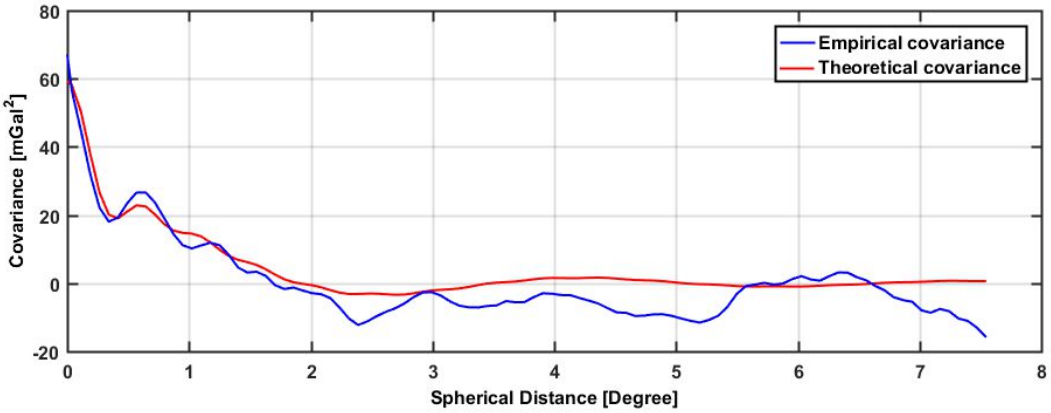

Figure 2.8: Empirical and analytical fitted covariance functions using different GGMs models; unit [mGal^2].

2.4.3 Restore Step

At this point, the long and short wavelengths components of the gravity field can be restored and summed up to the residual gravity anomalies in order to obtain the full gravitational signal for the SPW-R5, DIR-R5, TIM-R5, and GOCO5S GGMs, as shown in Fig. 2.9. The former can be restored using the FA gravity field derived from the syntheses of the different GGMs truncated at d/o 200, whereas the latter is recoverable from the EGM2008 model synthesized from d/o 201 to its maximum d/o, i.e. 719, in order to be compatible with the XGM2016. A note must be taken that the one does not need to restore the RTM signal as it has not been considered within the remove step because the reduced signal did not gain any improvements after taking it into consideration. The statistics of the differences between the various developed combined models and the XGM2016 model are reported in Tab. 2.4, where the SPW-R5-based regional combined model delivered the minimum STD value of 8.75 mGal, as expected. Therefore, the best combined regional gravity model for Egypt is computed on basis of the SPW-R5 model, displayed in Fig. 2.10, by summing up all the effects with the residual signal.

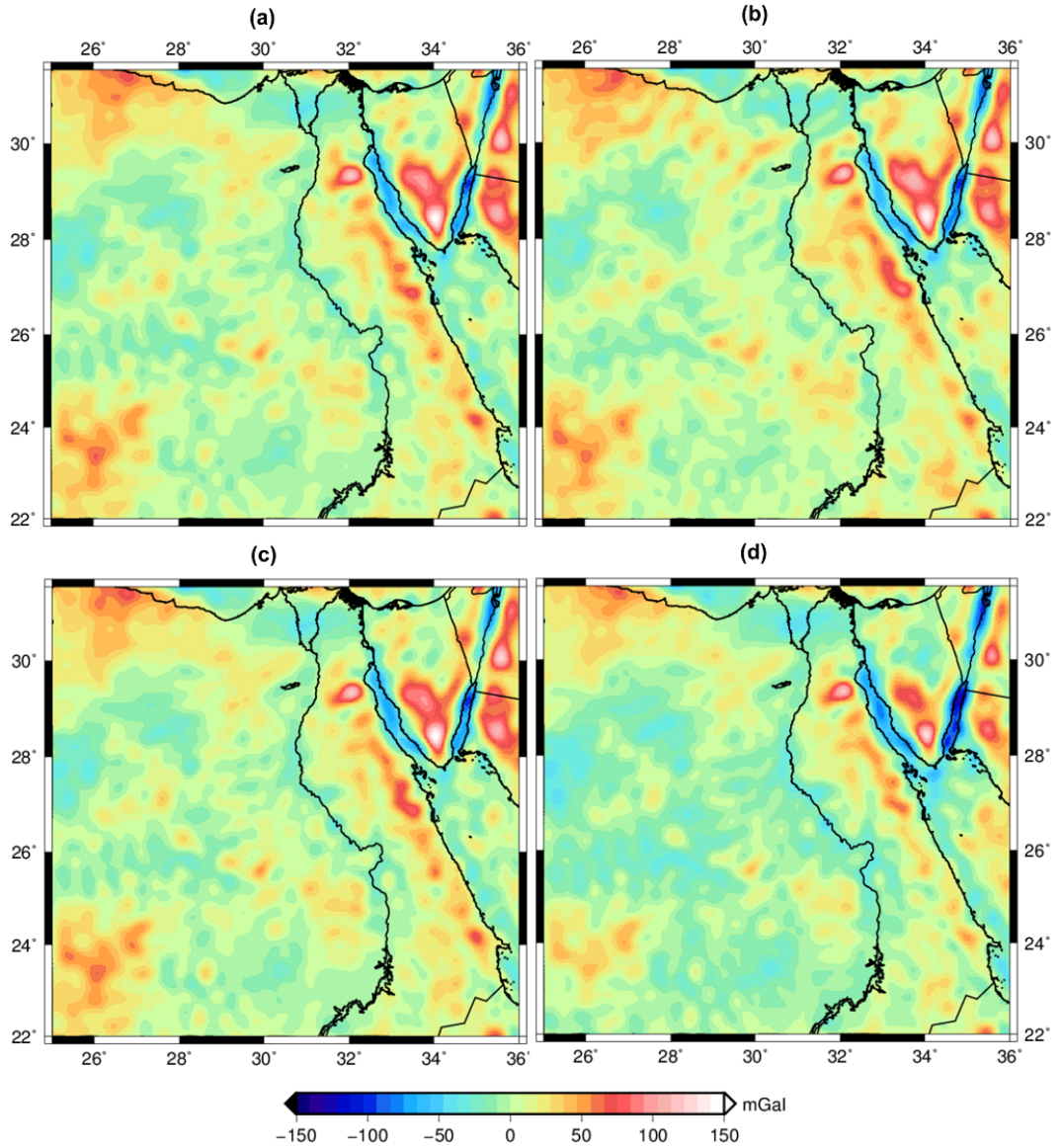

Figure 2.9: The restored signals using different GGMs models: (a) the SPW-R5; (b) the DIR-R5; (c) the TIM-R5; and (d) the GOCO5S GGM; unit [mGal].

Table 2.4: The statistics of the comparison between the XGM2016 model and the different combined models computed on basis of the SPW-R5, DIR-R5, TIM-R5, and GOCO5S GGMs; units [mGal].

Model	Min	Max	Mean	STD
XGM2016 - SPW-R5	-126.72	102.07	0.69	8.75
XGM2016 - DIR-R5	-118.97	104.38	1.29	9.59
XGM2016 - TIM-R5	-126.49	101.09	0.77	8.82
XGM2016 - GOCO5S	-100.25	121.78	2.04	10.46

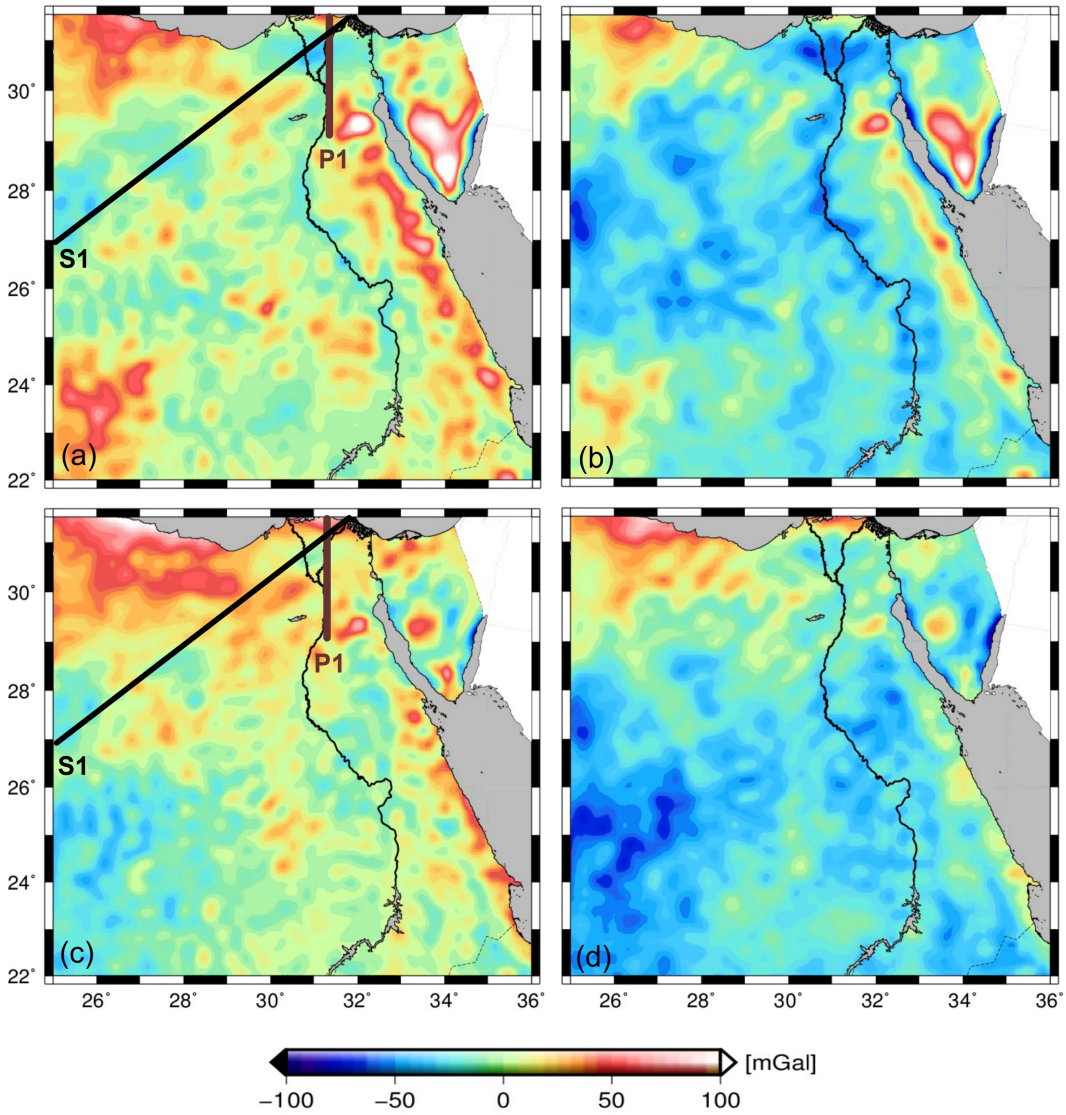

Figure 2.10: Comparison of the combined regional gravity model with the XGM2016 global model. (a) The free-air gravity anomalies according to our combined model, (b) the Bouguer anomalies (i.e. free-air anomalies reduced by the topographic effect) computed by the combined model, (c) the free-air gravity anomalies synthesised from the XGM2016 global model, and (d) the Bouguer anomalies retrieved by the XGM2016 global model. The black line shows the location of the profile described in Fig. 2.12. The brown line P1 shows the location of the profile described in Sec. 2.5 and the black line S1 displays the location of the NorthEast-SouthWest cross-section S1; unit [mGal].

2.5 Combined Model Validation

Firstly, the Bouguer anomalies were computed by removing the gravitational effects of the topographic masses from the developed combined regional gravity model, computed by means of the GTE, as shown in Fig. 2.10, in order to validate the goodness of such a combined model. The estimated combined model in terms of FA and Bouguer anomalies (Fig. 2.10-a and c) is compared to the XGM2016 model (Fig. 2.10-b and d). Moreover, the differences evaluated by the combined regional gravity models with respect to the XGM2016 (see, Fig. 2.5) illustrated the lowest STD of

8.75 mGal for the SPW-R5-based combined model, see Tab. 2.4. A reminder must be made here, that the computational steps have been systematically repeated in order to compensate for the long wavelengths contributions using the DIR-R5, TIM-R5, and GOCO5S models, whose restored signals with respect to the XGM2016 are characterized by STD values of 9.59, 8.82, and 10.46 mGal, respectively.

Hence, such differences could be seen as a direct reflection of the improvements gained from the produced combined regional gravity model, which has accounted for terrestrial data contribution, over XGM2016 model, where such data were not used.

Furthermore, for an additional validation step, the radial average power spectrum of the combined gravity model, the XGM2016, and the SPW-R5 GGMs was calculated. As illustrated in Fig. 2.9, the power of the combined model is evidently higher in the short wavelengths band as a direct contribution of the terrestrial data. That is due to the fact that the combined model has more details since it contains short wavelengths attributes gained from the ground gravity data. The power of the XGM2016 model lies in between both models, the combined model and the SPW-R5, which is reasonable as it has a maximum d/o of 719.

A NorthEast-SouthWest cross-section, namely S1, was considered for a thorough

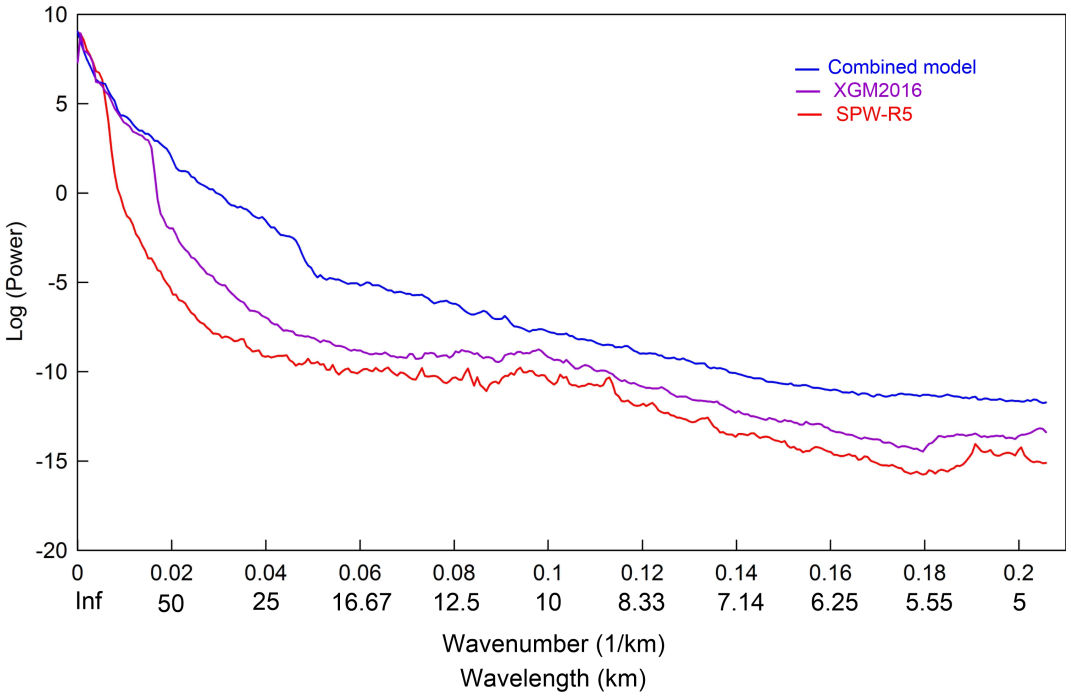

Figure 2.11: The Spectral representation of the combined model (blue), the XGM2016 model (purple), and the SPW-R5 GGM (red).

wavelengths comparison between the combined, the SPW-R5, and the XGM2016 models, see Fig. 2.10. It can be easily noticed, from Fig. 2.12, that the SPW-R5 signal is the smoothest since it only contributes the long wavelengths. On the other hand, as mentioned earlier, the combined model retrieved more detailed short wavelengths as a direct contribution of terrestrial data. In contrast, the XGM2016 model, along the cross-section S1, looks smoother in comparison to the combined model since it

solely has SHs until 719.

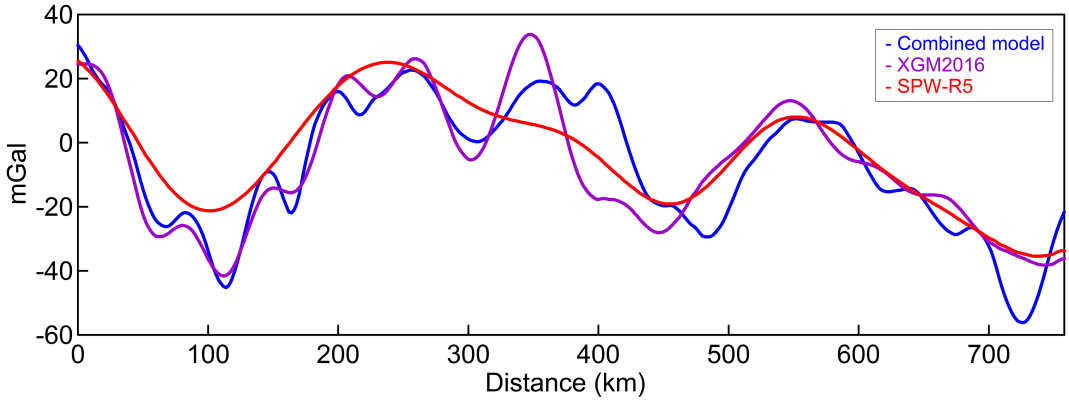

Figure 2.12: The differences between the combined model, the XGM2016, and the SPW-R5 GGM along NE-SW profile; unit [mGal].

2.6 Forward Density Modelling

As a geophysical application, the combined regional gravity model was utilised to build a forward density model for the Delta region, located within the Northern Egypt, where dense data are available. The 2D forward gravity modelling was accomplished using the IGMAS+ software (Götze and Lahmeyer, 1988; Schmidt et al., 2010).

The representative profile, named P1 (see Fig. 2.10), has been taken perpendicular to the general geological strike of the region oriented in the North-South direction. For the purpose of this research, the model set-up initially contained several layers that were constrained by the interpretation of various deep seismic profiles (Makris et al., 1982; Marzouk, 1988) with a fine-tuning applied on the geometry. The density values of the sedimentary layers were estimated based on the available drill wells studies executed over the Nile Delta area and those of the crust and upper mantle were derived from the P-wave seismic velocity by converting the velocities to density values using the approach of (Christensen and Mooney, 1995).

The model represents thick sedimentary basins from the North near the off-shore area (more than 8 km) that thin towards the South. The Northern part of the model shows a thin crust ($\simeq$ 24 km) beneath the coastal line of the Mediterranean Sea, with the crustal thickness increasing toward the South, reaching about 32 km (see Fig. 2.13).

The original density model proposed by (Saleh, 2012) was constructed without using any satellite gravity data. The calculated Bouguer anomaly represented as a black solid line in Fig. 2.13 served as a reference model in order to compare these estimated by the combined gravity model and the XGM2016 GGM.
The original model geometry and densities (Saleh, 2012) were kept fixed and subse-

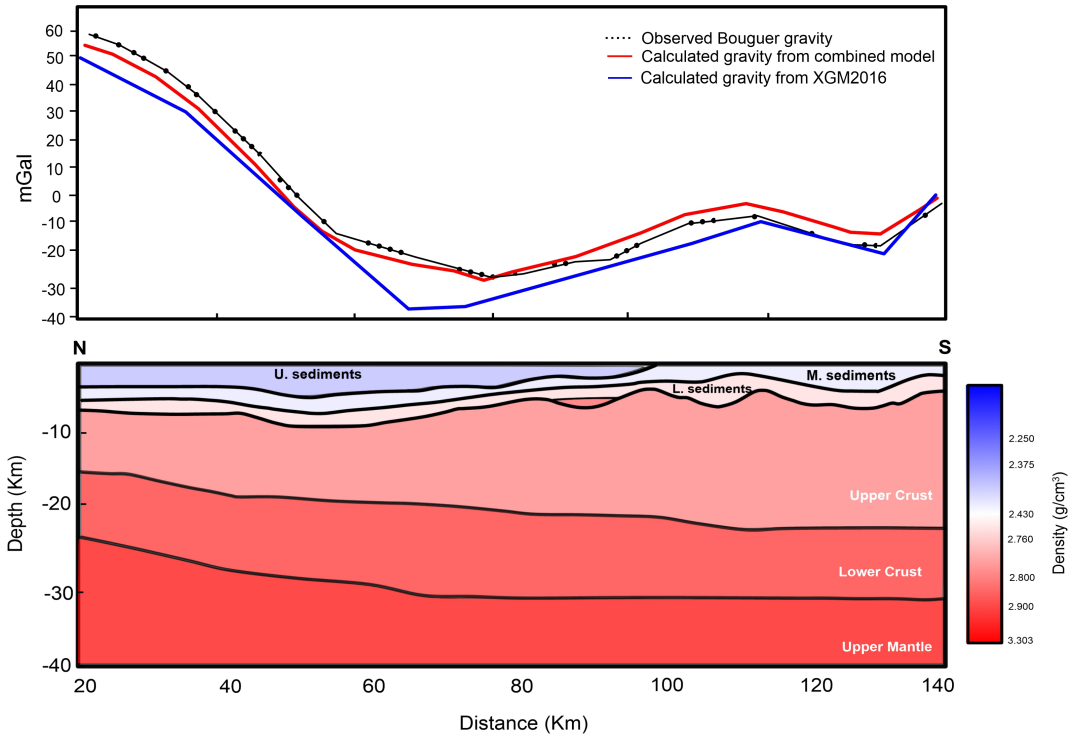

Figure 2.13: A vertical cross-section of a 3D density model from the P1 (N-S) profile over the Nile Delta region (P1). The thin solid black line is the measured gravity anomaly, the red solid line is the modelled gravity signal using the combined gravity model, and the blue solid line is the calculated gravity using the XGM2016 model. The Geometry and the density values of the model were retrieved from (Saleh, 2012).

quently, the Bouguer anomaly of the combined regional gravity model was forward-calculated. The modelled signals almost perfectly match the observed gravity values with a STD of 7.0 mGal for the residuals evaluated for the observed and modelled signals. In contrast, the XGM2016 anomalies fit the general trend of the observed data but with a higher STD equivalent to 18.0 mGal.

The produced mass deficit associated with the XGM2016 can be compensated by an increase in the crustal and sediment density values or a decrease in the crustal and sediment thickness. However, such scenarios lead to an unrealistic crustal structure, which deviates from the density model of (Saleh, 2012) that is seismically constrained. We aim to test the combined model with the existing model without any changes. The displayed anomalies from the combined model along the cross-section present a good agreement with the well-constrained density model (Saleh, 2012).
For our combined regional gravity model, the contribution of the terrestrial gravity measurements improved the gravity signals in comparison with the XGM2016 model over the study region, since it has been generally developed using only a limited number of terrestrial gravity points, over Egypt.

2.7 Conclusion

A new combined regional gravity model has been developed for Egypt utilizing the recently-made-available terrestrial FA gravity anomalies integrated with the satellite

gravity data. The terrestrial data used in this study, characterized by consistent gravity and height values, were exploited for the first time over the Egyptian territory. A quality control analysis has been done, for these terrestrial data, in order to exclude the gravity points, which have large discrepancies with respect to the SRTM-based DTM heights and/or positions in order to produce a homogeneous dataset that is used for the development of the combined gravity field modelling.

In regards to the investigated GOCE-based gravity data, namely the SPW-R5, DIR-R5, TIM-R5, and GOCO5S GGMs, the space-wise SPW-R5 solution, synthesized up to a SH d/o 200, is found to be the best model to closely-approximate the gravity field over Egypt, especially in terms of the long wavelengths components. Accordingly, the classical RCR method and LSC technique have been applied in order to reduce the order of magnitude of the terrestrial FA gravity observations and afterwards integrate them with satellite gravity data.

Correspondingly, a combined model in terms of FA anomalies has been developed and compared with respect to the state-of-art XGM2016 model, which was developed using a limited number of terrestrial gravity stations in Egypt, whose performance has been thoroughly investigated. In order to test the combined gravity model, the Bouguer anomaly data, which were calculated from the FA signal, synthesized from the combined model, were forward-modelled using the IGMAS+ 3D modelling along a transversal profile, P1, crossing the Nile Delta area from North to South.

The modelled gravity signals, derived from the calculated combined gravity model, are in a good agreement with the observed gravity signals producing residuals characterized by a low STD equivalent to 7.0 mGal compared with the residuals of the XGM2016 that exhibited a STD of 18.0 mGal. This emphasizes that the developed combined regional gravity model delivers significant improvements over the XGM2016 model as a result of jointly exploiting both the satellite and a large number of terrestrial gravity observations. The combined model would definitely be of added-value for geophysical and geodetic applications where no or only sparse ground data are available. In addition, the method may be useful when combining other heterogeneous datasets of different resolution e.g. onshore gravity data with offshore satellite data.

Chapter 3

Manuscript II: Inverse and 3D forward gravity modelling for the estimation of the crustal thickness of Egypt

Abstract

A 3D crustal density model for Egypt was compiled. It is constrained by available deep seismic refraction, receiver functions analysis, borehole, and geological data.

In Egypt, seismic data are sparsely and irregularly distributed. Consequently, we developed the crustal thickness model by integrating seismic and gravity data. Satellite gravity data was inverted to build an initial model, which was followed by a detailed 3D forward gravity modelling. The initial crustal thickness is determined by applying seismically constrained non-linear inversion, based on the modified Bott's method and Tikhonov regularization assuming spherical Earth approximation. Moreover, the gravity inversion-based Moho depth estimates are in good agreement with results of seismic studies and are exploited for the 3D forward modelling.

Crustal thicknesses range from 25 to 30 km along the rifted margins of the Red Sea, which thin toward the Mediterranean Sea. Thicknesses in southern Egypt reach values between 35 and 40 km. A maximum crustal thickness of 45 km is found in the southwestern part of Egypt. Within the Sinai Peninsula, the thickness varies from the shallow southern edge ($\sim$ 31 km) and increases toward the North ($\sim$ 36 km). Our model revealed a thick lower crust beneath the southern part of Egypt, which can be associated with the crustal modification that occurred during the collision of East Gondwana and the Saharan Metacraton along the Keraf suture zone during the final assembly of Gondwana in the Neoproterozoic. Finally, the isostatic implications of the differences between the seismic and gravity-derived Mohos are thoroughly discussed.

In conclusion, the developed 3D crustal thickness model provides high-resolution

Moho depth estimates that closely resembles the major geological and tectonic features. Also, the existing correlation between the topography, Bouguer anomalies, and Moho depths indicates that the investigated area is close to its isostatic equilibrium.

3.1 Introduction

The present-day structure and the dynamics of the lithosphere of Egypt and its adjacent regions are controlled by the relative motion of three major tectonic plates: the Eurasia, Africa, and Arabia. The interaction of these continental plate margins causes a complex geodynamic setting. Therefore, mapping Moho depths can help to understand the crustal structure, the degree and style of isostatic compensations of continental plates, by lithospheric modelling techniques.
Seismic data such as derived from deep seismic refraction/wide-angle reflection, receiver functions and ambient noise tomography permit to perform the most robust imaging of the subsurface, although they are sparsely distributed due to limited access to the desert of Egypt. Gravity data has better spatial coverage and distribution compared to seismic data and can, therefore, be considered complementary information to resolve the crustal density and thickness variations (Aitken, Salmon, and Kennett, 2013).

In general, high-resolution mapping of Moho depths is fundamental and leads to a better understanding of the geometrical structure of the subsurface, the geodynamical evolution of the study area and can be used for both the prediction and mitigation of geohazards, e.g. earthquakes. Moreover, the knowledge of a precisely modelled crust would increase the potential to target and extract natural resources as well as to understand regional dynamics. A better understanding of the deep structures can help to improve the heat flow modelling and the prediction of source rock maturity and hydrocarbon accumulations (e.g., Allen and Allen, 2005; Hantschel and Kauerauf, 2009; Bouman et al., 2015).

Regarding Egypt, a number of seismic studies have imaged the crust in the past (e.g., Makris et al., 1979; Makris, 1983; Rihm, 1984; Makris, Rihm, and Allam, 1988; Makris and Rihm, 1991; Rihm, Makris, and Moller, 1991; Dorre et al., 1997; Seber et al., 2000; Tealeb, Gharib, and Hussein, 2003; El-Khrepy, 2008; Salah, 2011; Abdelwahed, El-Khrepy, and Qaddah, 2013; Hosny and Nyblade, 2014; Hosny and Nyblade, 2016; Corchete et al., 2017). Most of these studies have explicitly focused on the northern and eastern parts of the country, i.e. the Red Sea and the Mediterranean Sea coastlines, respectively, while large data gaps away from the coast remain (Fig. 3.1).
This study exploits satellite gravity data as well as terrestrial gravity observations acquired over the study area, integrated with the results of the aforementioned major seismic experiments as physical constraints for the development of the crustal thickness model as well as to perform an interdisciplinary interpretation.

Since seismic data in Egypt are sparse and irregularly distributed, the main objective of this study is to develop a crustal thickness model for Egypt (Fig. 3.1) by integrating both seismic and gravity data. First, satellite gravity data is inverted in

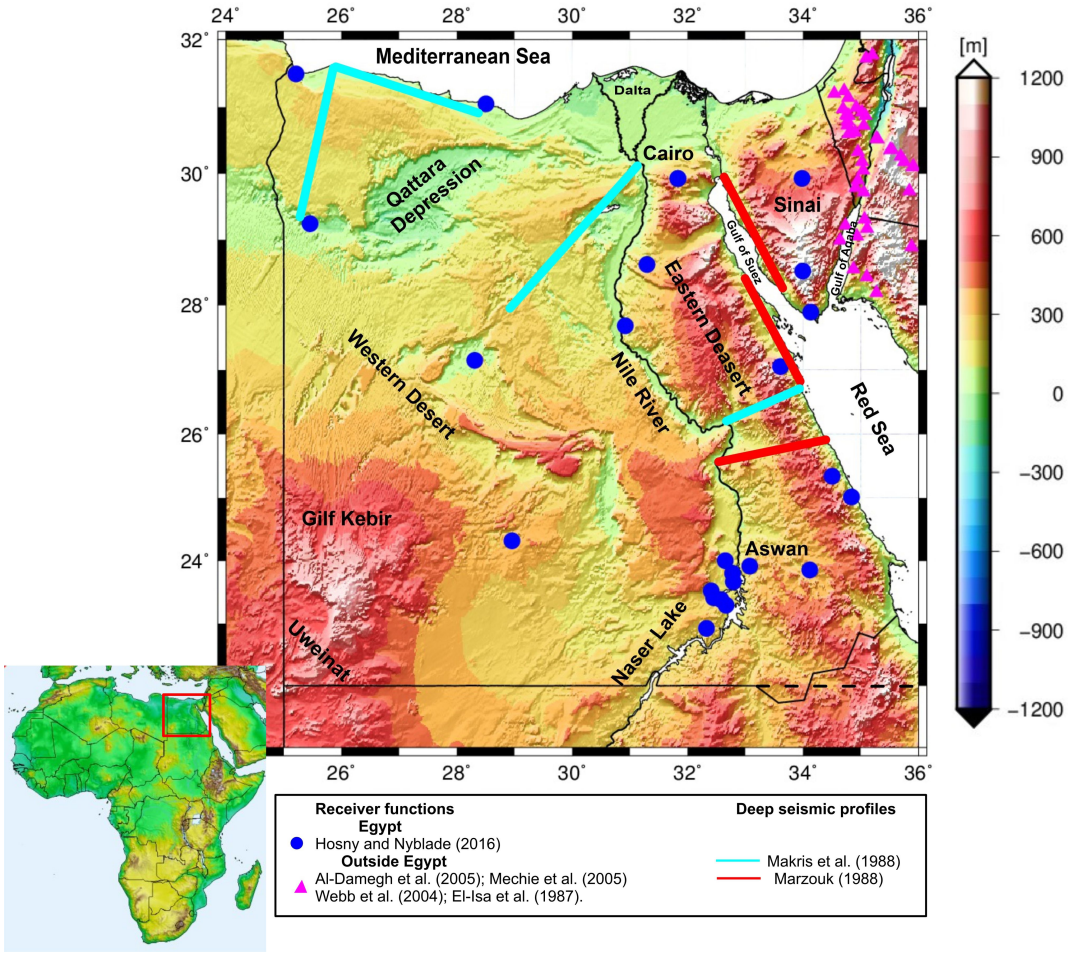

Figure 3.1: The geographic map of Egypt and the spatial location of the constraining geophysical data. Cyan lines show the location of deep seismic profiles from (Makris, Rihm, and Allam, 1988). Red lines show the location of the refraction seismic profiles from (Marzouk, 1988). Blue circles indicate the location of the receiver functions results inside Egypt from Hosny and Nyblade, 2016. Magenta triangles show the location of receiver functions result around Egypt from (El-Isa et al., 1987; Webb et al., 2004; Al-Damegh, Sandvol, and Barazangi, 2005; Mechie et al., 2005). The major geographic features are named and geographically positioned. The shaded digital elevation model in the background is derived from the ETOPO1 model (Amante, 2009).

order to have an initial crustal thickness map precedent to performing a detailed 3D forward gravity model constrained by independent information.

Because variations in the Moho boundary depth correspond to different geological terranes, we compare the Moho map with the major surface geological units within the study area.

This paper commences with a summary of Egyptian geological and tectonic settings in Sec. 3.2. The data exploited for the present and previous Moho depths estimates are thoroughly presented in Sec. 3.3. The implemented theory and methodology for the development of the gravity-based Moho model in addition to the isostatic state of the study area and the necessary corrections as well as the gravity inversion

and the compilation of the 3D forward gravity modelling are described in Sec. 3.4. The analyses and the final Moho model are presented in Sec. 3.5. The discussion is held in Sec. 3.6, while some relevant conclusions are drawn in Sec. 3.7.

3.2 Tectonic Settings and Previous Geophysical Studies

This section is dedicated to the description of the tectonic settings as well as the previous estimations of the Moho depths in the study area.

3.2.1 Tectonic and Geological Settings of Egypt

Egypt is primarily divided into four major provinces; the Arabian-Nubian Shield, stable shelf, unstable shelf, and the Gulf of Suez-Red Sea graben (Said, 1962). The Arabian-Nubian shield that consists mainly of Precambrian rocks, extends over large parts of the Eastern Desert, the southern Sinai Peninsula, and the extreme southern part of the Western Desert at the Uweinat area (southwest of Egypt). The stable shelf, located in the North and the West of the Arabian-Nubian Shield, exhibits gentle tectonic deformations, where the continental and epicontinental deposits such as the Mesozoic Nubian Sandstone mainly represent its sedimentary cover. The sedimentary sequence on the stable shelf is relatively thin of about 400 m near the Arabian-Nubian shield and increases to, as thicker as, 2500 m near the transition zone into the unstable shelf in the North. The Hinge Zone, located between the mobile shelf and the miogeosynclinal basinal area, is characterized by a rapid thickening of the Oligocene to Pliocene sediments and partially coincides with the present Mediterranean coastal area (Fig. 3.2).

However, in southern Egypt, a number of granitic outcrops have been interpreted to be part of the much older Saharan Metacraton. Fig. 3.2 displays a simplified geologic map of Egypt and the main tectonic provinces. The suture between the Neoproterozoic terranes to the East and the Metacraton to the West is marked by the Keraf shear zone. (Abdelsalam and Stern, 1996a; Abdelsalam and Stern, 1996b; Abdelsalam et al., 1998). On the one side, Phanerozoic sedimentary rocks overlie the Precambrian basement across most of the Egyptian territory. On the other side, Palaeozoic sandstones and shales are found at the base of the sedimentary section, which in many places are overlain by the Mesozoic sandstones, Paleogene and Neogene limestones, sandstones, and conglomerates, and unconsolidated Quaternary sediments.

3.2.2 Previous Moho Depths Studies of Egypt

The crustal thickness of Egypt has been previously investigated in a number of studies, summarised in Table 3.1 and Fig. 3.1. However, most of these studies focused on the northern and eastern parts of the country, along the Red Sea and the Mediterranean Sea, by elaborating the older seismic refraction, receiver functions studies, and ground-based gravity measurements. Specifically, most of such studies are based on seismological analyses, e.g., local earthquake travel time inversion (Abdelwahed, El-Khrepy, and Qaddah, 2013), seismic profiles (Makris et al., 1979; Makris, 1983; Gaulier et al., 1988; Marzouk, 1988; Makris and Rihm, 1991; Rihm,

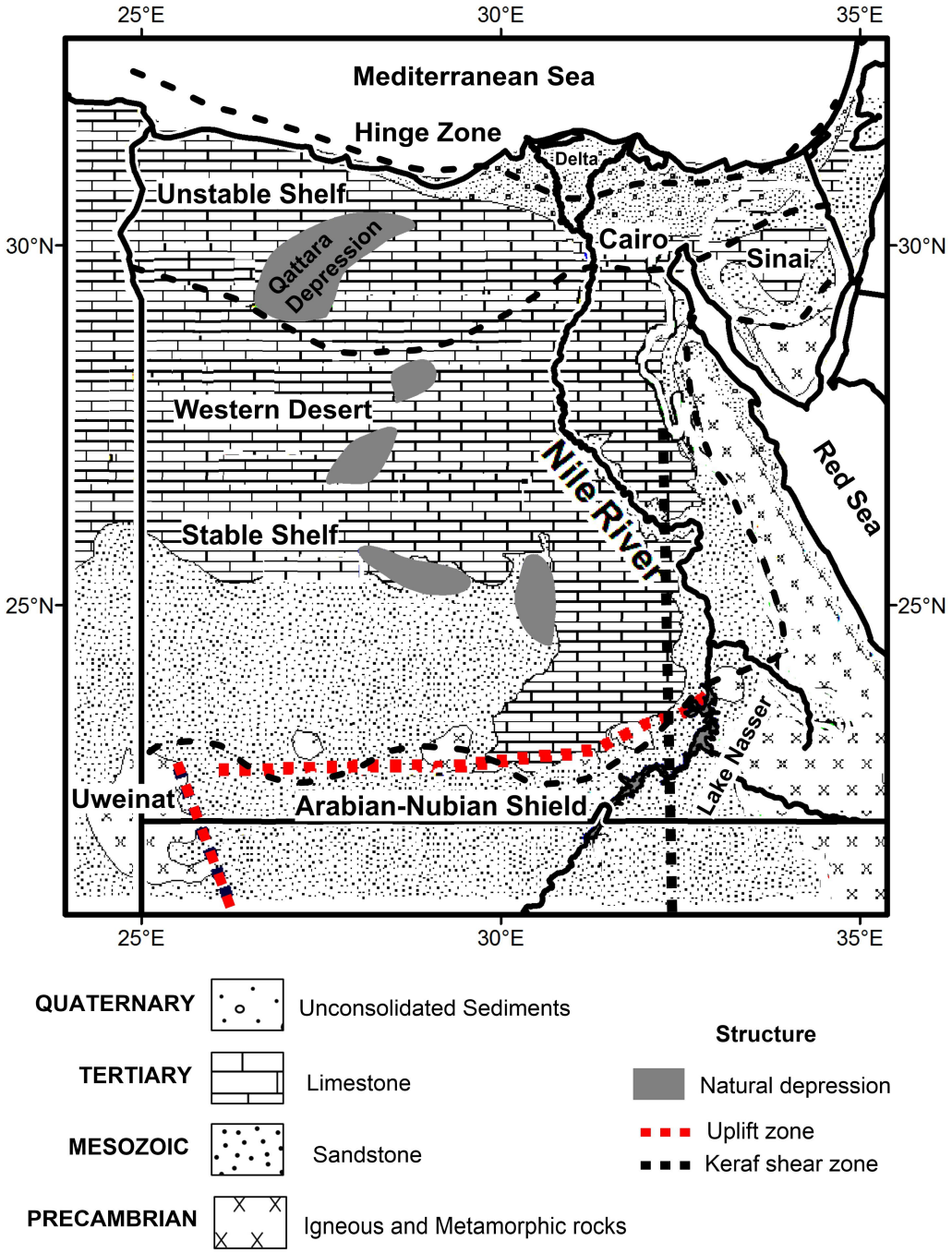

Figure 3.2: The simplified geologic map of Egypt, redrawn after the geological map of the Egyptian Geological Survey and Mining Authority 1981. Black dashed lines show the locations of the main tectonic provinces after (Said, 1962).

Makris, and Moller, 1991), or deep seismic sounding (Ginzburg et al., 1981; EL-Hadidy, 1995; Segev et al., 2006). (Corchete et al., 2017) determined the crustal and uppermost mantle structure in north-eastern Egypt based on the Rayleigh wave analyses. While, (Hosny and Nyblade, 2014) modelled P-wave receiver functions around Lake Nasser in southern Egypt, for a single station in north-eastern Egypt and they extended their research to include the all-broadband beneath all seismic

stations in Egypt (Hosny and Nyblade, 2016).

Table 3.1: Previous Moho depths estimates for Egypt (see Fig. 3.1). The methodology is also indicated; unit [km].

Area	**References**	**Method**	**Depth Estimates**
Sinai Peninsula	Marzouk, 1988	Seismic refraction	30-35
	Saleh et al., 2006	Gravity	31
	Abdelwahed, El-Khrepy, and Qaddah, 2013	Local earthquake travel time inversion	31-35
	Ginzburg et al., 1981	Deep Seismic Sounding	33-35
	Hosny and Nyblade, 2016	Receiver Functions	32-38
	Corchete et al., 2017	Rayleigh wave analysis	30-35
Northern Egypt and SE Mediterranean	Makris et al., 1991	Seismic refraction	30-32
	Segev et al., 2006	Deep Seismic Sounding	30-35
	Dorre et al., 1997	Gravity	30-32
	Abdelwahed, El-Khrepy, and Qaddah, 2013	Local earthquake travel time inversion	29-31
NW Red-Sea	Salah, 2011	Receiver Functions	31
Cairo	El-Khrepy, 2001	Seismic refraction	33
Fayoum	Makris et al., 1979	Seismic refraction	32.5
Dahshour	Makris et al., 1979	Seismic refraction	31-33
Middle Egypt	Marzouk, 1988	Seismic refraction	32
	Dorre et al., 1997	Gravity	30-32
	Abdelwahed, El-Khrepy, and Qaddah, 2013	Local earthquake travel time inversion	32-33

Continued on next page

Area	References	Method	Depth Estimates
	EL-Hadidy, 1995	Deep Seismic Sounding	31
Western Desert	Makris, Rihm, and Allam, 1988	Seismic refraction	33-35
	Dorre et al., 1997	Gravity	32-34
	Abdelwahed, El-Khrepy, and Qaddah, 2013	Local earthquake travel time inversion	38
Upper Egypt	Makris, Rihm, and Allam, 1988	Seismic refraction	34
	Dorre et al., 1997	Gravity	32-34
	Abdelwahed, El-Khrepy, and Qaddah, 2013	Local earthquake travel time inversion	35-40
	Hosny and Nyblade, 2016	Receiver Functions	35-40
Eastern Desert Northern Red Sea	Makris et al., 1991	Seismic refraction	30-35
	Rihm, Makris, and Moller, 1991	Seismic refraction	30-32
	Saleh et al., 2006	Gravity	31
	Abdelwahed, El-Khrepy, and Qaddah, 2013	Local earthquake travel time inversion	29-31

In addition to the seismic investigations, a number of gravity-based calculations of the crustal thickness have been reported. (Dorre et al., 1997) compiled a crustal thickness variation map for Egypt by use of 2.5D gravity models. They used the gravity data collected within the framework of the African Gravity Project (Fairhead et al., 1988), which encompasses both terrestrial and airborne measurements, and applied the 2D power spectrum analysis.

(Seber et al., 2000) estimated the crustal thickness of the Middle East and Egypt combining gravity data with refraction seismic profiles. Moreover, (Saleh, 2012) reported Moho depths along the Nile Delta utilising the 3D forward gravity and magnetic modelling constrained by the available seismic reflection and well logs data. After this brief overview of the past Moho calculations, the next section will describe the new gravity datasets exploited in our investigations to determine a country-wide Moho, which is a combination of terrestrial and satellite gravity data.

3.3 Database

This section is concerned with the description of the various gravity datasets used in this study and the procedure of data correction.

3.3.1 Gravity Data

Two different gravity field datasets were implemented: (1) a high-resolution combined (terrestrial and satellite gravity) dataset exploited for building the detailed 3D density model, (2) the Gravity field and steady-state Ocean Circulation Explorer (GOCE)-based dataset utilised for the initial Moho depth estimation via the gravity inversion.

High Resolution Gravity Data

A new combined regional gravity model has been developed for Egypt integrating the recently-made-available terrestrial free-air (FA) gravity anomalies with satellite-based gravity observations (Sobh et al., 2018). The terrestrial data used in this study, characterized by consistent gravity and height values, are exploited for the first time over the Egyptian territory.

Gravity Data Processing

In regards to the data processing, one has to consider that the gravity observations at the Earth's surface and the Earth near space vary from the theoretical "normal" field values. The signal magnitude is not caused only by the latitude effect but also the elevation of observational points, the density of the cap beneath the station in the subsurface, and the effect of the topographic/bathymetric masses in the vicinity/surrounding. After correcting the gravity measurements for the Earth tidal effects and the air pressure variations, the remaining time-invariable residuals of the measured signal are theoretically: the normal gravity (γ_0), the effect of topographic/bathymetric masses (δg_{TC}), the Bouguer slab (δg_{BPL}), the elevation effect (FA term) (δg_{FA}), and the effect of the crustal root (δg_R).

The common representations of the gravity measurements, as maps and profiles, depend on the applied corrections to the gravity measurements. From all the measured values, the normal gravity value is subtracted and therefore the term "gravity anomaly" is defined. This is simply the difference between the observed and the "normal" gravity values.

In geophysics, the main three anomalies, i.e. the FA anomaly, Bouguer anomaly (BA), and isostatic anomaly (ISA), are distinguished in order to define the gravity field in terms of the height of the observations (e.g. (Naudy and Neumann, 1965; LaFehr, 1991; Li and Götze, 2001; Hackney and Featherstone, 2003; Zaki et al., 2018b) and many others).
Using the δg_R, which accounts for the effects of a mountain root, one can easily define the FA, BA and isostatic anomalies (ISA) as follow:

$$FA = \Delta g_o^{'} = \delta g_{obs} + \delta g_{FA}[+g_{TC}] - \gamma_0 \tag{3.1}$$

$$BA = \Delta g_o^{''} = \delta g_{obs} + \delta g_{FA} + \delta g_{TC} + \delta g_{BPL} - \gamma_0 \tag{3.2}$$

$$ISA = \Delta g_{ISA} = \delta g_{obs} + \delta g_{FA} + \delta g_{TC} + \delta g_{BPL} + \delta g_R - \gamma_0 \tag{3.3}$$

Based on the objective of the survey, specific corrections must be considered, in order to process the observations, g_{obs}. The calculation of the topographic reduction (δg_{TOP}) necessitates the precise knowledge of the topography/bathymetry and surface densities, which is commonly given in terms of a digital elevation model (DEM), is normally calculated using an area of influence, e.g. a surrounding circular area of $50 - 167$ km radius (e.g. (LaFehr, 1991; Hinze. et al., 2005). However, (Mikuška, Pašteka, and Marušiak, 2006) studied the so-called "long distant relief effects" and recommended the calculation of the effects of all the topographic masses on Earth. The gravity effects of a Bouguer slab with a certain thickness value, which is defined by the difference between the physical station height and a reference level, which is normally taken as the geoid, should always be calculated as a spherical cap (e.g. (Baschlin, 1948)). For smaller areas (with an influence radius $R < 20$ km) and moderate terrain roughness, the Bouguer slab can be simply calculated by:

$$\Delta g_{BPL} = 2\pi G\rho(H_S - H_B) \tag{3.4}$$

where G is the gravitational constant $(6.672 \cdot 10^{-11})(\mathrm{m}^3{\cdot}\mathrm{s}^{-2}{\cdot}\mathrm{kg}^{-1})$, ρ is the crustal density (2670 kg·m^3), H_S is the topographic height or the bathymetric depth of the gravity station, and H_B is the reference height (usually it refers to the geoid).

In the last step, the FA effects, δg_{FA}, is calculated using the "normal gradient" relationship, where (0.3086 mGal/m): $g_{FA} = 0.3086 \cdot (H_S - H_B)$ mGal/m, (1 mGal $= 1 \times 10^{-5}$ m·s^{-2}).

It is worth mentioning that the implementation of a constant gravity gradient is limited to large-scale investigations and it has to be replaced by equivalent values of the derivation of closed-mathematical expressions of the normal gravity, which is always latitude and height dependent.

The BA field is nothing but correcting the FA gravity anomaly signal for the topography correction (TC) before being used in the modelling step, as follows:

$$BA = FA - TC \tag{3.5}$$

The TC signal has been computed, using the gravity terrain effects (GTE) package (Sampietro et al., 2016; Capponi, Mansi, and Sampietro, 2018) with a continental crustal density of 2670 kg·m^3 and 1630 kg·m^3 for the offshore. For each station, the

gravitational effect of the prisms inside a circle with radius (167 km) around the station is computed, where all the first and second spherical corrections of the Earth's shape (Braitenberg et al., 2016; Mansi, 2016) have been considered.

The FA values of the study area, shown in Fig. 3.3-a, range between -45 and 110 mGal and they are found to be strongly correlated with the topography. The Arabian-Nubian shield, which is a stable tectonic unit that consists of the exposed basement rocks in the Eastern Desert, the southern part of the Sinai Peninsula and the isolated outcrops in southern Egypt are characterized by positive FA anomalies. The north-western part of Egypt is characterized by a positive FA anomaly (up to 70 mGal) decreasing towards the Mediterranean coast (45 mGal). The Nile Delta is characterized by a negative FA anomaly (~ -27 mGal) that increases towards the Mediterranean coastline ($\sim$ 30 mGal). On the meanwhile, the FA gravity anomalies along the Nile River have negative values (~ -15 mGal). A series of elongated gravity high-values parallel to the overall Red Sea trend is located outside the axial rift.
The computed TC signal varies between -10 and 120 mGal (Fig. 3.3-b), which naturally shows a strong correlation with the topography as it solely depends on the elevation. The Uweinat area, the locality of high mountains, has the highest TC value ($\sim$ 120 mGal), where the Qattara Depression, where the lowest altitude values are found, has the lowest altitude values has a negative value (~ -2 mGal). The BA, shown in Fig. 3.3-c, was obtained subtracting the TC values from the FA gravity signal.

The error of the calculated BA signal is estimated propagating the uncertainties of the gravity measurements and TC. The exploited high-resolution gravity dataset consists of a total number of 56250 ground stations integrated with satellite-based gravity data via the classical remove-compute-restore technique and the collocation procedure. The data provider has suggested an accuracy of 1.0 mGal for such terrestrial data. However, it is expected that the accuracy of the provided FA gravity anomalies, due to the noticeable high-inhomogeneity should be substantially low ($\sim$ 5 mGal) over the majority of the study area (Sobh et al., 2018).

The TC signal has an error of about 2.0 mGal, which comes from the mean error of the Shuttle Radar Topography Mission (SRTM) equivalent to 6.0 m, as reported by (Rodriguez, Morris, and Belz, 2006). A note must be taken that the computed TC assumed a constant density for all rock masses above the mean Sea level, which might introduce additional errors.

In general, the continental part of the study area is characterized by negative BA values, whereas the northern part, along the coastal area of the Mediterranean Sea, is characterized by positive values ($>$ 50 mGal). In the meanwhile, the Nile Delta is characterized by a pronounced negative BA in the East-West direction (-35 mGal), whereas the northern delta has positive anomalies ($>$ 50 mGal) that occupy the coastal area of the Mediterranean Sea. The Southwestern part of Egypt has a negative BA footprint that coincides with the Uweinat area.

The highest mountains, located at the shoreline of the Red Sea (altitudes greater than 1000 m), are characterized by negative BA values that range between -30 to

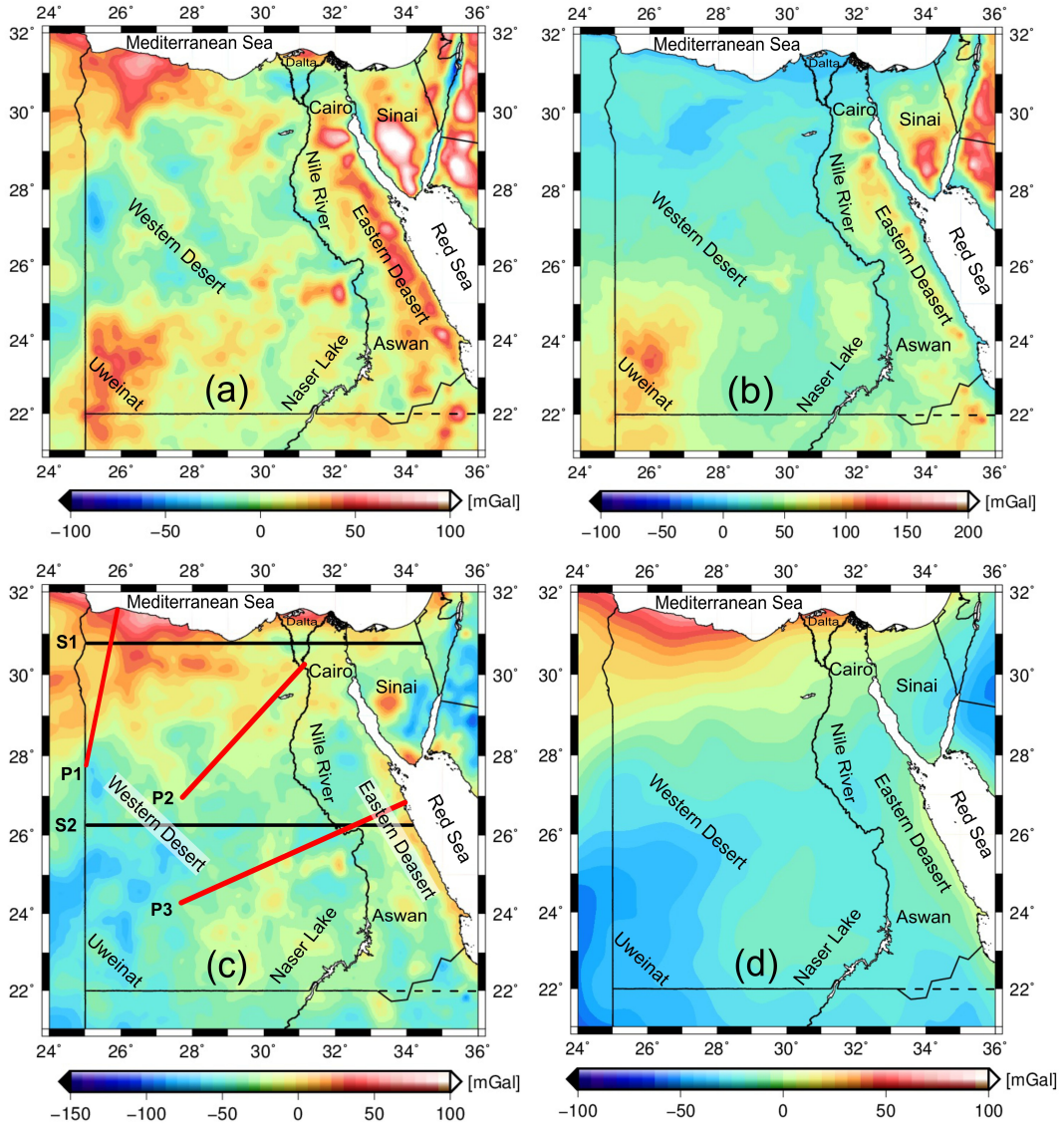

Figure 3.3: (a) The Free-air anomaly from the combined regional gravity model (Sobh et al., 2018), (b) the topographic correction computed using the GTE software (Sampietro et al., 2016; Capponi, Mansi, and Sampietro, 2018), (c) the Bouguer gravity anomaly obtained by subtracting (b) from (a), and (d) the GOCE-based synthesised satellite Bouguer gravity signal; unit [mGal]. This gravity anomaly signal of the panel (d) has been inverted for the Moho surface estimation. Red solid lines show the location of three profiles taken, where the seismic refraction profiles were carried out. Black lines show the location of the representing cross-sections S1 and S2. The major geographic features are named. unit [mGal].

−10 mGal. These BA values reveal that the crust attains its maximum thickness below the Red Sea Mountains and considerably thins towards the Red Sea Rift (Saleh et al., 2006).

GOCE Satellite Data

The Gravity Observation COmbination fifth release (GOCO5S) model (Mayer-Güerr, 2015) is used to synthesize the BA signal at a constant altitude at 50 km above the ellipsoid. The GOCO5S model is developed up to a spherical harmonic d/o 280 and

was built using the full GOCE mission data with a spatial resolution of about 70 km. The synthesized BA signal is then inverted to obtain initial estimates of the Moho depths.

The TC for the GOCE-based data was computed using the Tesseroids (Uieda, Barbosa, and Braitenberg, 2016) using the 1 arc-min spatial resolution ETOPO1 model (Amante, 2009). A continental crustal density of 2670 kg·m^3 and 1030 kg·m^3 for the offshore were applied. A 5-degree padding has been used in all directions, extending the actual digital elevation model, i.e. topography, of the study area to avoid any edge effects even for the far-field topography (Szwillus, Ebbing, and Holzrichter, 2016; Mansi, Capponi, and Sampietro, 2018; Sampietro, Mansi, and Capponi, 2018b; Sampietro, Mansi, and Capponi, 2018a; Zaki et al., 2018a). The BA signal calculated from GOCE data is reported in (Fig. 3.3-d).

3.3.2 Constraining Data for the 3D Modelling Procedure

The initial model consists of four layers, namely, the sediments, two different crustal domains, and the upper mantle. Moreover, the initial model takes into consideration all the significant geological and geophysical observations. Subsequently, the free parameters of the initial model can be modified until the forward computed gravity signal best-fit the measured values.

Geometrical Constraints

The 3D model is initially constrained by the deep seismic profiles, receiver functions studies (Fig. 3.1), drilled boreholes, and geological information. Moreover, the gravity inversion-based Moho and the isostatic Moho interface are used to constrain the Moho depths in regions where seismic observations are null. Besides, the sedimentary layer is constrained by the thickness data of the sediments retrieved from the global sediment thickness (Fig. 3.4) compilation of the Exxon Tectonic Map of the World (Exxon, 1985).

Crustal Density Constraints

The densities of the crustal models of Egypt were defined exploiting the rock density values of the various studies, summarised in Table 3.2. The density values were carried out in the northern part of the Egyptian Western Desert, the Nile Delta, and the Mediterranean Sea. Also, the P-wave velocities of (Hosny and Nyblade, 2016) were converted densities by applying the nonlinear relationships of (Christensen and Mooney, 1995).

3.3.3 Upper Mantle Density Constraints

The initial density of the upper mantle is obtained based on the S-wave tomography model of (Schaeffer and Lebedev, 2013a), which is converted to densities in two steps: first, the P-wave velocities (v_p) were calculated from the S-wave velocity (v_s), then, in turn, the obtained P-wave velocities were converted into densities (Kaban et al., 2016). The upper mantle density structure at 50 km depths is shown in Fig. 3.4-b. The model demonstrates very small density changes.

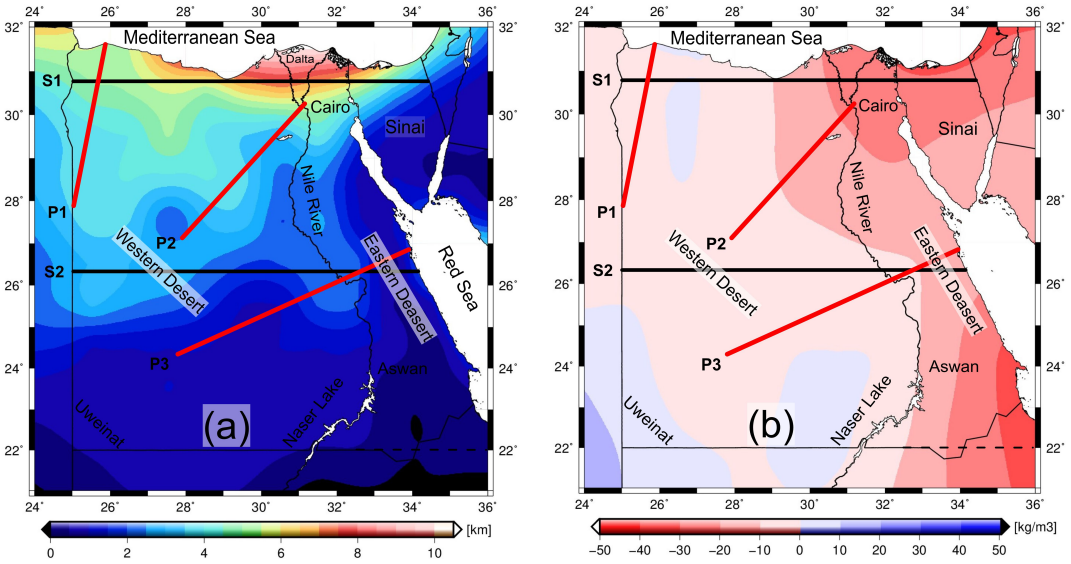

Figure 3.4: The model constraints. (a) Sediment thickness from Exxon, 1985; unit [km] and (b) Upper mantle density configuration at 50 km depth, converted from the SL2103Sv model (Schaeffer and Lebedev, 2013a); unit [km·m^{-3}]. The major geographic features are named and geographically positioned. Red solid lines show the location of three profiles taken, where the seismic refraction profiles were carried out. Black lines show the location of the representing cross-sections S1 and S2.

Table 3.2: Previous Moho depths estimates for Egypt (see Fig. 3.1). The methodology is also indicated; unit [km].

Layer	**Density [km·m^{-3}]**	**Reference**
Sediments	2400	(Ginzburg and Ben-Avraham, 1987; Makris et al., 1994)
Upper crust	2700	(Ginzburg and Ben-Avraham, 1987; Abdelrahman, Refai, and El-Ghalban, 1988; Makris et al., 1994)
Lower crust	2900	(Jacobs, Russell, and Wilson, 1959; Makris et al., 1979; Ginzburg and Ben-Avraham, 1987; Prodehl and Mechie, 1991; Rihm, Makris, and Moller, 1991; Makris et al., 1994)
Upper mantle	3250 – 3300	(Jacobs, Russell, and Wilson, 1959; Ginzburg and Ben-Avraham, 1987; Makris et al., 1994)

Accordingly, the density of the lithospheric upper mantle was assumed to be laterally homogeneous with a density value of 3300 km·m^{-3} as the main focus is on the crustal structure itself with the exception towards the Red Sea in the W-E direction.

3.4 Methods

The space-wise approach (Sampietro et al., 2017) has been applied for the data integration, then the 3D density modelling, which incorporates forward and inversion

techniques, was performed, where the geometry for the structural and the density model have been defined.

3.4.1 Gravity Inversion

In order to get preliminary information about the crustal thicknesses of Egypt, a regularized non-linear gravity inversion was applied (Uieda and Barbosa, 2017). The method is based on the modified Bott's method (Silva, Santos, and Gomes, 2014a) with the Tikhonov regularization to stabilize the computed solutions in a two-step procedure. In the first step, the regularization parameters are determined using a predefined set of initial values for the mean depth and the density contrast of the Moho discontinuity. In the second step, the gravimetric inversion is carried out for a set of different mean depth and density contrast values, where the best estimate, i.e. the final solution, is obtained after the cross-comparison with the seismic-based Moho depth estimates is held.

For such a purpose, the GOCE- synthesized BA signal at an ellipsoidal height of 50 km is inverted. The results of the gravity inversion are controlled by two parameters namely, the Moho reference depth and the density contrast between the crust and the upper mantle. Therefore, the available seismic data displayed in Fig. 3.1, were used to validate the obtained results by examining all the possible combinations of the nine Moho reference depth values that range from 20 to 40 km with a 2.5 km incremental step, and the seven density contrast values that range from 200 to 500 km·m^{-3} with 50 km·m^{-3} intervals. Fig. 3.5 visualises the Mean Square Error (MSE) values with respect to the seismological Moho dataset. The optimal MSE value has been obtained using the 32 km reference depth and the 450 km·m^{-3} density contrast. The gravity residuals appear to follow a Gaussian distribution with a mean of 0.23 mGal and a standard deviation (STD) of 2.56 mGal. The obtained Moho depths model varies between 20 km and 40 km as shown in Fig. 3.6.

3.4.2 3D Modelling with IGMAS+

In order to compile a 3D model for Egypt, the Interactive Geophysical Modelling Assistant (IGMAS+) software has been used, which is a 3D geo-modelling package developed based on the simultaneous forward modelling of gravity, gravity gradients, and magnetic fields (e.g. Götze and Lahmeyer, 1988; Schmidt et al., 2010; Schmidt, Barrio-Alvers, and Götze, 2015; Alvers et al., 2014; Alvers et al., 2015; Götze, 2020). The IGMAS+ platform offers an interdisciplinary 3D modelling approach integrating independent seismic, boreholes, and geological datasets, thusly reducing the ambiguity of the potential field inversion. The model consists of several parallel cross-sections, in which the vertical sections run from the East to the West direction with a separation offset of 50 to 100 km. The implemented IGMAS+ algorithm automatically eliminates the edge effects of a limited 3D model.

3.5 Results

The gravity-based results are reported and then cross-compared with the results of some of the previous seismic data sets (Sec. 3.2.2.). Such a comparison is thoroughly done along 3 longitudinal profiles.

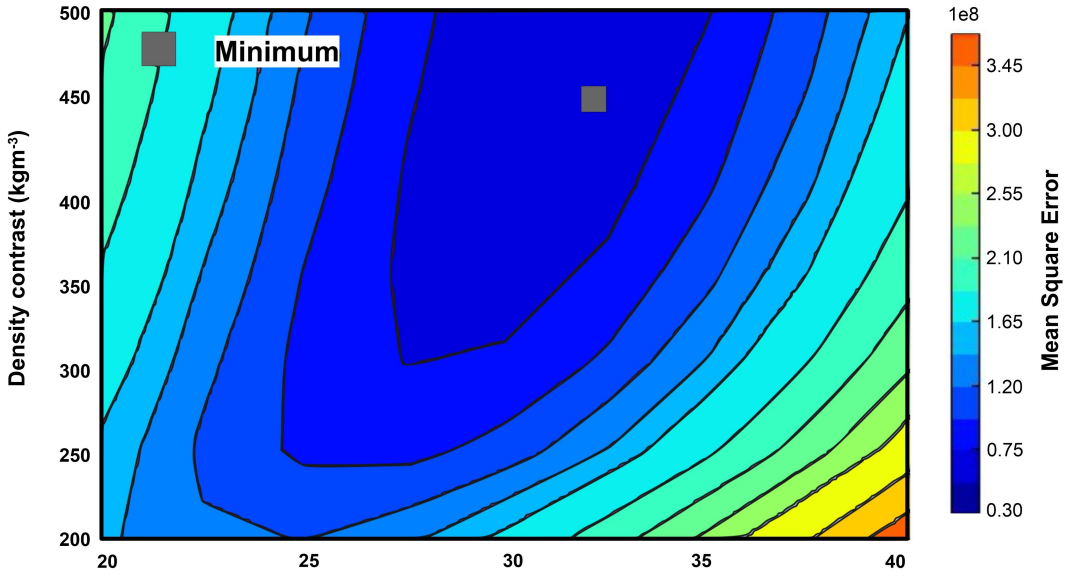

Figure 3.5: The validation step exploited to determine the Moho reference level (Z_{ref}) and the density contrast ($\Delta\rho$). The colours represent the Mean Square Error. The best-fit model is marked by the grey rectangular, which indicates a density contrast of 450 km·m^{-3} and a Moho reference depth of 32 km.

3.5.1 Isostatic Gravity Anomaly

In order to calculate the isostatic state of the lithosphere in Egypt, the Airy-isostatic correction has been applied to the BA values, which removes a significant part of the effects of the dominating deep density heterogeneity of the BA signal. This correction assumes that the crust is compensated by variations of the Moho depths. First, the root effects were computed and removed from the BA signal to obtain the residual isostatic gravity field. The Airy-isostatic Moho was then calculated using the topography/bathymetry data provided by the ETOPO1 model (Amante, 2009). The estimated Moho depths model (Fig. 3.7-a) ranges from 30 to 35 km in most parts of Egypt (e.g., (Abdelwahed, El-Khrepy, and Qaddah, 2013; Hosny and Nyblade, 2016). For that reason, a reference Moho depth is set to 32 km.

$$M_{iso} = Moho_{ref} + \frac{\rho_m}{\rho_m - \rho_c} * A_{topo} \tag{3.6}$$

where ρ_c and ρ_m are the crust and mantle density, respectively, the $Moho_{ref}$ is the Moho reference depth, and A_{topo} is the equivalent topography, which is calculated to account for the areas below the sea level:

$$A_{topo} = k * t \tag{3.7}$$

where $k = 1$ km·m^{-3} for the onshore regions and $k = \frac{(2670-1030)}{2670}$ km·m^{-3} for the offshore area. The Moho density contrast 450 km·m^{-3}, a value of which generally corresponds to the petrological data (Rabbel, Kaban, and Tesauro, 2013).

For the crustal structure, if the implemented isostasy model-related parameters are correct, the positive values of the residual field will indicate a thinner and/or a denser crust than assumed, the negative values will infer a thicker and/or a less

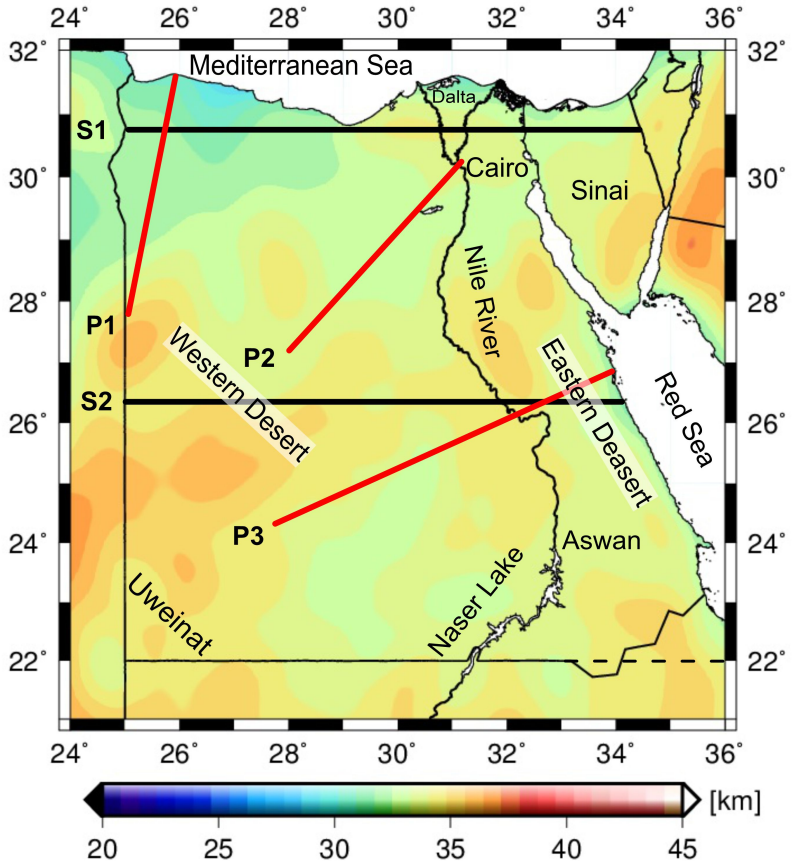

Figure 3.6: The Moho depth estimates obtained by inverting the GOCE gravity data after applying the topographic correction, of GOCE, with a reference depth of 32 km and a density contrast equivalent to 450 km·m^{-3}. The major geographic features are named and geographically positioned. Red solid lines show the location of three profiles taken, where the seismic refraction profiles were carried out. Black lines show the location of the representing cross-sections S1 and S2; unit [km].

dense crust.

Within the estimated residual isostatic anomalies (Fig. 3.7-b), several features are detected: (i) negative residuals are observed beneath the Nile Delta. Possible explanations could be that this area has thick sediments, of which whose effects are not fully removed from the observed BA signal, (ii) the existence of a positive anomaly along the coast of the Mediterranean Sea in the north-western desert, which could be related to some denser bodies located in the crystalline crust, or might be related to the subduction complex of the African lithosphere under the Eurasia. The high topography along the Red Sea coast is not isostatically compensated on a local scale, according to insignificant positive isostatic anomalies. Beneath the Uweinat area, a positive anomaly is observed, which might be linked to a thicker crust compared to the value considered within the model setup.

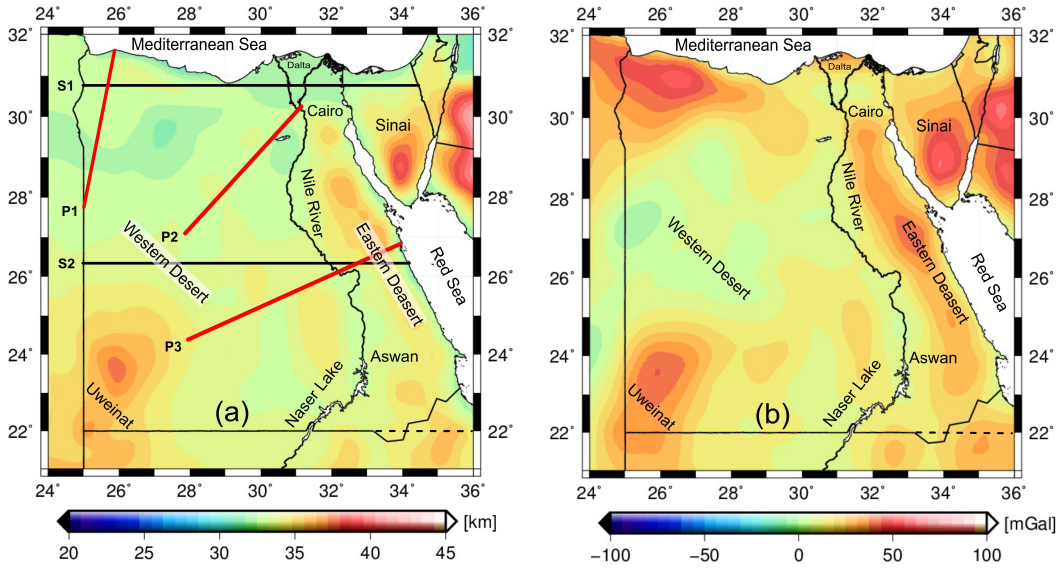

Figure 3.7: (a) The Airy-isostatic Moho depth estimates assuming density contrast of 450 kg·m^{-3} between the crust and the mantle, and a reference depth of 32 km; unit [km] and (b) Isostatic gravity residual; unit [mGal]. The major geographic features are named and geographically positioned. Red solid lines show the location of three profiles taken, where the seismic refraction profiles were carried out. Black lines show the location of the representing cross-sections S1 and S2.

3.5.2 Modelling Prerequisites

As a first step, all the available constraints are used to build up the initial model, whose gravity responses have been computed without any changes to the constrained layers (Sediments and Moho topography). The calculated gravity signal deviates from the observed field represented by the high residual gravity field. Therefore, the initial model was poorly explained the gravity data.

A tuning process has to be conducted by carefully shifting both layers surface (the Moho depths and sedimentary thickness) to improve the t of the gravity signal. The initial model has been carefully modied at every trial except when the Moho is constrained by seismic data and/or when the basement is constrained by borehole information. The density contrast between the crystalline crust and the sediments, caused shorter wavelengths gravity anomalies than those of deeper density contrasts, for example, in the crystalline crust or the upper mantle. From the modelled BA gravity map, shown in Fig. 3.8-a, the main features on both maps, the measured and the modelled gravity signal, are cross-comparable with small noticeable differences in shape. The spatial distributions of the residual gravity anomalies are reported in Fig. 3.8-b. The average mist between the measured and calculated anomalies reveals a correlation coefcient of 0.91 and a STD of 10 mGal, which is an acceptable value for regional gravity field modelling.
The gravity response of the modelled sediments thickness was calculated and presented in Fig. 3.9-a. In the southern part and along the Red Sea Mountains, the gravity response ranges between -5 and -10 mGal and it increases northward and toward the Nile Delta and the Mediterranean Sea Cost. Along the Nile Delta, where the sediments thickness reaches 9 km, the gravity response increases to -90 mGal.

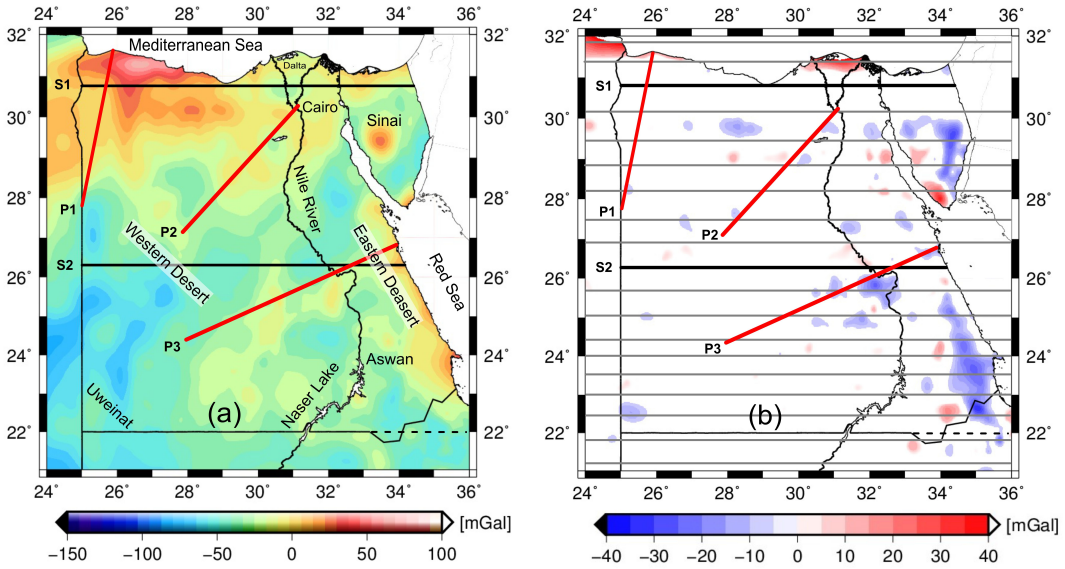

Figure 3.8: (a) The calculated Bouguer gravity map for Egypt and (b) The gravity residuals of the resulted model. Grey lines show the location of modelling cross-sections for the triangulation of the 3D density model. The major geographic features are named and geographically positioned. Red solid lines show the location of three profiles taken, where the seismic refraction profiles were carried out. Black lines show the location of the representing cross-sections S1 and S2; unit [mGal].

Since the sediment thickness map has a coarse resolution of 1° compared to the gravity data that has a finer resolution, uncertainty is introduced by the interpolation of the sedimentary map.

In Fig. 3.10 and Fig. 3.11 , only five out of a total number of 18 vertical cross-sections, of the final model, are displayed. Two of them are running in the E-W direction where the other three profiles coincide with the seismic lines.

East-West Profiles of the 3D Density Model

The profile S1, see Fig. 3.10, is realized along the W-E direction over a distance of about 1000 km, on which its gravity model is shown in Fig. 3.10-a. The undulation of the short wavelengths is due to the variations of the sediment thicknesses, whereas the western part has a sedimentary layer of 4 km thick increasing towards the Nile River then decreases toward the eastern direction that coincides with the Red Sea Mountains. In addition, the final model confirms the presence of a steep increase in the crustal thickness toward the East close to the Red Sea coastline. The estimated Moho depths range between 33 and 35 km at the West direction and gradually decrease and get steeper and/or shallower close to the Red Sea coastline, with a value of about $28 - 30$ km.

The profile S2, demonstrated in Fig. 3.10, is oriented in W-E direction also to the north of the study area. The western part is characterized by deep sediments along the Mediterranean Sea coastline, whose thickness increases toward the East direction reaching a maximum value of about $\sim 7 - 8$ km beneath the Nile Delta. The Moho depth is clearly shallow at the western part, which coincides with the

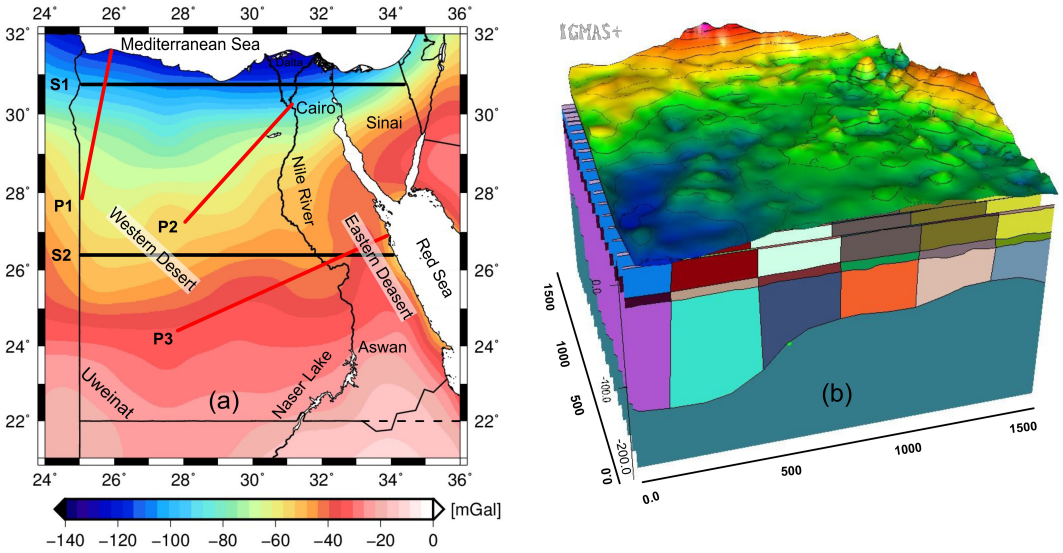

Figure 3.9: (a) The gravity response of the sediments thickness. The gravity response increase with the sediment thickness; unit [mGal]. (b) a three-dimensional perspective view of the IGMAS+ model with the Bouguer gravity anomaly on top. The major geographic features are named and geographically positioned. Red solid lines show the location of three profiles taken, where the seismic refraction profiles were carried out. Black lines show the location of the representing cross-sections S1 and S2.

Mediterranean Sea coastline, and then increases toward the East beneath the Nile Delta reaching values up to 32 km, and then it slightly gets shallower to the further Westside.

Vertical Cross-Sections of the 3D Density Modelling along Seismic Profiles

The three cross-sections are taken, where the seismic refraction profiles were carried out from the final 3D model.

The profile P1 extends from the Mediterranean Sea coast to the Egyptian-Libyan border. It stretches in the NW-SE direction, see Fig. 3.11-a, for about 450 km through the topographic feature of the Qattara Depression. Toward the Mediterranean coast, the observed gravity values increase with the increase of the thickness of the sediments and coincide with the thin Moho thickness of about $\sim$ 28 km with significant differences with respect to the isostatic Moho while being in a good agreement with the seismic-based Moho values.

The trending profile P2 extends from the Western Desert, oriented in a SW-NE direction, crosses the northern part of Egypt and ends at Cairo (Fig. 3.11-b). This profile corresponds to the seismic refraction profile of (Makris, Rihm, and Allam, 1988), see the Cyan dotted line in Fig. 3.1 The Moho depth below the Western Desert is 33 km that decreases eastward reaching a depth of 30 km beneath Cairo. The modelled Moho along this profile is in a good agreement with the gravity inverted Moho (blue dotted line) but in the meanwhile is characterized by small discrepancies with the isostatic Moho (red dotted line) of about $\sim$ 2 km indicating that the area is close to

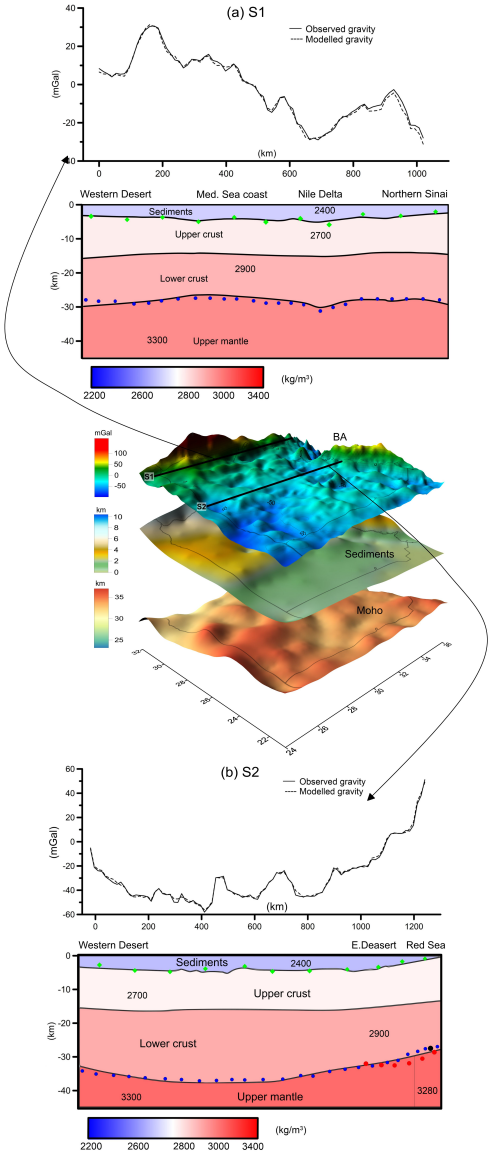

Figure 3.10: (a and b) The East-West vertical cross-sections of the 3D density model S1 and S2, respectively. The 3D Moho and the modelled sediment interfaces setting up the model, as well as the measured Bouguer anomaly are shown in (c). The upper part show gravity eld undulations, the solid line indicates the observed gravity field, and the dashed line indicates the modelled gravity field. The lower part shows the density structure of the lithosphere, the thick black lines represent the layers boundary. Green diamonds show the location of sediments from (Exxon, 1985); Blue dots show the location of gravity inverted Moho depths; Red dots show the location of the deep seismic profiles from (Makris, Rihm, and Allam, 1988); and Black dots show the location of the receiver function results from (El-Isa et al., 1987; Webb et al., 2004; Al-Damegh, Sandvol, and Barazangi, 2005; Mechie et al., 2005) according to the location of the cross-section.

its isostatic equilibrium state.

The profile P3 that extends in the SW-NE direction, runs along the seismic refraction profile of (Makris, Rihm, and Allam, 1988) from the Western Desert across the

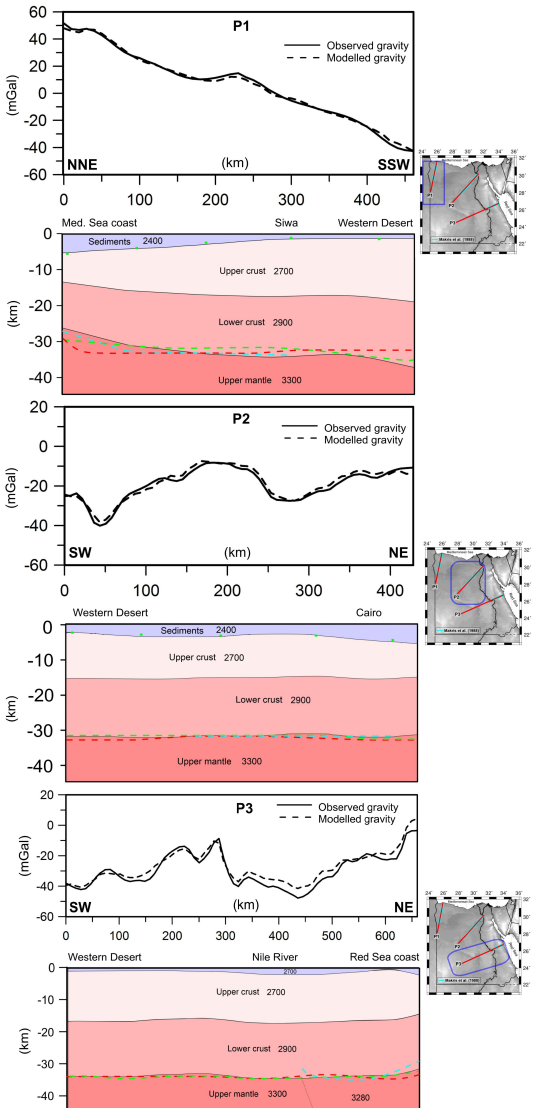

Figure 3.11: The vertical cross-sections of the 3D density model along seismic lines P1, P2 and P3, respectively. The upper panel shows gravity eld undulations, the solid Black line indicates the observed gravity field, and the Black dashed line indicates the modelled gravity field. The lower panel shows the density structure of the lithosphere, the black lines represent the layers boundary. Green diamonds show the location of sediments from (Exxon, 1985); Green dashed lines show the location of gravity inverted Moho depths. See Figure 6; Red dashed line indicates the Airy isostatic Moho; Cyan dashed lines show the location of the deep seismic profiles from (Makris, Rihm, and Allam, 1988).

Nile River and the Eastern Desert and ends at the Red Sea coastline, see Fig. 3.11-c. Westward, the crustal depth below the Western Desert is about $\sim$ 33 km and gradually decreases to reach a value of $\sim$ 31 km then increases eastward to reach its maximum value of $\sim$ 35 below the Red Sea hills. The Moho depths decrease towards the Red Sea coastline to a value of about $\sim$ 28 km. Our Moho depths estimation is in a good agreement with the seismic Moho illustrating a small discrepancy along the Red Sea coast.

The Moho depth increases south-westward reaching a value of 31 km beneath

the Siwa Oasis then gradually increases toward the south-west up to 35 km with a good agreement with the gravity inverted Moho value.

3.6 Discussion

The obtained gravity-based Moho depths results are cross-compared with the previous seismic-based estimates, both at local and regional scales.

3.6.1 Moho Depths Estimates Compared with the Main Geological Units

The residuals of our final Moho depth estimates compared to the local and global Moho values are displayed in Fig. 3.12. The Moho depths map is overlying the main geological units in the study area, as seen in Fig. 3.12, the Moho depth varies spatially between 25 and 45 km throughout Egypt. Generally, areas with a significant Moho depth gradient correlate well with the major tectonic boundaries. The deepest Moho value was found along the Uweinat Mountains, reaching a depth value of 45 km. The pronounced Moho depth around Naser Lake in Southern Egypt is interpreted to be along the mapped Precambrian suture zone, the Keraf shear zone, which was likely formed during the collision between east Gondwana and the Sahara metacraton during the final assembly of Gondwana in the Neoproterozoic (Abdelsalam and Stern, 1996a; Abdelsalam and Stern, 1996b; Abdelsalam et al., 1998; Hosny and Nyblade, 2016). These tectonic units are associated with the "Arabian-Nubian shield". The map clearly reveals both the northward and the eastward crustal thinning trends toward the Mediterranean Sea and the Red Sea, respectively. Eastward, the Moho under the Eastern Desert is situated at a depth of $\sim$ 31 km.

The crustal thickness varies within the Sinai Peninsula from the southern edge to the north side, which provides evidence for the presence of an Early Mesozoic passive margin with thinned continental crust in the north of Sinai. The shallower depth of the Moho in the southern Sinai reflects a thinning phenomenon related to the rifting process in the Gulf of Suez. Linking our findings to the tectonic map of Egypt, the final Moho model presents a rapid thinning crust toward the Mediterranean Sea, which coincides with the Hinge Zone.

3.6.2 Comparison with Local Seismic-Based Moho Depths

Our estimated Moho depths are in good agreements with those obtained from seismic investigations, regardless that the available seismic points are sparsely distributed. Fig. 3.13-a displays the differences between the seismic-derived Moho depths and gravity-derived model (Fig. 3.12). The differences approximately range between -5.0 to 7.5 km (Fig. 3.13-b) with a mean value of 0.52 km and a STD of 2.6 km. Along the Red Sea coastline, our model slightly overestimates the Moho depths of approximately 31 km with a difference of 5 to 7 km. On the other hand, our model could produce more reliable depths estimation, when the coverage of the seismic stations is very limited, and from the literature, acceptable Moho depth discrepancies can reach 10 km (Knapmeyer-Endrun, Krüger, and Group, 2014).

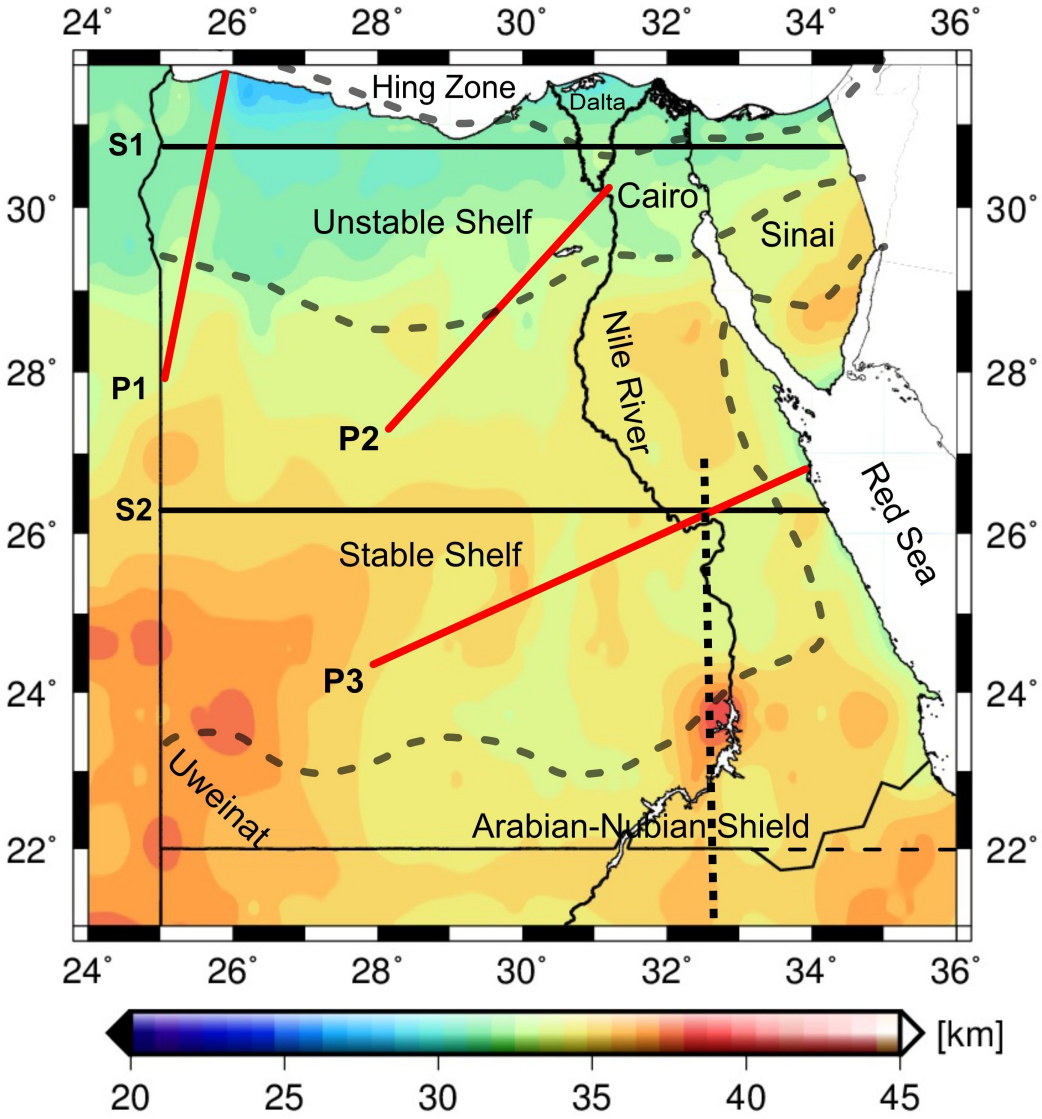

Figure 3.12: The crustal thickness map determined from the 3D gravity modelling with major geological units indicated. Black lines show the geographic location of the representing the modelled cross-sections S1 and S2. Dashed grey lines are the main tectonic boundaries, Black dashed line is the Keraf shear zone between the Neoproterozoic terranes and the Saharan Metacraton (Abdelsalam et al., 1998). The major geographic features are named and geographically positioned. Red solid lines show the location of three profiles taken, where the seismic refraction profiles were carried out.

3.6.3 Comparison of Regional Moho Models

A regional comparison of the gravity-derived Moho depth estimates with respect to the global seismic crustal model CRUST1.0 (Laske, 1997; Laske et al., 2013), shown in Fig. 3.14-a, revealed significant differences. In addition, our findings were cross-compared with two gravity-derived continental-scale models, namely, the GOCE Exploitation for Moho Modelling and Applications, known as the GEMMA model (Reguzzoni, Sampietro, and Sansò, 2013; Reguzzoni and Sampietro, 2015), and the Globig2016 model (Globig et al., 2016a). Table 3.3 summarizes the statistics of the differences.

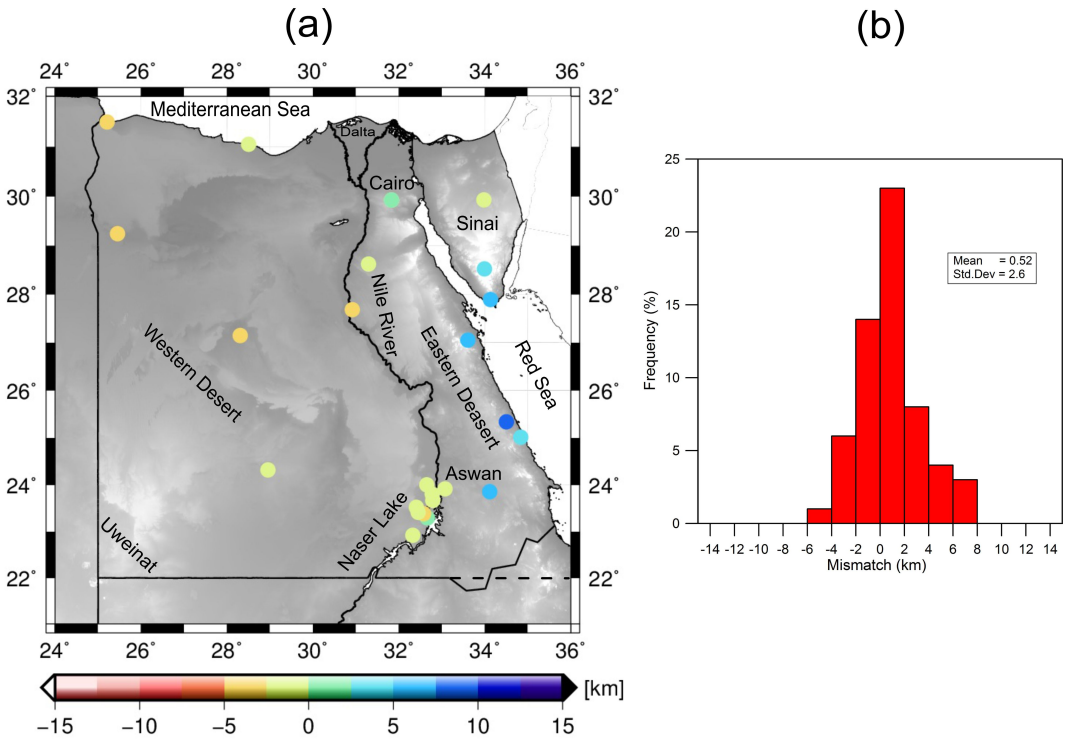

Figure 3.13: (a) The differences between the Moho depths from the receiver functions analysis and gravity-modelled Moho depths. (b) The histogram of the differences with their corresponding mean and standard deviation values; unit [km]. As shown in b, the differences around 0.5 km which indicates the gravity-derived Moho in agreement with the depth derived from receiver functions analysis.

The comparison with the GEMMA model, see Fig. 3.14-b, illustrated that an overall

Table 3.3: Statistical Comparison between Referenced Crustal Models and the new density model.

Model	**Min [km]**	**Max [km]**	**RMSE [km]**
CRUST1.0 − the developed model	−5.76	3.50	2.74
GEMMA − the developed model	−15.97	5.84	4.67
Globig2016 − the developed model	−0.80	11.50	1.42

thicker crust, with differences ranging from −5 to 5 km for most of the study area is obtained. The GEMMA model is a gravimetric-based Moho model computed exploiting both the CRUST1.0 and GOCE data.

The Globig2016 model, displayed in Fig. 3.14-c, revealed the minimum RMSE value of 1.42 km. Although the RMSE varies between 1.7 and 4.7 km for all comparisons, the minimum and maximum crustal variations range from −15.97 to 11.5 km, indicating that in some regions, differences can be pronounced. Generally speaking, our crustal model is much thinner than the Globig2016 model, with differences ranging from 0 to 5 km for most of the study area. A note must be taken that the Globig2016 model is developed based on the joint modelling of the elevation and geoid data, combined with thermal analyses under the assumptions of local isostasy and thermal steady-state conditions.

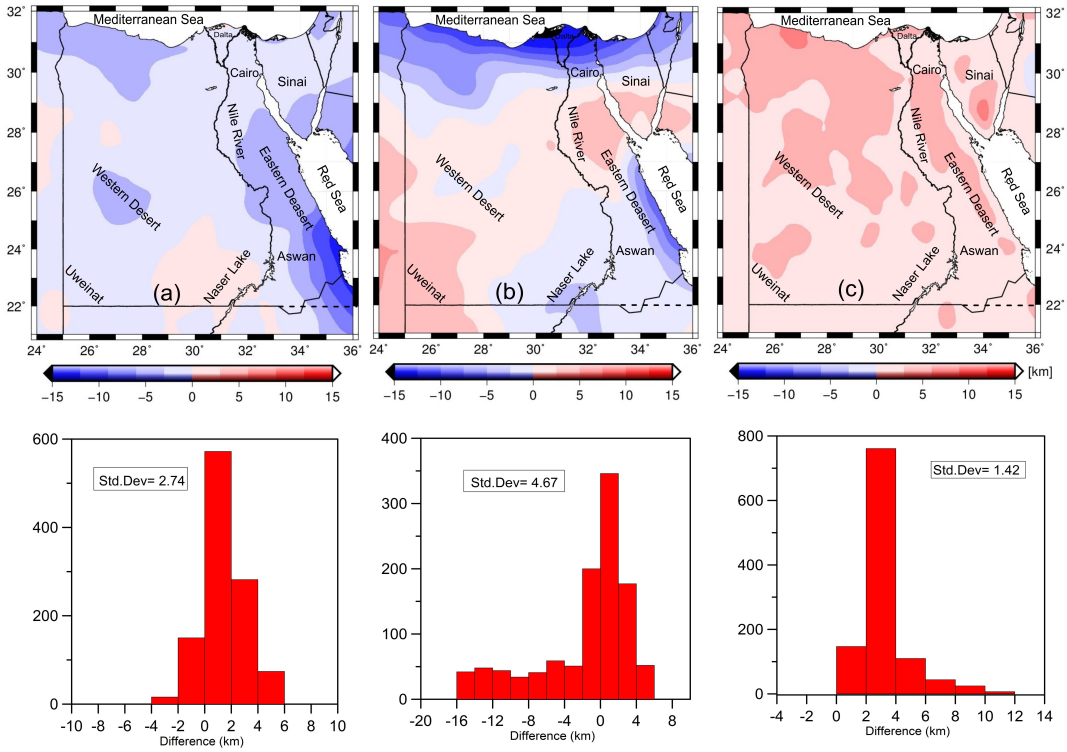

Figure 3.14: Comparison between regional crustal thickness models and our model. (a) The CRUST1.0 model (Laske et al., 2013), (b) the GEMMA model (Reguzzoni, Sampietro, and Sansò, 2013), and (c) the Globig2016 model (Globig et al., 2016a). The (top panel) reports the residuals of the designated model with respect to the crustal thickness calculated in this study; unit [km], and the (bottom panel) is the histograms of the differences between the developed model and the CRUST 1.0; GEMMA; and Globig2016, respectively; unit [km]. The major geographic features are named and geographically positioned.

3.6.4 Errors of Moho Depth Estimations

The accuracy of the estimated gravity-based Moho depths depends on several factors, related to the quality of the input gravity data and the applied corrections, the constraining seismic data, the availability of a precise topographic model, and the sediment thickness. With regard to the used receiver functions data for determination of the Moho interface an average error of about ± 4 km indicated for Egypt (Hosny and Nyblade, 2016).

The Moho depth uncertainties attributed to the errors of the gravity data are relatively small because the accuracy of the input gravity signal and the corresponding applied corrections are of about ± 7 mGal or better. Specifically, the uncertainty of the FA anomaly provided by the Getech is ± 5 mGal (Sobh et al., 2018). The topographic correction has an error of ~ 2 mGal, which is caused by the 6 m mean error, over North Africa, of the SRTM model (Rodriguez, Morris, and Belz, 2006). The topographic corrections computed with a constant density value of 2670 kg·m^3 for all rock masses above the mean Sea level, which will contribute an additional error during the computation of the TC as well as the estimated Moho depths.

3.7 Conclusions

Based on the combination of the Bott's method with regularization, the anomalous Moho has been discretized using the Tesseroids, in order to develop the first order Moho depths map that would be consequently used as an initial layer for the 3D forward gravity modelling by (IGMAS+) over Egypt. Then, the 3D model is fed with precise topographic values. The obtained results are cross-compared with the available seismic data and the Airy-type local isostatic compensation model. A significant correlation between the crustal thicknesses, elevation values, and Bouguer gravity advocates that the crust is isostatically compensated.

The 3D gravity model was constrained using the available deep seismic profiles, depths of receiver functions studies, and geological information in order to produce a regional model of the crustal thickness for the continental part of Egypt. The developed Moho depths model was compared with compilations of the seismic estimates showing a good agreement as well as a high level of consistency.

The modelled Moho depths clearly exposed both the northward and eastward crustal thinning trends toward the Mediterranean Sea and the Red Sea, respectively. Eastward, the Moho under the Eastern Desert is located at a depth of $\sim$ 31 km, which increases in southern Egypt to values ranging from 35 to 40 km. A maximum crustal thickness of 45 km is found in the southwestern part of Egypt. Within Sinai, the crustal thickness varies from being shallow at the southern edge to deep towards the north. Our model revealed a thick lower crust beneath the Southern part of Egypt that can be associated with the modification of the crust that occurred during the collision between east Gondwana and the Sahara metacraton along the Keraf suture zone during the final assembly of Gondwana in the Neoproterozoic.

The study demonstrates the advantage of gravity inversion in studying the 3D density structure of geologically-interesting formations, where the Bouguer anomaly data is combined with a priori information retrieved from the petrophysical (e.g., density values) and seismic datasets. Compared to previous studies, the developed model shows a better match with the available seismic studies than the global crustal model (e.g., the CRUST1.0 and GEMMA), in which interpolation such global models on local scales might give unrealistic Moho depth values.
This study has mainly focused on the continental crust, where successive studies targeting the entire lithospheric scale incorporating seismic tomography and ideally petrological data are highly recommended.

Chapter 4

Manuscript III: Lithospheric structure of the Saharan Metacraton from 3D integrated petrological-geophysical modelling

Abstract

We model the variations of the crustal and lithospheric thicknesses as well as the variation in temperature, composition, S-wave seismic velocity and density of the lithosphere beneath the Saharan Metacraton (SMC) using three-dimensional (3D) modelling. The SMC was once an intact Archean-Paleoproterozoic craton, but was remobilized (metacratonized) during the Neoproterozoic due to partial loss of its sub-continental lithospheric mantle (SCLM) during collisions along its margin. The partial loss of the SCLM might have permitted the preservation of the cratonic remnants within the metacraton. We discuss the possible preserved cratonic remnants within the SMC exploiting integrated modelling using geophysical, petrological, and geological information for the crust and the lithospheric mantle. The cratonic remnants are overlain by Paleozoic-Mesozoic sedimentary basins and they are surrounded and separated by topographic swells with known Cenozoic volcanism including the Hoggar Swell, the Tibesti Massif, and the Darfur Dome. We find that the three cratonic remnants are underlain by a relatively thicker lithosphere (the thickest being beneath Al-Kufra reaching $\sim$ 200 km) compared to the surrounding SMC, which has an average lithospheric thickness of $\sim$ 150 km. We also find that the SCLM of the cratonic remnants to be relatively colder and denser, as seen by faster S-wave velocities compared to the surrounding SMC. Our preferred models are approached considering different lithospheric thicknesses beneath the SMC with a uniform moderately-depleted composition (Proterozoic SCLM composition). We suggest that the presence of a relatively thinner lithosphere beneath the SMC, outside the cratonic remnants, was due to a combination of Precambrian events (partial SCLM delamination during the Neoproterozoic) and Phanerozoic events (Mesozoic-Cenozoic rifting and Cenozoic mantle volcanism).

4.1 Introduction

cratons are parts of the Earth's continental lithosphere that have not been affected by major tectonic or magmatic events for a long time, possibly since the time of their formation (Black and Liégeois, 1993). The stability of the cratons has been largely attributed to the presence of thick, cold, depleted, and anhydrous sub-continental lithospheric mantle (SCLM) that is isolated from the surrounding convecting mantle. However, it has been realized that cratons can lose their long-lasting stability through geodynamic processes leading to their total destruction (referred by Yang et al., 2008 as decratonization) or partial destruction (referred to by (Abdelsalam, Liégeois, and Stern, 2002) as metacratonization). Recently, (Ngalamo et al., 2017) listed examples of cratons that have been decratonized similar to the North China craton (e.g., (Kusky et al., 2014; Santosh, 2010; Zhai and Santosh, 2011; Zhang et al., 2011; Zhao and Zhai, 2013; Zhang et al., 2014)), the Wyoming craton (Föster et al., 2006; Kusky et al., 2014; Dave and Li, 2016), the Southwest Kaapvaal craton (Kobussen et al., 2008; Eriksson et al., 2009)), and the West Amazon craton (Kusky et al., 2014). These are in addition to the Saharan Metacraton (SMC) (Abdelsalam, Liégeois, and Stern, 2002). The term "metacraton" as exemplified by the Saharan Metacraton (Fig. 4.1) is defined as a "craton" that has been remobilized during tectonic and/or thermal events but can still be recognized through its rheological, geochronological and isotopic characteristics (Abdelsalam, Liégeois, and Stern, 2002). Later, (Liégeois et al., 2013) suggested that the metacratonization processes could occur at the craton's boundaries or within the craton's interior during events such as lithospheric plate collision or development of lithospheric-scale shear zones.

(Abdelsalam, Gao, and Liégeois, 2011) used low-resolution seismic tomography from the model of (Grand, 2002) to interpret the upper mantle structures of the Saharan Metacraton. The upper 100 km of the metacraton's SCLM has a S-wave velocity structure similar to the West African craton, the Congo craton, and the Kalahari craton. However, they also observed that the S-wave velocity of the metacraton's SCLM below 100 km depth is much lower than that of the other cratons. (Abdelsalam, Gao, and Liégeois, 2011) proposed that such upper mantle structure was due to partial SCLM delamination or convective removal of the cratonic keel, hence implying that the entire craton has been metacratonized. However, (Liégeois et al., 2013) suggested that the upper mantle structure of the Saharan Metacraton is heterogeneous and that metacratonization might be unevenly distributed leaving some remnants of the original cratonic lithosphere unaltered. These include the Murzuq, the Al-Kufra, and the Chad cratonic remnants (Fig. 4.1).

The understanding how cratons were formed and destructed (decratonized and metacratonized) is fundamentally important for advancing our understanding of the rates of continental growth and destruction because these processes might have led to the alteration of the volume of the continental lithosphere (Stern and Scholl, 2010). The first step to understand the geodynamics evolution, and the thermal state of the Earth's mantle beneath the SMC is constraining the present-day thermal and compositional 3D structure of the lithosphere/uppermost mantle as a fundamental element to understand the metacratons processes.

Geochronological and isotopic data (Abdelsalam, Liégeois, and Stern, 2002) indicate that the crust of the Saharan Metacraton is heterogeneous in age and contrasts the Neoproterozoic juvenile crust (crust derived from the mantle with a short crustal residence time) of the Arabian-Nubian Shield to the East and the Archean

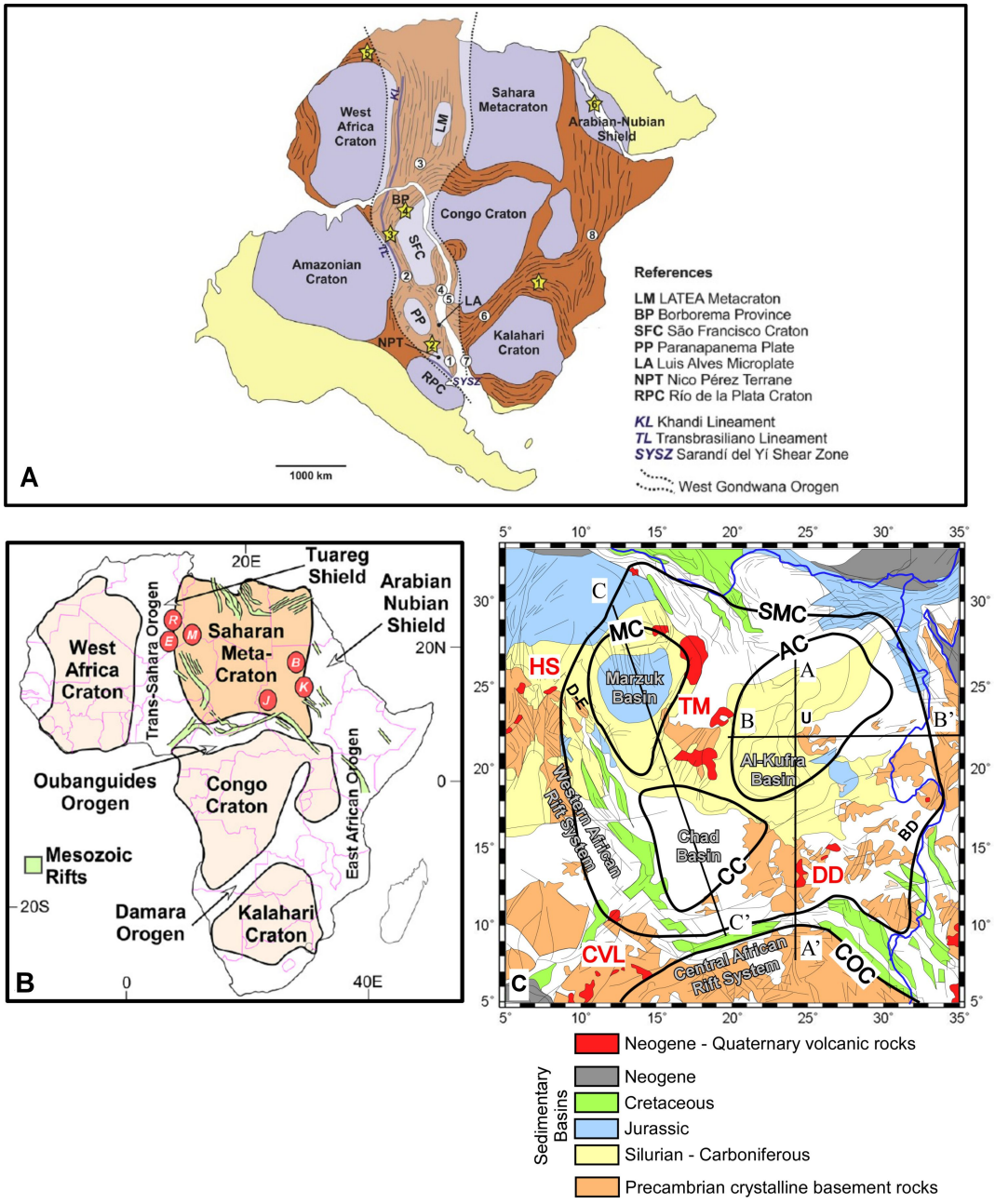

Figure 4.1: (A) Sketch of a Gondwana reconstruction with the major tectonic elements of Africa identied from geological mapping, geochemical, and geochronological studies, and seismic tomography (modified after Liégeois et al. (2013), Brito Neves and Fuck (2014), Ganade et al. (2016), and Gray et al. (2008)). (B) sketch map showing the cratons, metacraton, and orogenic belts of Africa (modified after Meert and Lieberman (2008)). (C) Tectonic map of the Saharan Metacraton modified from the Tectonic Map of Africa. The boundaries of the cratonic remnants are modified from Liégeois et al. (2013). SMC = Saharan Metacraton. MC = Murzuq cratonic remnants. AC = Al-Kufra cratonic remnants. CC = Chad cratonic remnants. HS = Hogar Swell. TM = Tibesti Massif. DD = Darfur Dome. CVL = Cameroon Volcanic Line. D-E = Djanet–Edembo terranes. U = Uweinat. BD = Bayuda. COC = Congo craton.

continental crust of the Congo craton in the South. These data indicate that such

a region constitutes a pre-Neoproterozoic continental crust overprinted by Neoproterozoic tectonic events (e.g., Pan-African collision events), which culminated in the formation of the Late Neoproterozoic supercontinent Gondwana (Kröner and Stern, 2005) as well as containing Neoproterozoic juvenile material. Ages ranging between Archean and Neoproterozoic are obtained from different rock types in the Saharan Metacraton that has been interpreted as an indicator on the presence of an Archean-Paleoproterozoic crust, which was subsequently reworked during the Neoproterozoic.

The mantle structure beneath the SMC region has been studied using regional and global seismic tomographic models. Fig. 4.2 shows the S-wave velocity distribution obtained from the regional seismic tomography model (Fishwick, 2010) at 100 km depth. The model shows lateral heterogeneities in shear wave velocities.

The three-cratonic remnants are associated with high S-wave velocity (Fig. 4.2), and the Darfur Dome, the Tibesti Massif, and the Hoggar Swell are characterized by a low S-wave velocity anomaly that coincides with a shallow Lithospheric-Asthenosphere Boundary (LAB) supporting the idea of the upwelling mantle beneath these Cenozoic volcanic areas. The positive S-wave velocity anomaly are shown in most of the recent tomographic models (global or regional) (Emry et al., 2019; Fishwick and Bastow, 2011; Schaeffer and Lebedev, 2013a; Sebai et al., 2006). Early S-wave seismic tomography models have also identified the positive anomaly beneath Al-Kufra craton to a 100 km depths, but no deeper.

In this study, we present the three-dimensional (3D) lithospheric thermochemical structure of the Saharan Metacraton through an integrated petrological-geophysical modelling exploiting gravity, gravity gradients, topography, geoid, and seismic velocity datasets.

4.2 The Tectonic Settings of the Saharan Metacraton

The tectonic setting of the Saharan Metacraton is introduced in detail in (Abdelsalam, Liégeois, and Stern, 2002). The region is bounded in the East, West, and South by lithospheric-scale suture zones resulting from Neoproterozoic collisional events of the metacraton with the surrounding terranes.

To the East, a N-trending arc-continental suture separates the Saharan Metacraton from the Arabian–Nubian Shield (see, Fig. 4.1-A), which represents the northern part of the East African Orogen (Abdelsalam and Dawoud, 1991; Abdelsalam and Stern, 1996a; Stern et al., 1994). Similarly, a N-trending shear zone in the West is interpreted as a suture defining the collision zone between the metacraton and the Tuareg Shield (consult, Fig. 4.1-A), which represents the northern part of the Trans-Saharan Orogen (Liégeois et al., 1994; Liégeois et al., 2003; Henry et al., 2009). In the South, as shown in Fig. 4.1-A, the Saharan Metacraton is separated from the Congo craton (COC) by the E-trending Oubanguides Orogen, which is interpreted as imbricated Neoproterozoic and Archean–Paleoproterozoic thrust sheets, tectonically emplaced southward onto the Congo craton (Pin and Poidevin, 1987; Toteu et al., 2006).

Significant portions of the Precambrian rocks of the Saharan Metacraton are covered either by Phanerozoic sedimentary rocks or unconsolidated sediment. Most of the Precambrian rocks crop out within outliers surrounded by these sediments.

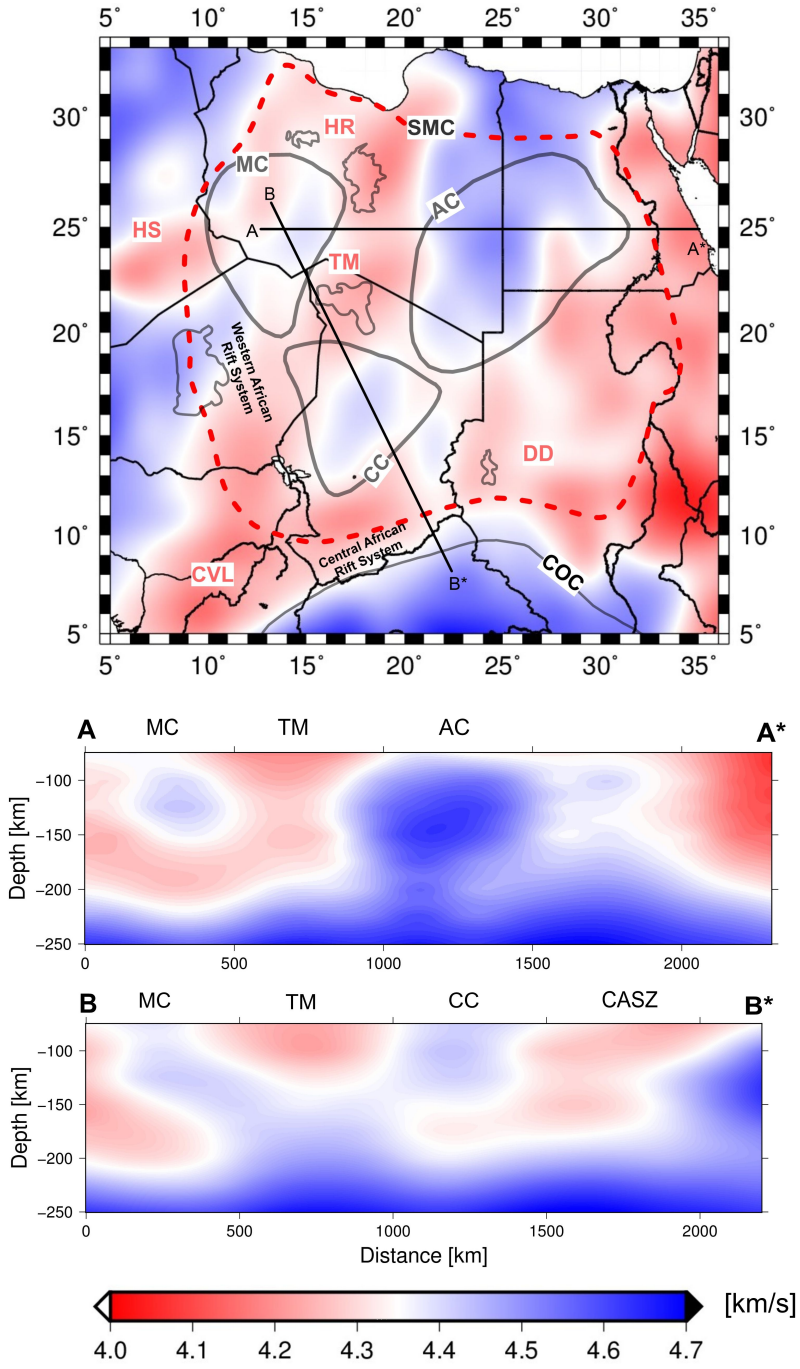

Figure 4.2: Tomographic S-wave model from Fishwick (2010). Slice at a depth of 100 km, two vertical transects are displayed: A-A and B-B profiles. MC = Murzuq cratonic remnants. AC = Al-Kufra cratonic remnants. CC = Chad cratonic remnants. TM = Tibesti Massif. CASZ= Central African Shear Zone. Both cross-sections show high-velocities along the Murzuq, Chad, and Al-Kufra cratonic remnants and low-velocities along the Tibesti Massif and Central African Shear Zone

These outliers include the Tibesti Massif (TM), the Uweinat (U), the Bayuda (BD), and the Darfur Dome (DD) besides small scattered outcrops (Fig. 4.1-C).

Within the Saharan Metacraton, there are three broad sedimentary basins of Paleozoic-Mesozoic age, namely, the Chad, the Murzuq, and the Al-Kufra. At least one of these

basins (Al-Kufra) has been identified as an intracontinental sag basin (Heine et al., 2008) and its evolution has been attributed to the lithospheric cooling and thickening of an initially thin lithosphere (Holt et al., 2010). Also, the Saharan Metacraton is surrounded by Mesozoic continental rifts related to the breakup of the Gondwana and those rifts are grouped as the west and the Central African Rift Systems (see, Fig. 4.1-C) Fairhead, 1979; Fairhead et al., 1988. In addition, widespread Cenozoic volcanism has affected the Saharan Metacraton that is interpreted to be associated with the continental rifting (Thorpe and Smith, 1974), Neoproterozoic Pan-African crustal reworking (Ashwal and Burke, 1989), or hotspots beneath the Hoggar (HS), the Tibesti (TM), the Darfur (DD), and the Cameroon Volcanic Line (CVL) (Fig. 4.1-C). The volcanic fields of the Hoggar, the Tibesti, and the Darfur are associated with topographic swells of uplifted Precambrian crystalline basement (see, Fig. 4.1-B). The source of the Cenozoic volcanism might be fed by the Afar plume (Ebinger and Sleep, 1998), unconnected plumes (Wilson and Guiraud, 1992; Burke, 1996), or by upwelling of the asthenosphere associated with the Africa-Europe collision (Bailey, 1992).

4.3 Methods

4.3.1 Moho Depth from Gravity Inversion

To develop the Moho depth of the Saharan Metacraton, we follow the methodology of (Uieda and Barbosa, 2017), who developed a non-linear inversion algorithm that integrates both gravity and seismic data. This inversion technique is based on the modified Bott's method (Silva, Santos, and Gomes, 2014b) with a Tikhonov regularization to stabilize the computed solutions in a two-steps procedure. In the first step, the regularization parameters are determined using a predefined set of initial values for the mean depth and the density contrast of the Moho discontinuity. In the second step, the gravimetric inversion is carried out for a set of various values of the mean Moho depth and density contrast, where the best estimate, i.e. the final solution, is obtained after the cross-comparison with the seismic-based Moho depth estimates is held. The results of the gravity inversion are controlled by two parameters namely, the Moho reference depth and the density contrast between the crust and the upper mantle.

Since the mean depth of the Moho boundary and its density contrast are poorly known for the Saharan Metacraton, we would examined all the possible combinations of the nine Moho reference depth values that range from 20 to 40 km with a 2.5 km incremental step, and the seven density contrast values that range between 200 and 500 km·m^{-3} with 50 km·m^{-3} intervals. Afterwards, the Moho depth results are validated against the Moho depth from seismological estimates. Finally, the model that gives the lowest Mean Square Error (MSE) values will be chosen as the best fitting model. For more details on the gravity inversion methodology, the reader is referred to (Uieda and Barbosa, 2017)

4.3.2 Integrated Modelling by LitMod3D and Model Assumptions

Here we provide a brief review of the modelling technique; LitMod3D (LIThospheric MODelling in a 3D geometry) is thoroughly introduced and explained in (Afonso et

al., 2008; Fullea et al., 2009). The general scheme of the modelling work-flow is shown in Fig. 4.3.

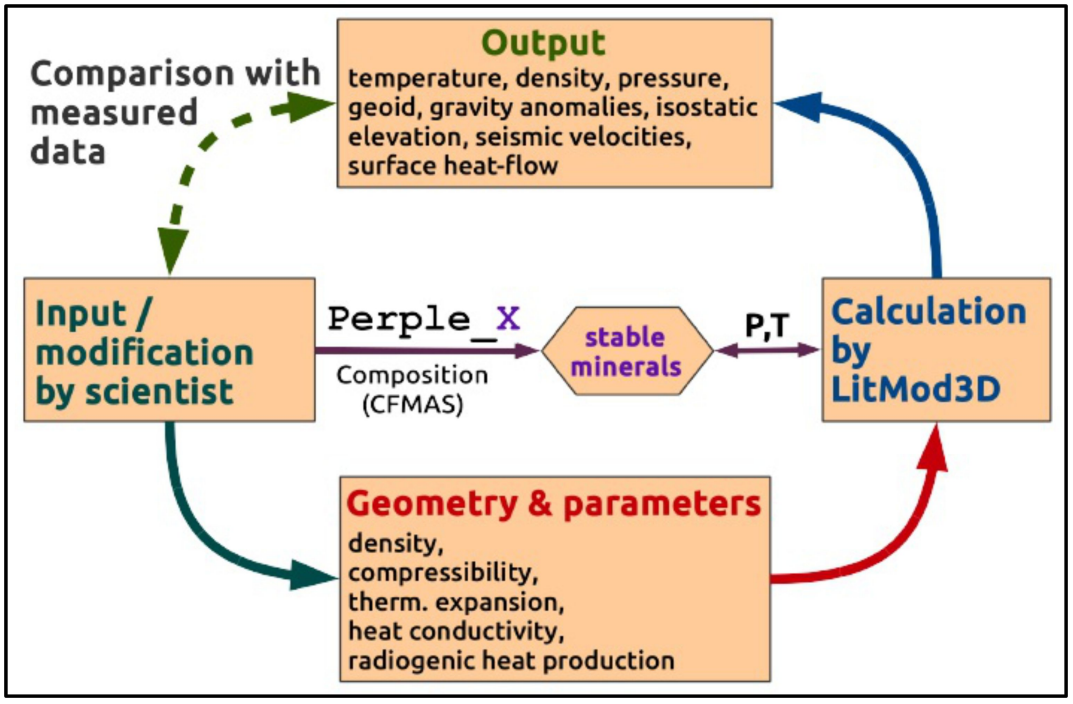

Figure 4.3: A simplified flowchart of the LitMod3D after Pappa et al. (2018) (pers. comm.)

LitMod3D was developed to perform integrated geophysical-petrological forward modelling of the lithosphere and the sublithospheric mantle down to the top of the transition zone at 410 km depth. The LAB definition is based on both, the temperature and compositional distributions. Therefore, we assume that the lithospheric mantle is defined:

- thermally, as the portion of the mantle characterized by a conductive geotherm;
- compositionally, as the portion of the mantle characterized by, generally, a different (normally, more depleted) composition with respect to the fertile primary composition in the sub lithosphere, i.e., Primitive upper mantle composition (PUM) (McDonough and Sun, 1995).

The lithospheric geotherm is computed under the assumption of a steady-state heat transfer condition in the lithospheric mantle, considering a P-T-dependent mantle thermal conductivity (Afonso et al., 2008; Fullea et al., 2009). As boundary conditions, we impose no lateral heat flow across the vertical limits of the model and fixed temperature at the surface (15° C) and at the base of the defined lithosphere (1330° C).

The heat production and thermal conductivity of each layer are defined. Between the lithosphere and sub-lithospheric mantle, a "transition" region (a buffer layer) is assumed with a variable thickness and a continuous linear super-adiabatic gradient (i.e., heat transfer is controlled by both conduction and convection, see (Fullea et al., 2009) for more details). Below the buffer layer, the geotherm is given by an adiabatic temperature gradient that is forced to be in the range 0.35 to 0.6° C/km.

Stable mineral assemblages in the mantle are calculated using a Gibbs free energy minimization using Perple_X as described by (Connolly, 2005). The composition is defined within the major oxide system CFMAS (CaO-FeO-MgO-Al_2O_3-SiO_2). In our study, all the stable assemblages are based on the (Stixrude and Lithgow-Bertelloni, 2005; Lithgow-Bertelloni and Stixrude, 2011) thermodynamic database. The LitMod3D approach allows for a self-consistent calculation of phase equilibria (identity and amount of mineral phases stable at a certain pressure and temperature) and physical properties. The density and seismic velocities in the upper mantle are determined according to the elastic moduli and density of each end-member mineral as described by (Connolly and Kerrick, 2002; Afonso et al., 2008).

4.4 Data

The data used to constrain the lithospheric model of the SMC can be divided into three groups.

1. Geophysical observables and fields (elevation, geoid height, gravity, gravity gradients, and surface heat flow) 4.1. For initiating the model we need information (data) related to the geometry of the start model;

2. Crustal thickness information; Lithospheric thickness and geometry. For the petrological part, we use

3. Petrological information on the SCLM compositions as a model input.

Table 4.1: Summary of the exploited datasets used to constrain the initial model.

Data	Reference
Geophysical	
Elevation	ETOPO1 (Amante, 2009)
Calculated Bouguer gravity	GOCO5S (Mayer-Güerr, 2015)
Geoid	GOCO5S (Mayer-Güerr, 2015)
Gravity gradients	Bouman et al. (2015)
Surface heat flow	Pollack, Hurter, and Johnson (1993)
Seismic tomography	Fishwick (2010)
Geometrical	
Sediment thickness	Exxon Tectonic Map of the World data Exxon, 1985
Moho depth	Compilation (Tokam et al., 2010; Hansen et al., 2013) (Hosny and Nyblade, 2016; Tahir et al., 2013), gravity inversion (Uieda and Barbosa, 2017)
Base lithosphere	Fishwick and Bastow (2011)

4.4.1 Geophysical Fields Observables

We used the 1 arc-min spatial resolution ETOPO1 global elevation model shown in Fig. 4.4-A Amante, 2009. The Saharan Metacraton has a relatively low-lying topography, that is interrupted by a number of shorter wavelength swells and uplifted regions, such as the Darfur Dome (reaching an elevation of $\sim$ 1200 m), the Hoggar

Swell (reaching an elevation of $\sim$ 1000 m), and the Tibesti Massif (reaching an elevation of $\sim$ 2000 m). In places, there is relief lower than $\sim$ 500 m and this has been interpreted as due to large-scale crustal flexure associated with the development of sedimentary basins such as the Chad Basin (Fig. 4.4-A).

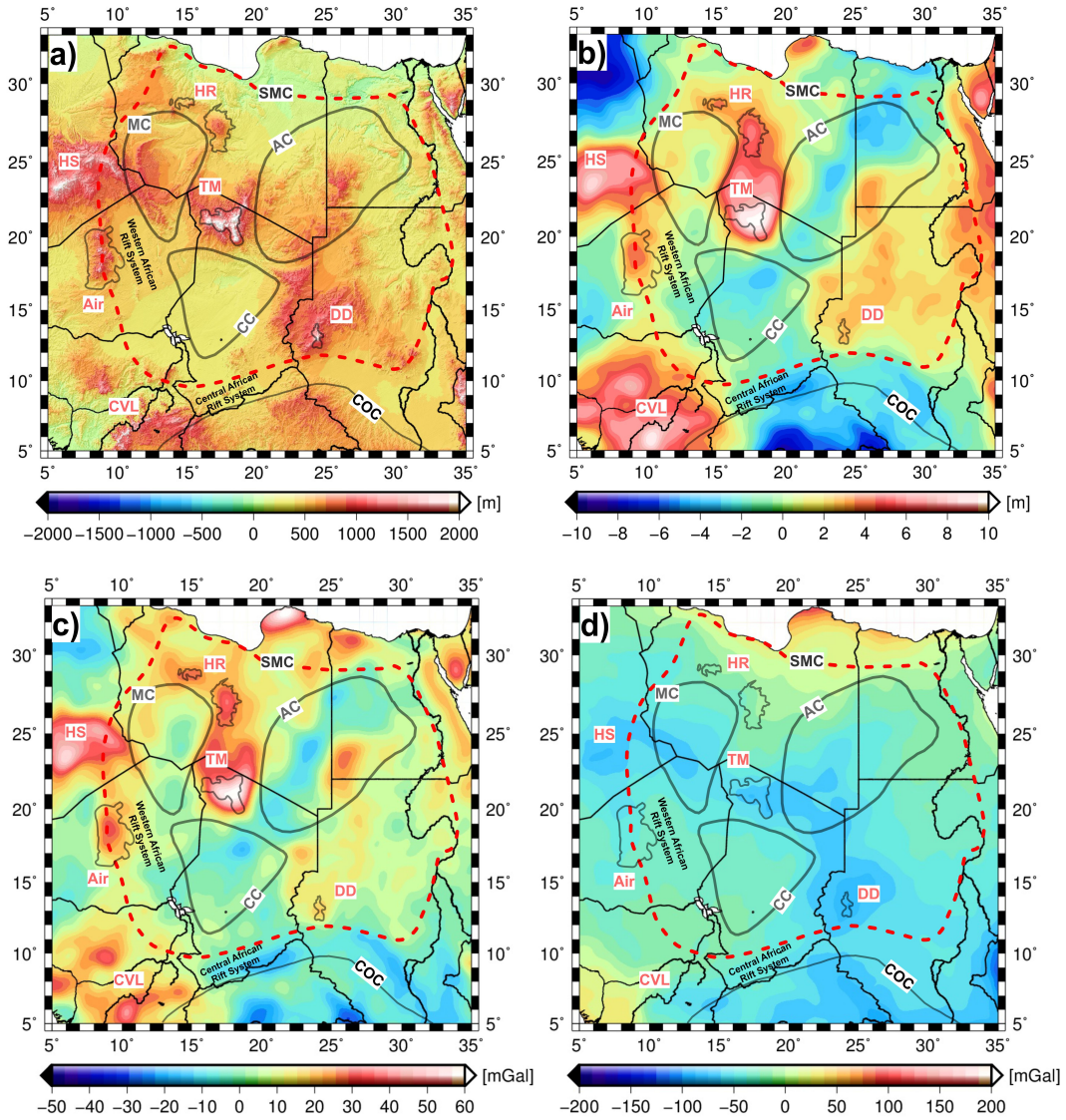

Figure 4.4: Geophysical fields in the Saharan Metacraton. (a) Topography of the Saharan Metacraton generated from the Global 1 arc-minute elevation data ETOPO1 Amante, 2009. The presence of the elevated Darfur Dome (DD), the Tibesti Massif (TM) and the Hogar Swell (HS) aligned in a NW-SE direction. The three cratonic remnants (Al Kufrah, Murzuq, and Chad) are located within the topographic low regions between and around the elevated swells. (b) Geoid height of the Saharan Metacraton calculated from the GOCO5S model Mayer-Güerr, 2015. The three cratonic remnants (Al Kufrah, Murzuq, and Chad) are characterized by low geoid whereas the three swells (Darfur, Tibesti, and Hogar) are characterized by high geoid. (c) Free air anomaly from the GOCO5S model. (d) Bouguer anomaly map from GOCO5S

The geoid height was derived from the fifth release of Gravity Observation Combination model (GOCO5S) (Mayer-Güerr, 2015). The GOCO5S model was developed up to a spherical harmonic d/o 280 exploiting the full GOCE (Gravity field

and steady-state Ocean Circulation Explorer) mission data with a spatial resolution of about 80 km. In order to remove the long wavelength anomalies larger than 4000 km, the spherical harmonics up to a d/o 10 has been subtracted. The obtained geoid anomaly, which reflects the distribution of density and the geometry of masses within the lithosphere (Bowin, 2000) is shown in Fig. 4.4-B. Despite the low amplitude, the geoid anomalies are highly correlated with the topography. Geoid heights ($1 - 10$ m) directly coincide with the Darfur Dome (DD), the Tibesti Massive (TM), and the Hoggar Swell (HS), while the geoid low heights (-10 to -1 m) are associated with the topographic low values associated with the Murzuq basin overlying the Murzuq cratonic remnant, the Al-Kufra Basin overlying the Al-Kufra cratonic remnant, and the Chad Basin overlying the Chad cratonic remnant.

The Bouguer anomaly (Fig. 4.4-D) was computed by applying the Bouguer correction to the satellite free-air gravity (Fig. 4.4-C) derived from the GOCO5S model at 50 km height over ellipsoid using tesseroids software (Uieda, Barbosa, and Braitenberg, 2016) with a correction density of 2670 $kg{\cdot}m^{-3}$ for onshore and 1040 $kg{\cdot}m^{-3}$ for the offshore.

The entire Saharan Metacraton is characterized by the so-called "great negative Bouguer anomaly" lineament (Girdler, 1975) linking the domally uplifted Cenozoic volcanism of North Africa to the negative Bouguer anomaly associated with the East African Rift System (Fairhead, 1979; Fairhead et al., 1988).

This suggests that the North African gravity anomaly might be caused by the same processes that have caused the East African Rift System anomaly as a result of the low-density upper mantle structure. Bouguer anomaly values of -95 mGal ($1\ \text{mGal} = 1 \times 10^{-5}\ m{\cdot}s^{-2}$) are observed beneath the Darfur Dome, whereas the Tibesti Massif and the Hoggar Swell show values that range between -85 and -80 mGal. The Murzuq, the Al-Kufra, and the Chad basins are characterized by Bouguer anomaly values of ~ -70, ~ -45, and ~ -20 mGal, respectively.

Gravity gradients (Fig. 4.5) are retrieved from the GOCE satellite gravity gradient grids (Bouman et al., 2016). The satellite gravity data are collected at 225 km above the WGS84 reference ellipsoid, in a local East-North-Up coordinate system.

We use the gravity gradients data at satellite altitude in additions to the gravity data, as they are highly sensitive, especially, to the density structure of the crust and uppermost mantle (Bouman et al., 2016; Holzrichter, Szwillus, and Ebbing, 2016; Guy, Holzrichter, and Ebbing, 2017).

The compilation of surface heat flow data used in this work comes from different sources (Pollack, Hurter, and Johnson, 1993; Lesquer et al., 1990; Nyblade et al., 1996). In general, details on the quality of data are not available. According to the International Heat Flow Commission, the good, average, and poor accuracy levels are, respectively, of ± 5, ± 10, and $\pm 20\%$. A few but sparse heat flow values in the Western Desert, West of the Nile, range between 42 and 47 $mW{\cdot}m^{-2}$, increasing toward the coastal zone of the Red Sea and the Gulf Suze in both shores where values of 80 to 100 $mW{\cdot}m^{-2}$ are measured. In Aswan area, low heat flow shows values of $45 - 57\ mW{\cdot}m^{-2}$ were acquired. On the other side, the heat flow across the Sirt Basin has shown to be normal ($49 - 77\ mW{\cdot}m^{-2}$) at the Eastern part that slightly elevated

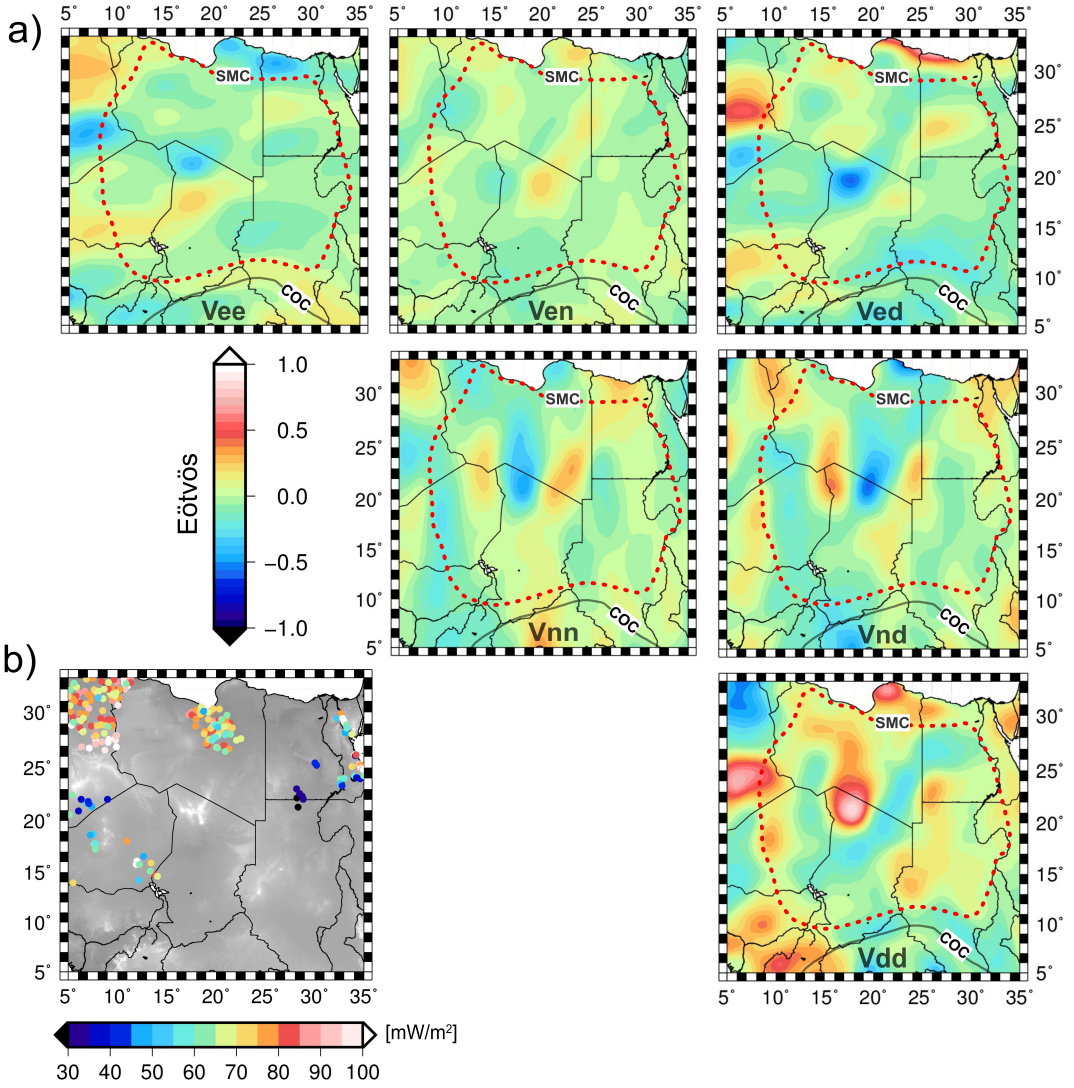

Figure 4.5: (a) Satellite gravity gradient components Bouman et al., 2016 at the height of 225 km above the reference ellipsoid. (b) The heat flow measurements from global dataset (Pollack, Hurter, and Johnson, 1993).

to $77 - 91$ mW·m^{-2} values in the western part of Sirt Basin, close to the volcanic provinces in Libya (Nyblade et al., 1996). The few available data in Niger indicates heat flow values that range between $45 - 90$ mW·m^{-2}.

4.4.2 Constraints for Model Geometry

Our study is focused on the regional scale thermo-chemical structure of the uppermost mantle beneath the SMC. Therefore, a reliable Moho depth map needs to be defined and kept fixed throughout the modelling process.

However, due to the lack of seismic studies in most parts of North Africa, where the SMC is located, several crustal models were developed exploiting the continental and regional-scale data. These models were either a gravity-based or a combination

of gravity and seismic models. Significant differences in the available models result from the different spatial resolution of the data and/or the modelling technique ((Laske et al., 2013; Reguzzoni, Sampietro, and Sansò, 2013; Tugume et al., 2013; Globig et al., 2016b).

Moho Depth

The main objective of this section is to estimate the Moho depths for the SMC by integrating both the seismic and gravity data. The data inversion is constrained by the new compilation of seismic Moho depths from receiver function studies (Hansen et al., 2013; Tokam et al., 2010; Tahir et al., 2013; Cooper and Miller, 2014; Hosny and Nyblade, 2016) (Fig. 4.6-A).

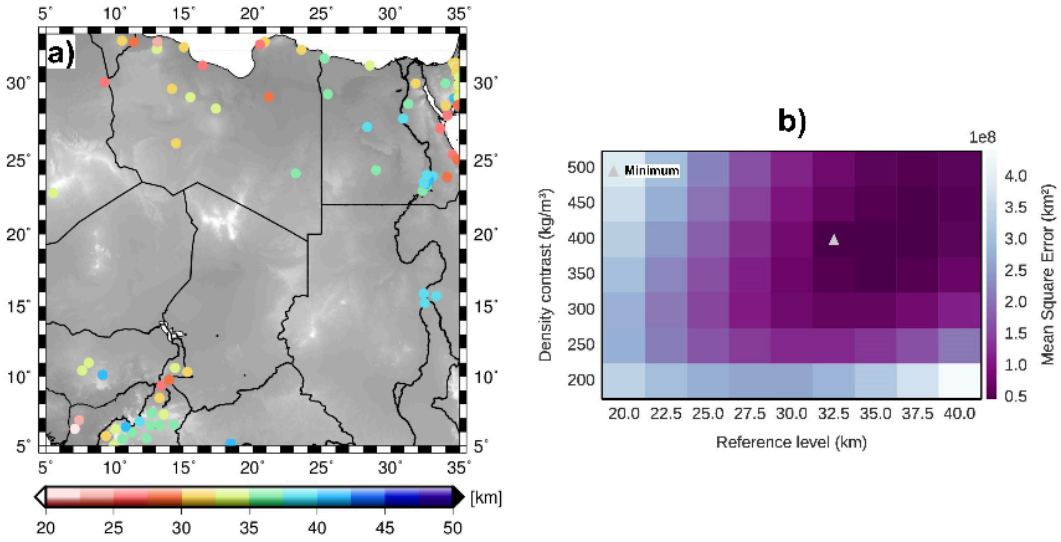

Figure 4.6: (a) Seismic-based estimates of crustal thickness from receiver function studies. (b) The validation step exploited to determine the Moho reference level (Z_{ref}) and the density contrast ($\Delta\rho$). The colors represent the Mean Square Error. The best-fit model is marked by the grey triangle, which indicates a density contrast of 400 kg·m^{-3} and a Moho reference depth of 32.5 km.

In order to get preliminary information about the crustal thicknesses of the SMC, a regularized non-linear gravity inversion was applied (Uieda and Barbosa, 2017) and has been discussed in (Sobh et al., 2018). The combined gravity model GOCO05s at 50 km above the ellipsoid (Fig. 4.4) was used. The representation of the field at 50 km is chosen as it offers a higher level of details in the signal than at satellite altitude and keeps the noise amplification at an acceptable level (Sebera et al., 2014).

The topographic corrections for the GOCE-based data was computed using the Tesseroids Uieda, Barbosa, and Braitenberg, 2016 using the 1 arc-min spatial resolution ETOPO1 model (Amante, 2009) (Fig. 4.4). Fig. 4.6-B visualizes the Mean Square Error (MSE) values with respect to the seismological Moho. The optimal MSE value has been obtained using the 32.5 km reference Moho depth and the 400 kg·m^{-3} density contrast. The obtained Moho depths model varies between 20 and 40 km as shown in Fig. 4.7-B.

Lithospheric Thickness

The LAB of the Saharan Metacraton was taken from the regional seismic model of Africa (Fishwick and Bastow, 2011) (Fig. 4.7). The differences in depth estimates between the different LAB models are significant and sometimes can be as high as 80 km in areas with sparse seismic coverage. For the initial lithospheric modelling, the available information of the LAB depths have been used in this study as a first input, and then further modifications, within the uncertainties range until the best fit is obtained, has been performed.

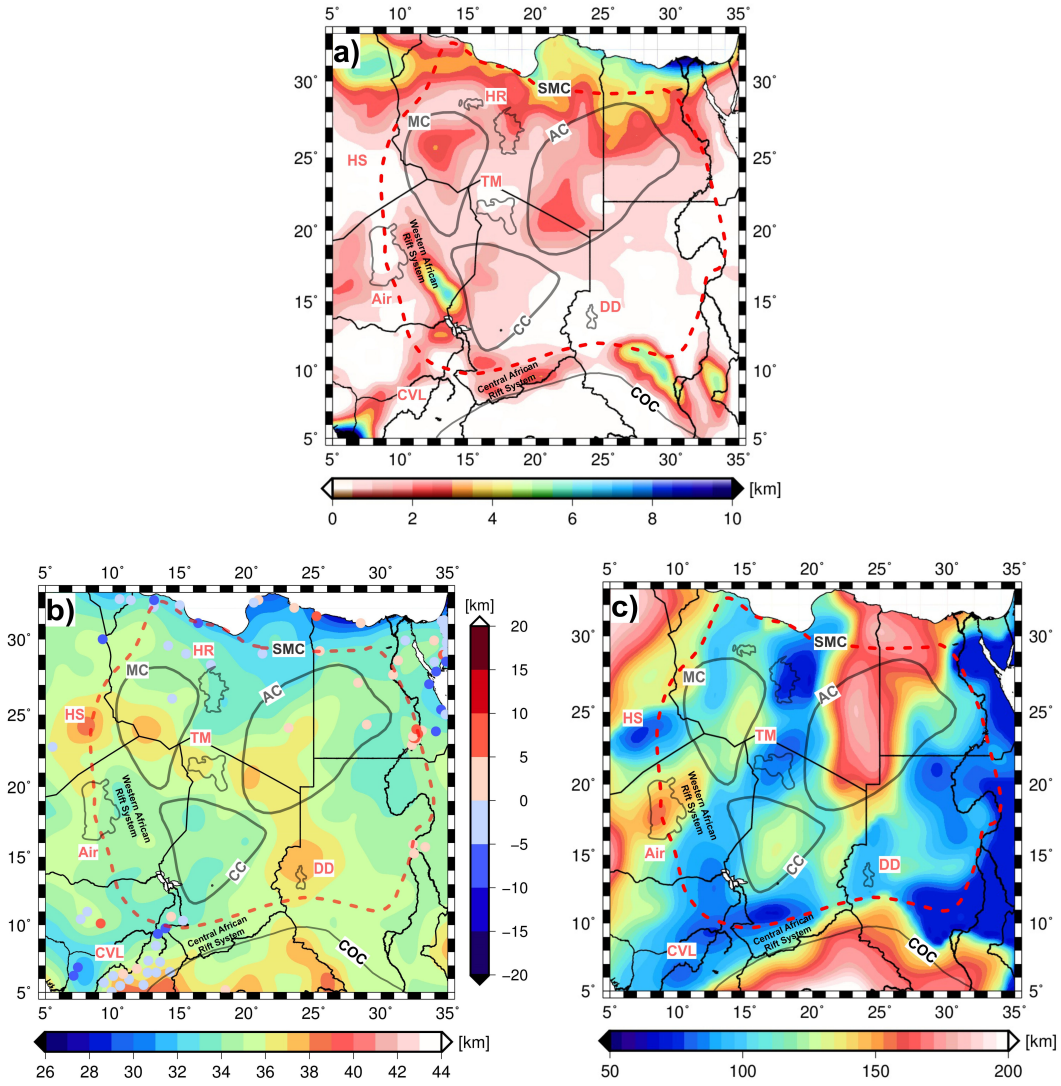

Figure 4.7: Initial geometry used in lithospheric models. (a) Sedimentary thickness from global compilations of Exxon Tectonic Map of the World data (Exxon, 1985). (b) Moho depth from the gravity-inversion constrained by seismic data compilation, The coloured circles indicate the differences in depth between the seismic constraint and the inverted depth. (c) Lithosphere-Asthenosphere Boundary (LAB) from (Fishwick and Bastow, 2011).

Sediment Thickness

The sediment layer was retrieved from the global sediment thickness compilation of the Exxon Tectonic Map of the World (Exxon, 1985) (Fig. 4.7). In the Saharan Metacraton, the thickness of sediments ranges from 0 to 7 km. The cratonic basins (AC, MC, CC) are characterized by $\sim$ 3 km thickness, while most of the part of SMC has sediment thicknesses less than 1 km.

4.4.3 Sub-Continental Lithospheric Mantle (SCLM) Composition

The SCLM composition mainly depends on the tectono-thermal age of the overlying crust (Griffin et al., 2003; Griffin et al., 2008; O'Reilly and Griffin, 2006). Generally, the SCLM is highly heterogeneous in composition ranging from dunites and harzburgites to lherzolites. Such heterogeneities lead to significant density differences at a given P-T condition. The age of the Saharan Metacraton SCLM ranges from Archean to Neoproterozoic. The oldest rocks in the Saharan Metacraton were found in the Uweinat, at the Egyptian-Sudanese-Libyan borders and these rocks gave Archean age (Bea et al., 2011; Klerkx and Deutsch, 1977; Harris, Hawkesworth, and Ries, 1984; André, Klerkx, and Busrewil, 1991).

However, multiple tectonic events affected and likely heated and refertilized the lithospheric mantle during the Pan-African orogeny (Kröner and Stern, 2005). We, therefore, choose a Proterozoic-type (SCLM) composition for our starting model (Table 4.2).

We have tested various lithospheric mantle compositions (Archean and Phanerozoic compositions) in order to evaluate the effects of these changes on the modelled geophysical observables (See Appendix A for more details). No significant mantle xenolith compositional data are available for the Saharan Metacraton. Therefore, we used in our 3D modelling the standard CFMAS compositions from (Griffin et al., 2008) for the SCLM of the Saharan Metacraton. These compositions range from less depleted Proton composition to the more fertile asthenosphere as a Primitive Upper Mantle, PUM (McDonough and Sun, 1995). Table 2. summarizes the SCLM compositions considered in this study.

Table 4.2: Bulk SCLM compositions used in the model. (1) stands for SCLM compositions of (Fullea et al., 2009), Modified from (Afonso et al., 2008), and (Griffin et al., 2008). (2) stands for the PUM of (McDonough and Sun, 1995). (3) Mg# stands for magnesium number: $\frac{MgO}{(MgO+FeO)}$.

	Proterozoic$^{(1)}$	Archean$^{(1)}$	Phanerozoic$^{(1)}$	PUM$^{(2)}$
SiO_2	45.60	45.70	44.5	45.00
Al_2O_3	1.93	0.99	3.5	4.45
FeO	8.00	6.40	8.00	8.05
MgO	42.60	45.50	39.80	37.80
CaO	1.70	0.59	3.10	3.55
Na_2O	0.12	0.07	0.24	0.36
Mg#$^{(3)}$	90.58	92.70	89.87	89.30

4.5 Modelling

4.5.1 Model Setup

Our model covers an area of $\sim$ 3000 $\times$ 3000 km, approximately, and the depth of the bottom of the model is 410 km. Given the lack of knowledge about the characteristics of the lithosphere in wide parts of SMC, it is reasonable to apply general (global) values for the crustal parameters and geochemical oxide compositions for the lithospheric mantle. The model consists of one sedimentary layer, a two-layered continental crust, the lithospheric and asthenospheric mantle (see, Fig. 4.8)).

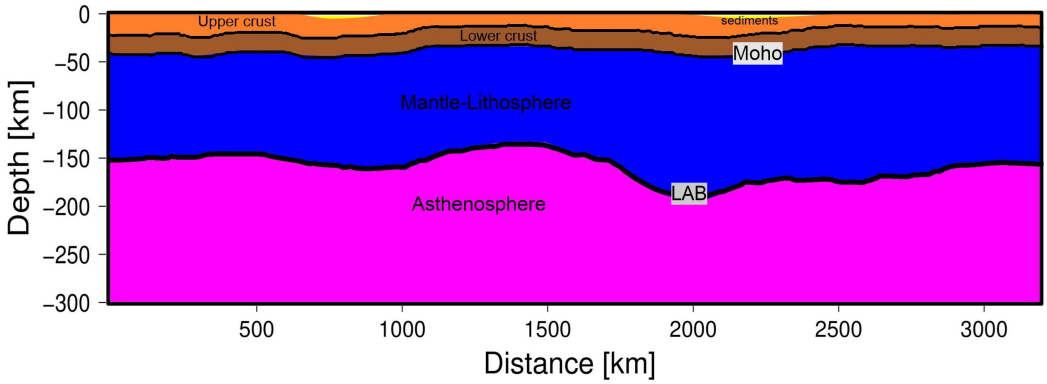

Figure 4.8: Profile illustrating the initial model clearly shows the geometric structure, see Table 4.3 for the thermo-physical properties for each domain.

The continental crust is divided into an upper and lower crust to realistically model the thermal field by introducing differentiated radiogenic heat production rates and thermal conductivity (Table 4.3).

Table 4.3: Thermophysical properties of materials used in the 3D modelling.

Material	**Density** (ρ) [kg·m^{-3}]	**Thermal conductivity** (κ) [W·(km)$^{-1}$]	**Heat production rate** (H) [mW·m^{-2}]
Sediments	2450	2.5	2.000
Upper crust	2670 – 2790	2.4	1.500
Lower crust	2800 – 2850	2.0	0.400
Proton		4.5	0.001

4.6 Results

4.6.1 Modelling Results

The thermo-physical parameters of different crustal bodies are given in Table 4.5. Using the initial parameters as well as the model geometries described in Sec. 4.3, the forward signal does not fit the observables (in particular, the gravity field) and is far from the isostatic compensation in most regions (Fig. 4.9). It also shows high residuals in the gravity gradients (see, Fig. 4.10). Positive elevation residuals extending North-South, in correlation with the LAB depths used in the initial model (M_0),

are clearly seen. That means that the initial Moho and LAB depths are not able to represent the deep lithospheric structure correctly.

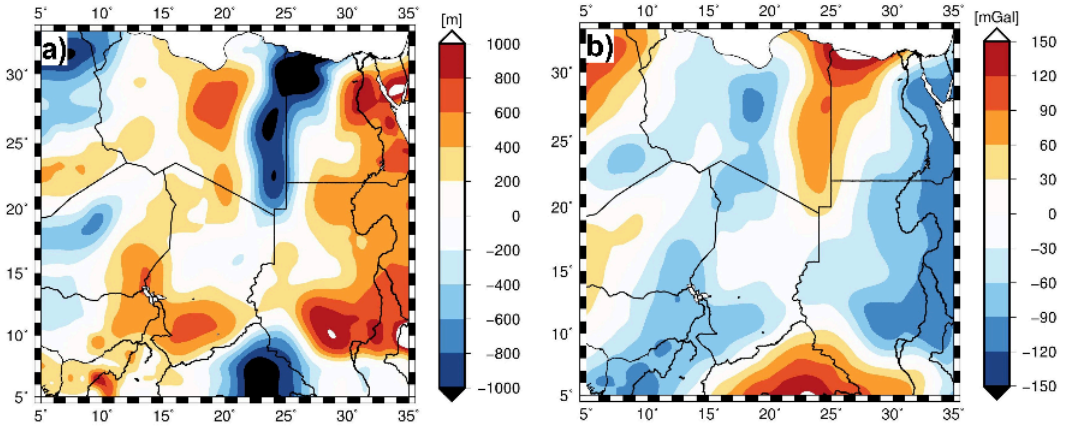

Figure 4.9: Residual field for the initial model (M_0) in terms of: a) Elevation and b) Bouguer anomaly.

Starting from M_0, we iteratively modified the lithospheric geometry (the Moho boundary and LAB depth) according to the topographic misfit (residual elevation) to match the long wavelength gravity field and isostatic elevation based on the trial and error forward modelling.

To fit the gravity gradients data, the original assumption of the isostatic balance of the study area has been ignored. To do that for the final model (M_1), both the Moho boundary and LAB are tuned. Consequently, in the adjusted model, on the one hand, the main objective was fulfilled, as the gravity gradients signal is modelled resulting in very small residuals (Fig. 4.11). While, on the other hand, the obtained elevation residuals are not minimal (Fig. 4.12). The one can justify the motives to better fit the gravity gradients by stating that they are highly sensitive, especially, to the density structure of the crust and uppermost mantle.

4.6.2 Crustal and Lithospheric Thickness

The modelled crustal and lithospheric thickness are displayed in Fig. 4.13. In particular, the resulting crustal thickness map (Fig. 4.13-A) shows a thin crust ($\sim$ 28 km) along the coastal area and Chad basin. Along the Al-Kufra basin, the crustal thickness reaches $\sim 38 - 40$ km, increasing to 41 km beneath Murzuq craton and Darfur Dome. Our results are consistent with the (Globig et al., 2016b) crustal model with some differences.

Also, our estimated Moho depths are in good agreement with those obtained from seismic investigations, regardless of the available seismic data, which are sparsely distributed (see, Fig. 4.7). The shallowest LAB is found beneath the Darfur Dome,

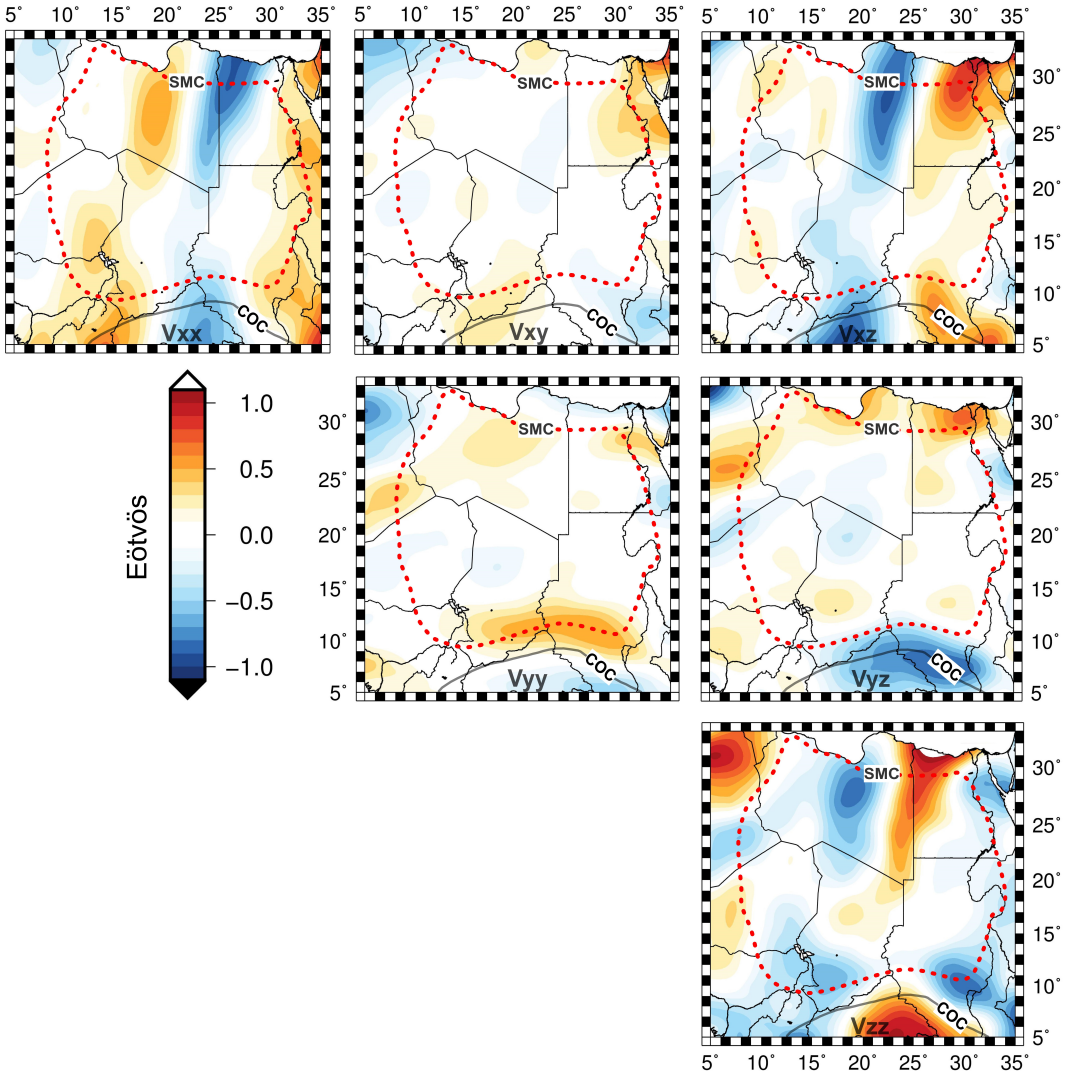

Figure 4.10: Satellite gravity gradients residuals for the initial model (M_0).

the Hoggar Swell, and the Tibesti Massif (Fig. 4.15-B). In contrast, the thickest lithosphere has been allocated beneath the Al-Kufra Basin that overly the Al-Kufra cratonic remnant.

In this region, the lithosphere reaches a thickness of $190 - 200$ km and coincides with high S-wave velocity anomalies (Fig. 4.15). To the west, the LAB thickness of $130 - 140$ km is much less pronounced beneath the Chad and the Murzuq basins that overlie the Murzuq cratonic remnant and the Chad cratonic remnant, respectively. These regions are characterized by a relatively faster S-wave velocity (Fishwick and Bastow, 2011).

After modifying the LAB to fit the gravity fields, it deviated from the original LAB by (Fishwick and Bastow, 2011) with up to ± 50 km differences in the area (Fig. 4.14-B). In order to adjust the small wavelength anomalies of the gravity field and elevation, the depth of the Moho was changed by less than its range of uncertainty by ± 4 km (Fig. 4.14-A).

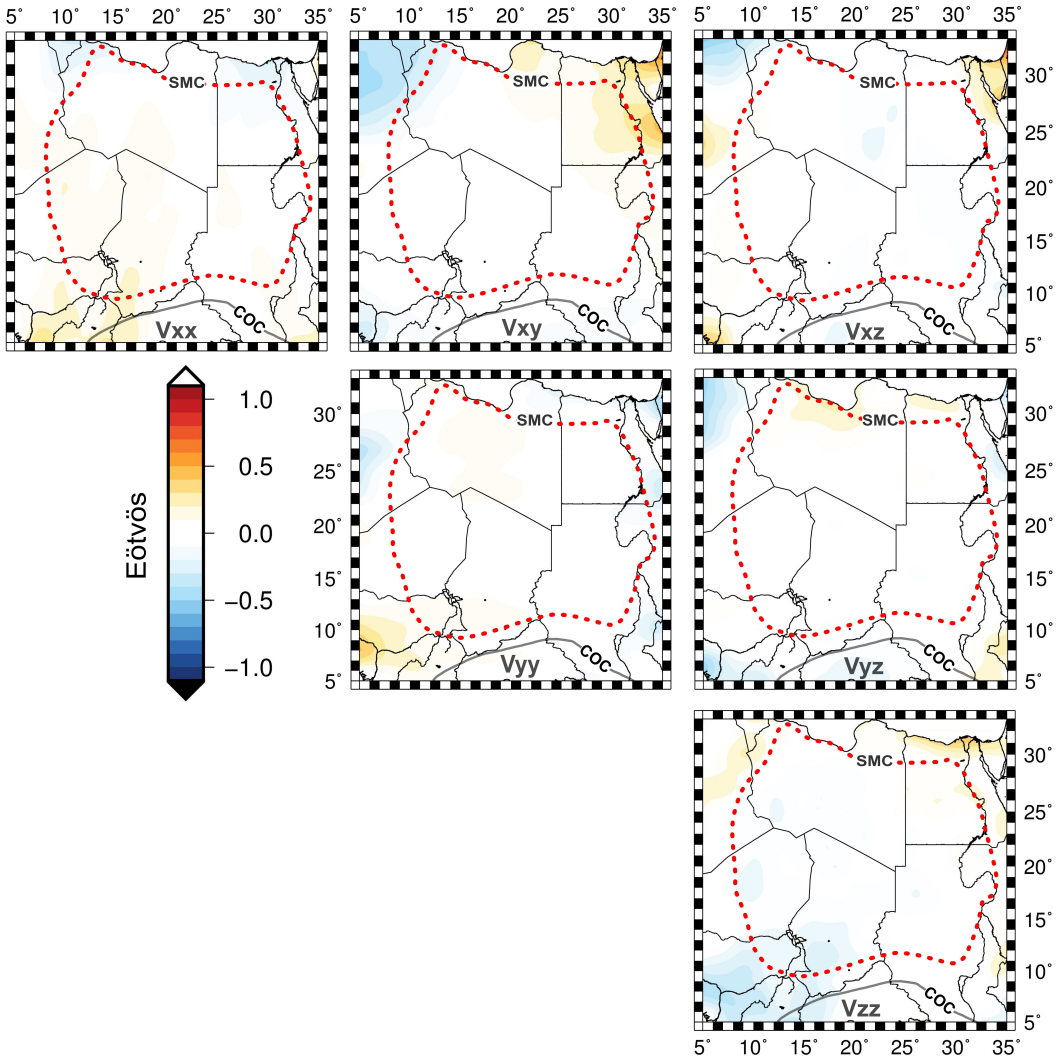

Figure 4.11: Satellite gravity gradients residuals of the last model (M_1).

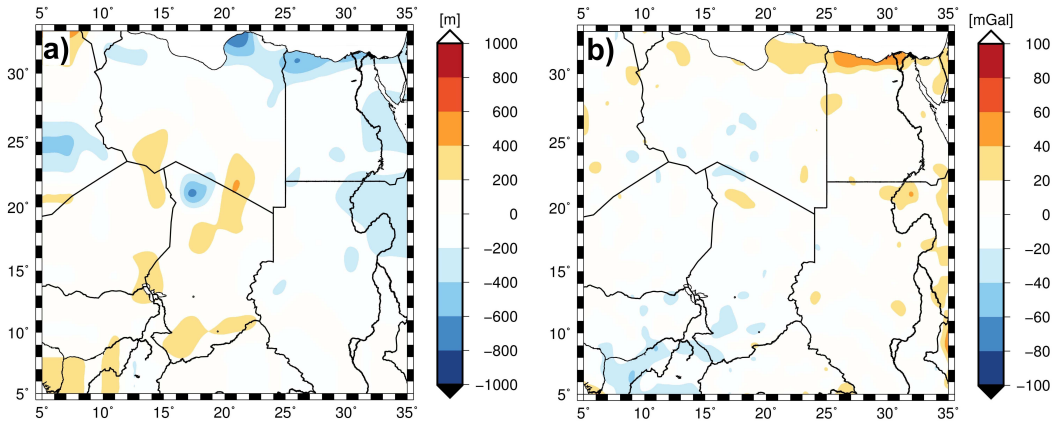

Figure 4.12: Residual field of the last model (M_1), in terms of a) Elevation and b) Bouguer anomaly.

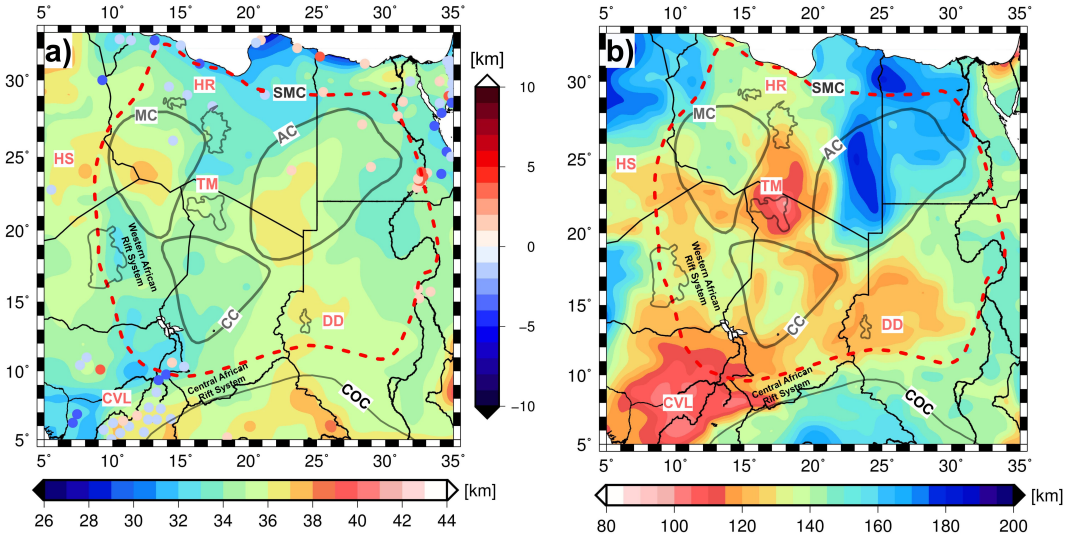

Figure 4.13: The results of the final model (M_1). (a) Moho depth and (b) LAB depth.

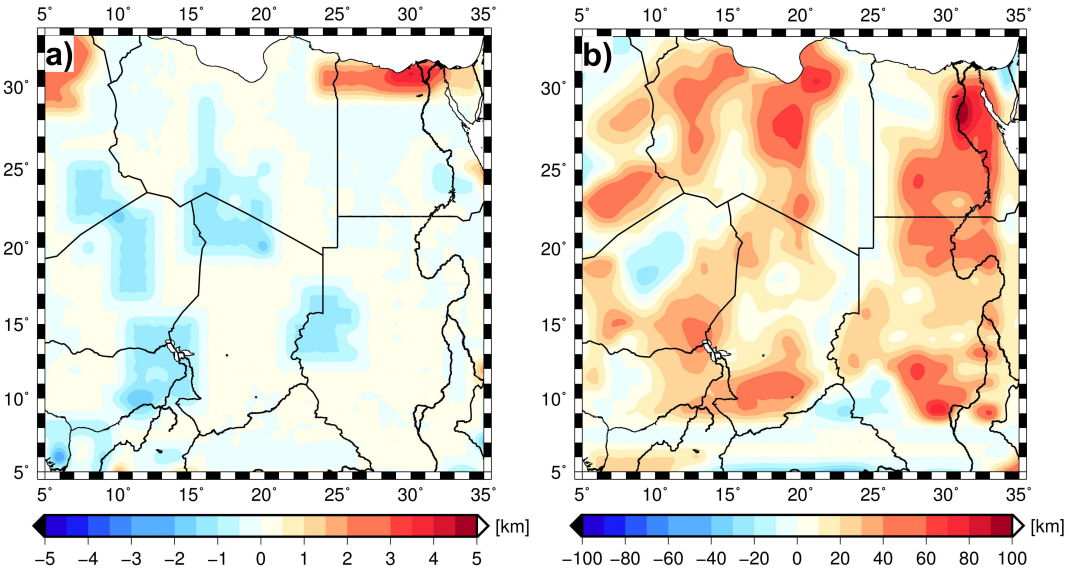

Figure 4.14: a) The differences between the final Moho depth model from LitMod3D and the initial model from the gravity inversion. b) The differences between the final lithospheric thickness from LitMod3D and the initial LAB model from (Fishwick and Bastow, 2011).

It is clearly visible, that the modelled LAB is much deeper than the initial LAB (Fishwick and Bastow, 2011) both in the Eastern part (Al-Kufra cratonic block), the North Central part (Cenozoic volcanism in Libya), and the Eastern Hoggar area. On the South, i.e. Congo craton, the modelled LAB is shallower than the initial LAB with $\sim$ 30 km. The differences between the LAB models arise from the different definitions of the LAB and the different methods used for its compilation. Hence, they are sensitive to other properties. While the tomographic LAB uses a zone of low seismic shear-wave velocity beneath a high-velocity, like the LAB by (Fishwick

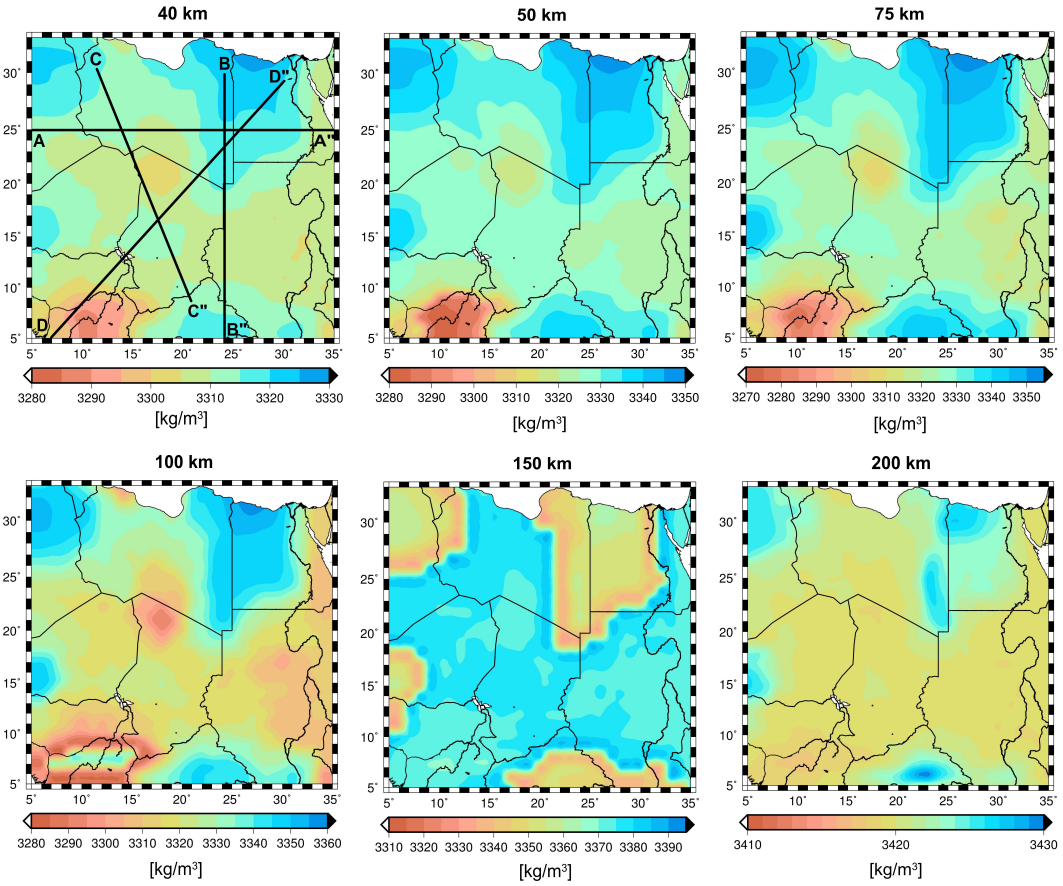

Figure 4.15: Horizontal slices of the 3D density model at 40, 50, 75, 100, 150, and 200 km depths. The locations of profiles A, B, C, and D are indicated by solid lines.

and Bastow, 2011), the LAB constructed by the gravity and gravity gradient data is more sensitive to elastic and isostasy changes.

4.7 Discussion

In the current study, the thermal and compositional structure of the lithosphere and uppermost mantle of the Saharan Metacraton has been assessed using the 3D integrated geophysical-petrological approach allowing for the self-consistent combination of various data sets (Afonso et al., 2008; Fullea et al., 2009).

In the SMC, there are no xenolith samples. Hence, the mantle compositions cannot be related to any direct samples. Therefore, we have tested representative mantle compositions of the SMC corresponding to the last tectono-thermal age of overlying crust, as suggested by (Griffin et al., 2008). All of (Griffin et al., 2008; Djomani et al., 2001) have classified the main mantle domains based on their age and the main mineralogical composition. Such a classification is a good proxy to the true compositions in regions, where no mantle samples are available.

We have modelled the SMC lithosphere using two different compositions, namely, the Proterozoic (Proton) and Phanerozoic (Tecton). In the implemented modelling

approach, the mantle densities and velocities are calculated as a function of the temperature, pressure, and bulk composition based on the thermodynamic calculations. In order to match the observed potential field data and the topography, the results of the Proton composition are clearly favoured over the Tecton composition. In the next sections, we will thoroughly discuss the temperature, density, and velocity structure resulted from our modelling approach.

4.7.1 Density Structure

The mantle density is calculated based on the given mineralogical composition and the in-situ P/T measurements. As displayed in Fig. 4.15 that reports the density values at different depths 40, 75, 100, and 150 km, the results show that the density of the lithosphere in the SMC exhibits notable non-uniform distribution both horizontally and vertically. Also, Fig. 4.15 mainly represents the density variations beneath the Moho depth and in the upper mantle with four cross section (Fig. 4.18, 4.19, 4.20, and 4.21). The density variation at a depth of 100 km, see, Fig. 4.15, shows a very heterogeneous distribution, where the differences between the Al-Kufra craton and the Tibesti Mountains that corresponding to the density variations in the upper mantle, can be easily observed.

The lowest density values are obtained along the Cenozoic Cameroon Volcanic Lines, the Tibesti Mountains, and along the Darfur Dome, which indicate that the upper mantle is significantly warmer beneath such regions.

Significant high-density values anomalies ($3340 - 3350$ kg·m^{-3}) are found along the Al-Kufra cratonic remnant, which belongs to the Proterozoic age. Previous studies of the Proterozoic subcontinental lithospheric mantle (SCLM), based on the interpretation of xenolith data (for instance, consult, (Griffin et al., 2003)), estimated an average density of 3340 kg·m^{-3} at a depth of $\sim$ 100 km and a temperature of $\sim$ 700° C, corresponding to an upper mantle partly depleted in high-density elements (Fe) and mineral phases (Gt).

Such a density value is significantly larger than that of the Archean SCLM (3310 kg·m^{-3}), but also significantly lower than that of the Phanerozoic SCLM (3370 kg·m^{-3}). Additionally, the temperatures of the Proterozoic upper mantle are also characterized by intermediate values between those of the Archean and Phanerozoic upper mantle Griffin et al., 2004. Along Al-Kufra block, the seismic tomography shows a remarkably positive velocity anomaly Fishwick, 2010; Schaeffer and Lebedev, 2013b; Emry et al., 2019. Quantifying the contributions of the compositional effects of the density anomaly is difficult, in particular, when the study area suffers from the absence of mantle-derived xenolith data. Since the maximum expected density differences between a highly depleted Archean and a fertile lithosphere mantle is ca. -100 kg·m^{-3} in shallow lithospheric mantle (Djomani et al., 2001). This difference gradually decreases with depth and, typically, vanishes in the basal part of the lithosphere (Griffin et al., 1999; Griffin et al., 2004).

4.7.2 Temperature Structure

The subsurface temperatures at various horizontal depths are displayed in Fig. 4.18 and as a vertical cross-section (Fig. 4.16). In the upper mantle, strong lateral temperature heterogeneities were observed. At depths 60 to 150 km, temperature differences about 500° C (Fig. 4.16) and ∼ 200° C at 200 km depth were computed. A large-scale low-temperature beneath the Al-Kufra block and the north edge of the Congo craton extends down to ∼ 200 km, which is highly consistent with the recent seismic tomographic results, showing continuous high-velocity in the upper mantle (Emry et al., 2019).

The low-temperature beneath both the Murzuq and Chad blocks extends to ∼ 130 km with no clear boundaries. These low-temperature values correspond to the cold and old lithosphere represented by the cratonic remnant.

Along the Cenozoic volcanic areas of the DD, TM, CVL, and HS, high-temperatures are imaged and characterized by upward deflected isotherms near the LAB (Fig. 4.18, 4.19, 4.20, and 4.21). Beneath the TM, the high-temperature is observed at a depth equivalent to 200 km, which coincides with the locations of the Cenozoic volcanism and low-density values. The extreme high-temperature values reect the presence of a very thin lithosphere due to the upwelling of the mantle along both the Tibesti and CVL. The upper mantle temperature anomalies are confirmed by the recent tomography models (Fischer et al., 2010; Schaeffer and Lebedev, 2013b; Emry et al., 2019), which resolved similar features with an anomalously low-velocity upper mantle. However, the amplitude of the anomaly, its corresponding depth, and the location do differ between the different models. As expected, the pattern of the temperature anomalies (Fig. 4.16) closely mimic the pattern of the LAB thickness. Recently, A 10 km thinning of the mantle transition zone (MTZ) was observed beneath the Cenozoic volcanic provinces in central Libya (Lemnifi et al., 2017), suggesting higher-than-average temperatures in those parts of the MTZ. Along the Al-Kufra cratonic block, the thickness of the MTZ increases indicating a colder-than-average MTZ. These results are consistent with the upper mantle temperature anomaly that we obtained from our model.

4.7.3 Seismic Velocity Structure

Our lithospheric modelling results show high seismic shear velocities that are coincident with the previously proposed cratonic blocks (Al-Kufra, Murzuq, and Chad), with the exception of the Chad cratonic block. Moreover, our results also coincide with the recent seismic tomography models (Fishwick, 2010; Schaeffer and Lebedev, 2013b; Emry et al., 2019).

Fig. 4.17 show depth-slices of Vs at 100 km depth. For a better understanding of the 3D upper mantle velocity structure, vertical cross sections of Vs across four profiles (solid lines in Fig. 4.17-A) are plotted in Fig. 4.18, 4.19, 4.20, and 4.21.

Low-velocity features were detected in the shallow upper mantle beneath the prominent volcanic area throughout the SMC, including the Hoggar and Tibesti as

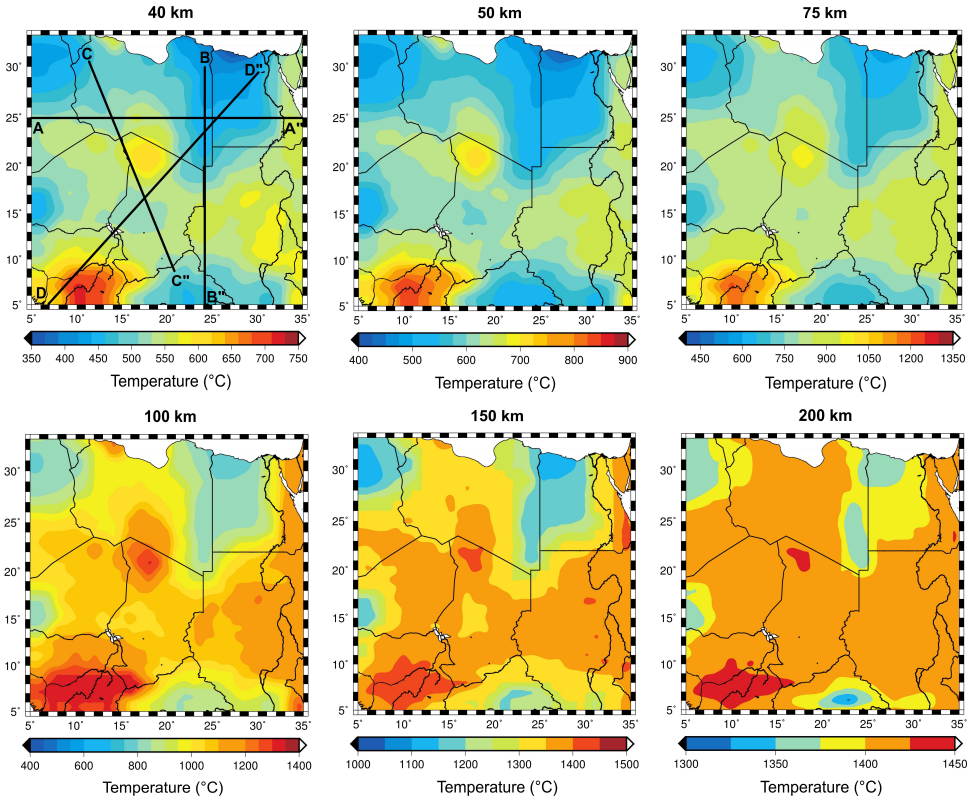

Figure 4.16: Horizontal slices from the 3D temperature model of the SMC at different depths. Lines and text as in Fig. 4.15.

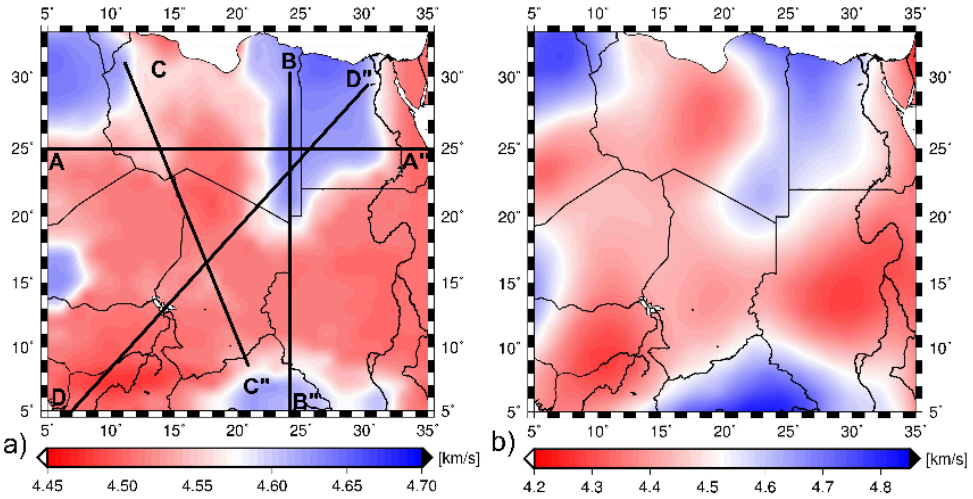

Figure 4.17: (a) Absolute values of S-wave seismic velocity of the final model (M2) at the 100 km depth slice; (b) Seismic tomography model of (Schaeffer and Lebedev, 2013b). The black lines and labels show the loctions of the cross-sections.

well as the Darfur Dome (Fig. 4.17). These low-velocity values coincide with both the lithospheric thinning and the high-temperature values along these regions. The most prominent feature is a high-velocity along the Al-Kufra cratonic block and the northern edge of the Congo craton, which has been resolved by the three recent tomographic models. The high-velocity features along the Al-Kufra cratonic block

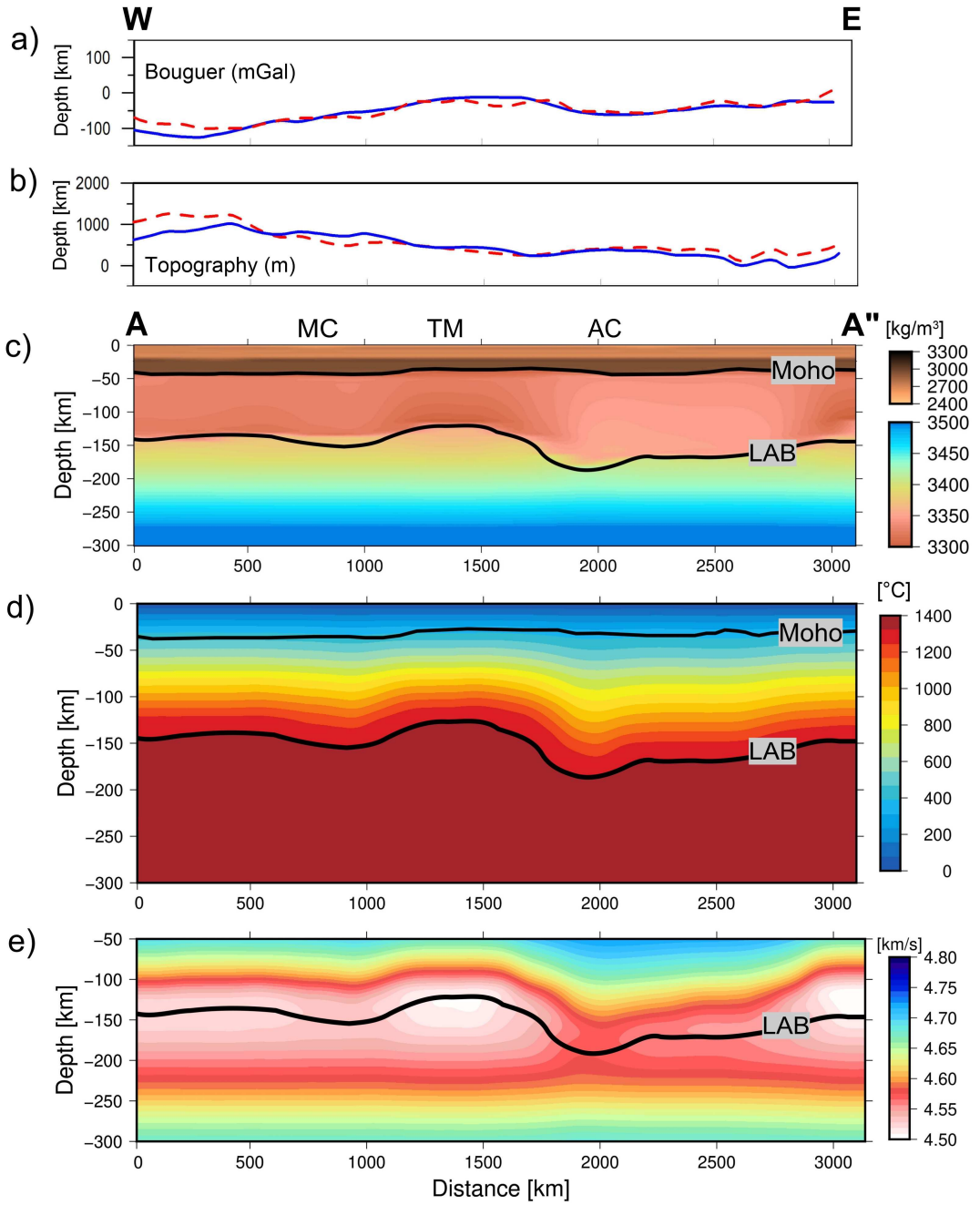

Figure 4.18: Modelling results for A-A profile. Observed (blue solid lines) and calculated (red dashed lines) in terms of (a) Bouguer gravity anomaly and (b) topography, which crosses the Saharan Metacraon in W-E direction. (c), (d) and (e) are the modelled distributions of density, temperature, and S-wave seismic velocity, respectively. Continuous black lines indicate Moho and/or LAB depth geometry. MC = Murzuq cratonic remnants; TM = Tibesti Massif; and AC = Al-Kufra cratonic remnants.

are consistent with the recent tomographic models at a global scale (Schaeffer and Lebedev, 2013b) and at a continental scale (Fishwick and Bastow, 2011; Emry et al., 2019).

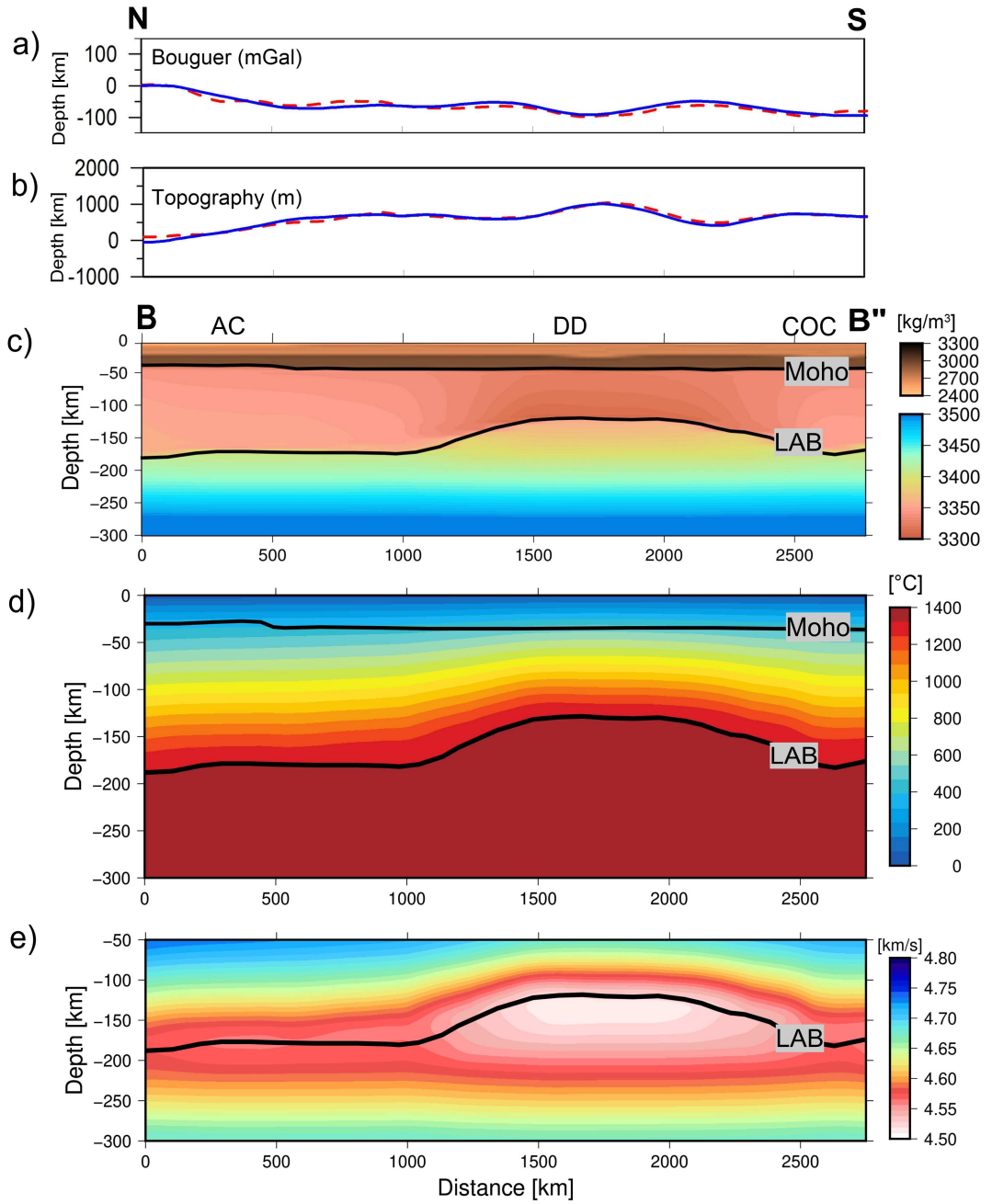

Figure 4.19: Modelling results for B-B profile. Observed (blue solid lines) and calculated (red dashed lines) in terms of (a) Bouguer gravity anomaly and (b) topography that crosses the Saharan Metacraon in N-S direction. (c), (d) and (e) are the modelled distributions of density, temperature, and S-wave seismic velocity, respectively. Continuous black lines indicate Moho and/or LAB depth geometry. AC = Al-Kufra cratonic remnants; DD = Darfur Dome; and COC= Congo craton.

4.7.4 Surface Heat Flow (SHF)

The computed SHF from our model is the result of the mantle contribution (controlled by the depth to the LAB) together with the radiogenic heat production and the thermal conductivities of the crustal layers. The predicted surface heat flow

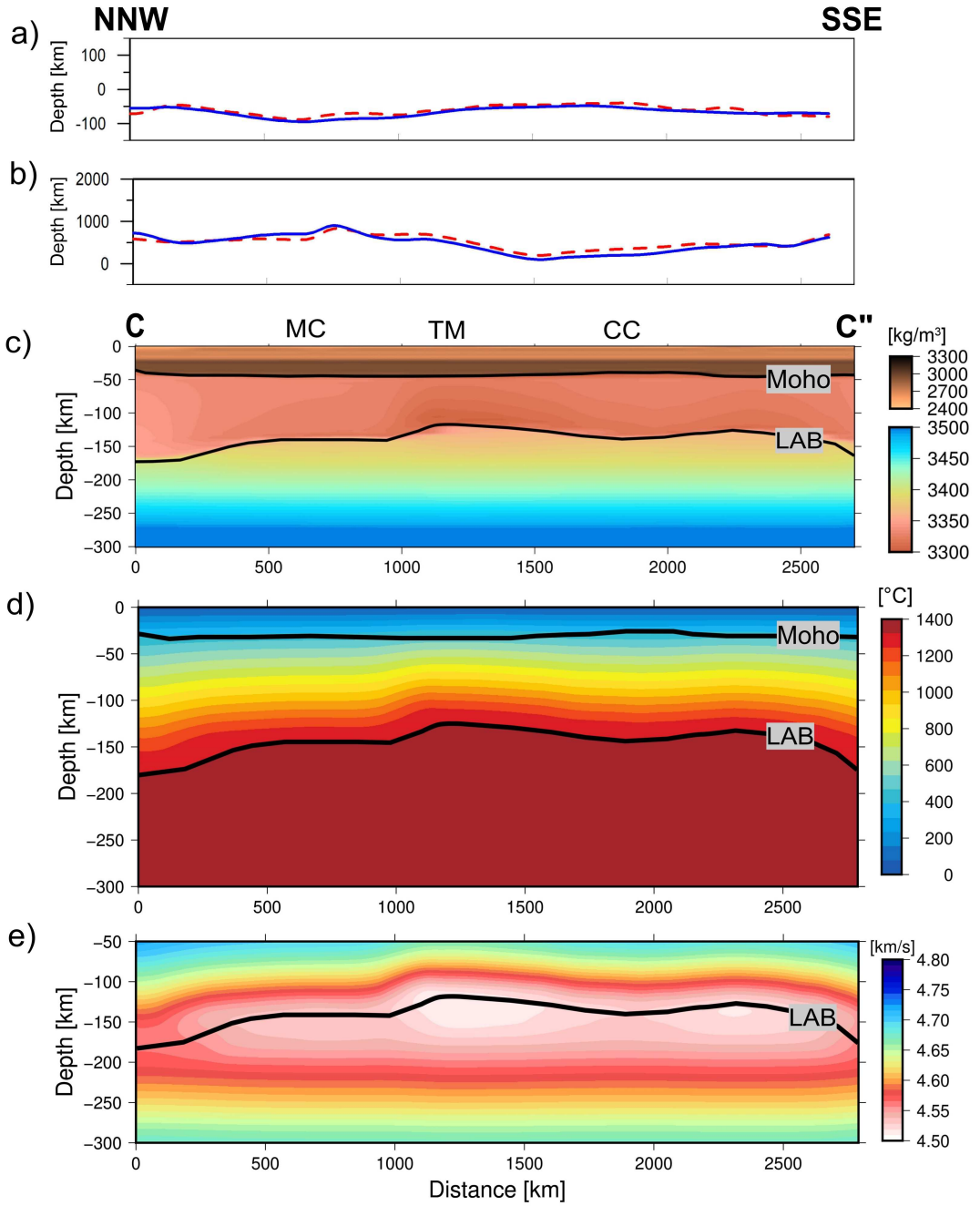

Figure 4.20: Modelling results for C-C profile. Observed (blue solid lines) and calculated (red dashed lines) in terms of (a) Bouguer gravity anomaly and (b) topography that crosses the Saharan Metacraon in NNW-SSE direction. (c), (d) and (e) are the modelled distributions of density, temperature, and S-wave seismic velocity, respectively. Continuous black lines indicate Moho and/or LAB depth geometry. MC = Murzuq cratonic remnants; TM= Tibesti Massif; and CC= Chad cratonic remnants.

(Fig. 4.22) shows a large variability, ranging from $\sim 40 - 50$ mW·m^{-2}, which corresponds to a modified Archean-Proterozoic lithosphere (Artemieva, 2006) along the Al-Kufra cratonic remnant and the northern edge of Congo craton to $55 - 60$ mW·m^{-2} associated with the Tibesti Mountains and Darfur Dome.

The maximum surface heat flow (SHF) values are greater than 65 mW·m^{-2} around

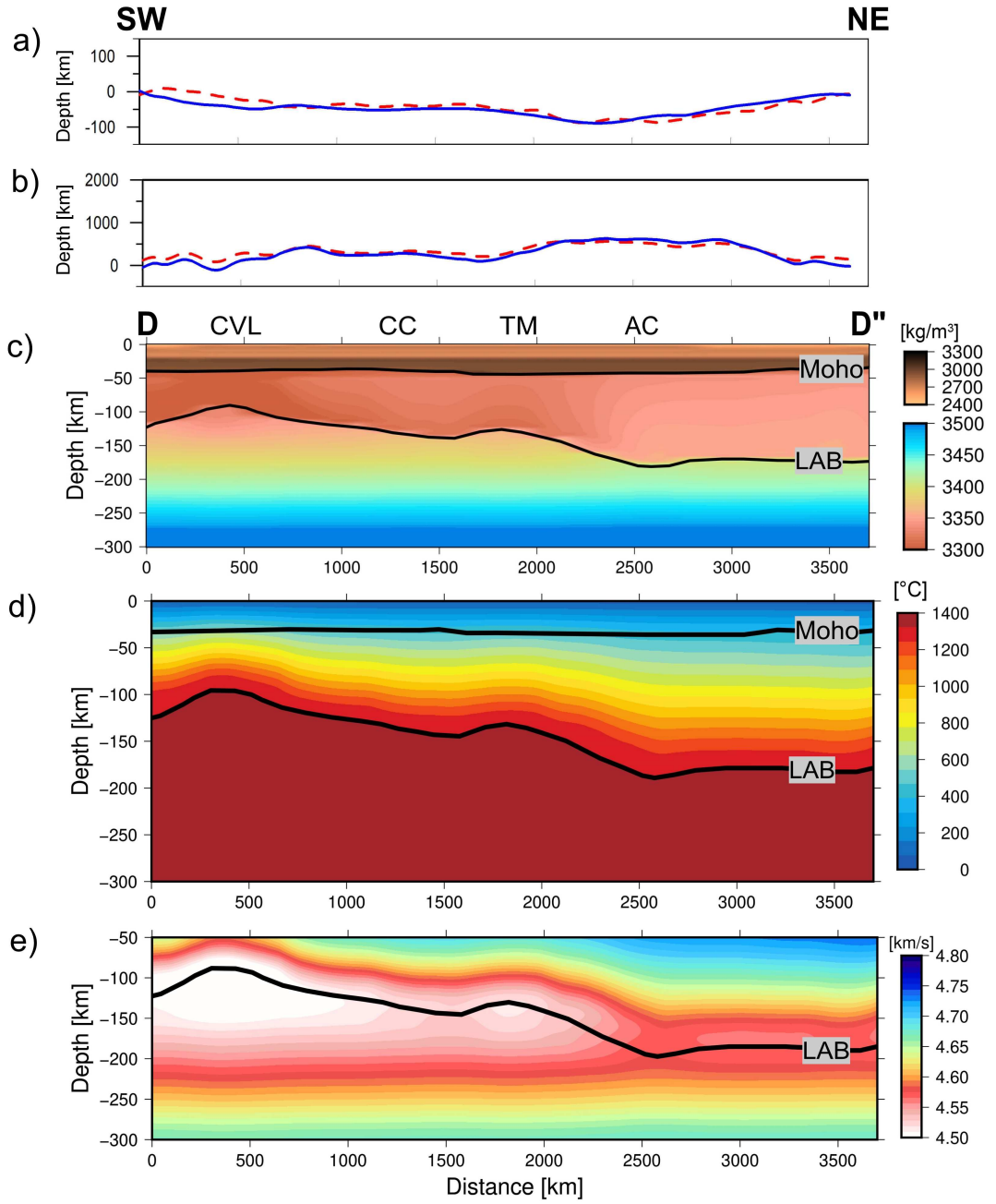

Figure 4.21: Modelling results for D-D profile. Observed (blue solid lines) and calculated (red dashed lines) in terms of (a) Bouguer gravity anomaly and (b) topography that crosses the Saharan Metacraon in SW-NE direction. (c), (d) and (e) are the modelled distributions of density, temperature, and S-wave seismic velocity, respectively. Continuous black lines indicate Moho and/or LAB depth geometry. CVL = Cameroon Volcanic Line; CC= Chad cratonic remnants; TM= Tibesti Massif; and AC = Al-Kufra cratonic remnants.

the Cameroon Volcanic Lines. The predicted SHF suggests that the Al-Kufra is underlain by a rigid lithospheric block with a thick and cold lithosphere, which may be mostly surrounded by a thin and rheologically weak mantle.

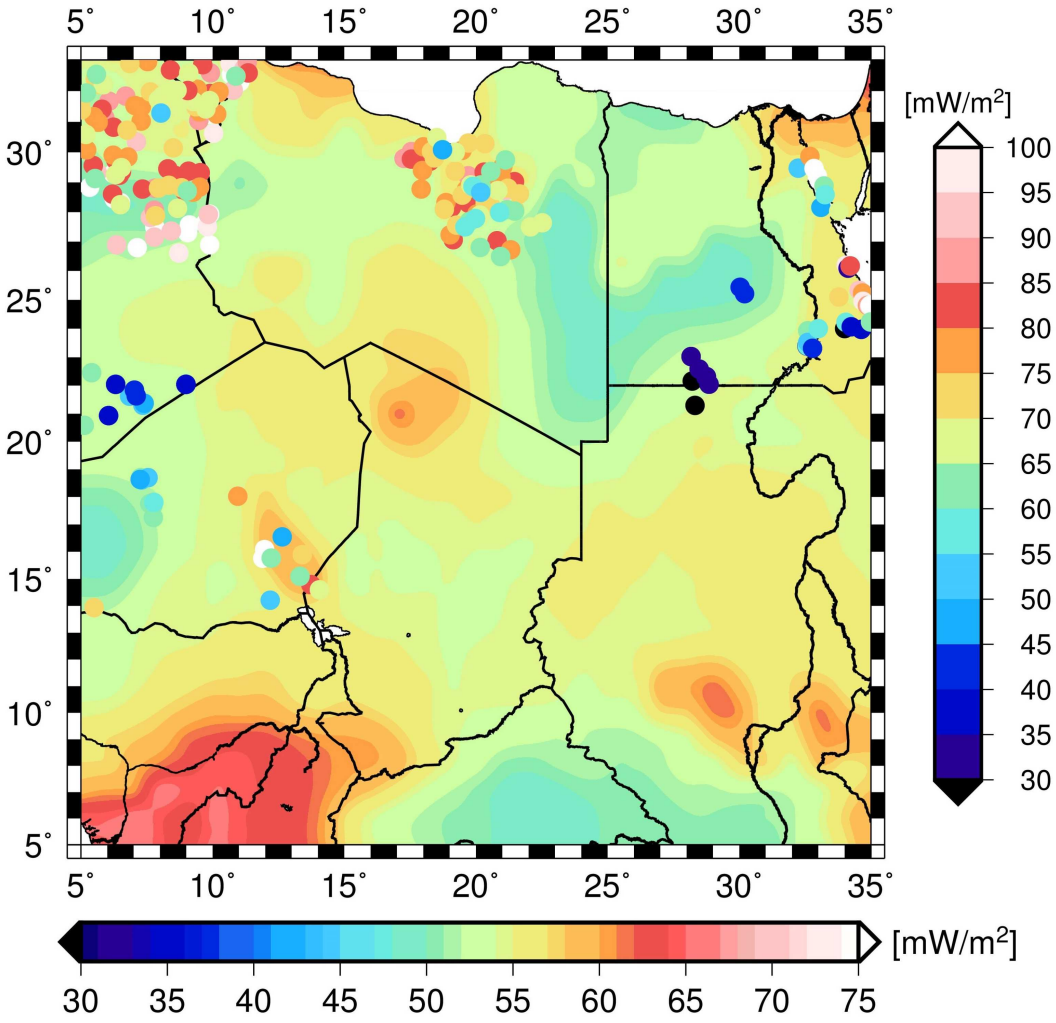

Figure 4.22: Predicted surface heat flow in the Saharan Metacraton. Dots show the values of the available measured heat flow from the global dataset Pollack, Hurter, and Johnson, 1993.

The validation of the predicted SHF results is not strong due to the poorly constrained thermal structure of the internal part of the SMC, and due to the availability of few heat flow data that are sparsely distributed.

We observed that the predicted heat flows are partially in contrast with the available measured points from boreholes, the amplitudes of the lateral variations are higher in some areas (e.g., across Al-Kufra block) and lower in other areas (e.g., across Sirt basin). Some of these discrepancies can be attributed to our simplified crustal model. Additionally, the lateral variations in crustal thermal properties (radiogenic heat production and thermal conductivity) are not included in either the crystalline or the sedimentary layers, which could affect the predicted heat flow locally. We note, however, that although the SHF observations are useful as broad constraints, they are not heavily weighted as constraining data in this study due to the sparsity of the data available and the local geological variations (e.g., in thermal conductivity) that might be affecting them.

4.7.5 Upper Mantle Thermal Anomaly and Cenozoic Volcanism

The origin of the Cenozoic volcanism inside the SMC is debatable and three contrasting models have been proposed.

1. The association is a manifestation of a deep mantle plume (Burke and Wilson, 1976; Sicilia et al., 2008), possibly linked to the postulated Afar Plume (Sebai et al., 2006), although the typical geological features of plumes are poorly represented (Zhao, 2007);

2. Alternatively, the swell and volcanism are the results of the reactivation of lithospheric structures due to the intraplate stress generated by the Africa-Europe collision (Liégeois et al., 2005; Pik, Marty, and Hilton, 2006; Radivojević et al., 2015).

From our model, we found that the Cenozoic volcanism areas are associated with the upper mantle thermal anomaly and controlled by lithospheric architecture. The thin MTZ along these volcanic areas is an additional evidence of the high-temperature anomaly beneath these regions. Such interpretation is also consistent with our results for the present-day lithospheric thinning and temperature anomaly beneath these volcanic areas.

4.7.6 Lithospheric Structure and Metacratonization of the Saharan Region

Our results confirm the presence of three preserved cratonic remnants (Al-Kufra, Murzuq, and Chad) within the Saharan Metacraton that are underlain by a relatively thicker, colder, and denser SCLM characterized by high S-wave velocities. This is in contrast with the rest of the Saharan Metacraton, which is underlain by a relatively thinner, hotter, and less dense SCLM with relatively slower S-wave velocity values.

Moreover, we observed that the surface extents of the three cratonic remnants coincide with the broad depressions around relatively elevated regions (topographic swells) including the Darfur Dome, the Tibesti Massif, and the Hoggar Swell (Fig. 4.3). Also, the surface extents of the cratonic remnants coincide with the presence of the Paleozoic-Mesozoic sedimentary basins including the Al-Kufra, the Murzuk, and the Chad.

It seems that, during the Pan-African orogeny and the Phanerozoic, the cratonic blocks (e.g., the Murzuq and Al-Kufra) played an important role as rheologically rigid bodies. The presence of the thicker and denser SCLM beneath the cratonic remnants might have resulted in the development of negative buoyancy that allowed the formation of these sedimentary basins as broad intra-continental sag basins.

The presence of magmatism along the cratonic blocks boundaries, where the Cenozoic volcanic field is present might have induced the process that modified the lithospheric mantle beneath the SMC, which, in turn, may finally lead to the gravitational instability and destruction of the lower part of the lithosphere (Fezaa et al., 2010; Liégeois et al., 2013). Moreover, a high-temperature anomaly is imaged around the cratonic blocks within the SMC and its distribution correlates well with the location of the recent volcanism in the region. This anomaly seems to be related to

the up-welling of the sub-lithospheric material, which creates forced down-wellings and erosion of the basal parts of the lithosphere.

Our model illustrates the present state of the lithospheric structure of the Saharan Metacraton and the three enclosed cratonic remnants. Such lithospheric structure might have been the product of multiple geological events that occurred during different geologic times. Hence, this poses the question of when the Saharan Metacraton acquired its present lithospheric structure and what could be the relative contributions of each tectonic event. Also, the presence of the three cratonic remnants within the vastly remobilized Saharan Metacraton poses the question of what controlled the metacratonization process and how the three cratonic remnants escaped metacratonization.

(Liégeois et al., 2013) attributed the metacratonization of the interior of the once Saharan craton, not just its margin, to that the craton was subjected to collisional events in the Neoproterozoic along its entire margins. In the East, it collided with the Arabian-Nubian Shield. To the West, it collided with the Tuareg Shield, which in turn collided with the West African craton. In the south, it collided with the Congo craton. **LpIEGEOIS2013220** also, suggested that the Saharan craton was colliding against an unidentified continent in the North that is buried under the Phanerozoic sedimentary rocks of North Africa. Hence, the geodynamic setting of the Saharan craton during the Neoproterozoic favours significant shortening of the entire craton. This would certainly lead to instability in the form of lithospheric thickening that will be, consequently, followed by a total or partial SCLM delamination beneath the Moho or beneath the mechanical boundary layer-thermal boundary layer. It is possible that such delamination occurred along ancient collisional zones that stitched the fragments of the Saharan craton together. It is not unusual to have large cratons made-up of smaller Archean-Paleoproterozoic lithospheric fragments that were sutured together along Paleoproterozoic orogenic belt. For example, in Southern Africa, the larger Kalahari craton is made-up of the smaller Archean-Paleoproterozoic Zimbabwe and Kaapvaal cratons sutured by the Paleoproterozoic Limpopo, Magondi, and Kheis orogenic belts (Begg et al., 2009). So, it is possible that the Saharan craton had a similar tectonic setting before its metacratonization during the Neoproterozoic collisional events.

Little information are known about the Precambrian geology of the regions surrounding the three cratonic remnants within the Saharan Metacraton because of lack of exposures and lack of geological investigation due to their remote locations. However, there are observations that might have had different structural styles than the three cratonic remnants (although they were part of the intact Saharan craton). This allowed these regions to be preferentially metacratonized as well as influenced by the subsequent modification of the Saharan Metacraon's lithosphere during the Phanerozoic.

4.7.7 Conclusion

Our 3D lithospheric model of the Saharan Metacraton combines geophysical, geological, and petrological constraints at various scales into one robust and self-consistent

model. The modelling approach calculates the temperature, density, and seismic velocity of the upper mantle as a function of different P-T conditions and petrological composition, aiming to examine the potential existence of three preserved cratonic remnants within the Saharan Metacraton.

Our lithospheric model is able to explain both the observed seismic velocities and the measured geophysical and geodetic data, under the assumption that it is uniformly moderately depleted (i.e., typical Proterozoic mantle). Furthermore, our preferred models suggest that the lithospheric structure of these cratonic remnants is different from that of the main Saharan Metacraton in term of lithospheric thickness. The cratonic remnants are modelled with a relatively thick and, consequently, a colder and denser SCLM, while the SCLM beneath the remaining Saharan Metacraton is modelled as a relatively thin and, consequently, a hotter and less dense layer.

Therefore, our developed models propose that the SCLM of the cratonic remnants has relatively faster S-wave velocities compared to the metacraton, which are in agreement with the seismic tomography models, both, in regional and local scales. This can be interpreted as localized and partial metacatonization of the ancestral craton of the Saharan Metacraton during the Neoproterozoic collisional-related delamination event. The localized modification of the Saharan Metacraton SCLM might have been further enhanced by Phanerozoic events such as Mesozoic-Cenozoic rifting and Cenozoic volcanic activities.

Chapter 5

Conclusions and Outlook

5.1 Conclusions

During this PhD project, new insights on the present-day lithosphere structure of Egypt and the Saharan Metacraton consistently with geological and geophysical data, and seismic tomography models was developed.

First, a new combined regional gravity model has been developed for Egypt utilizing the recently made available terrestrial FA gravity anomalies integrated with the satellite gravity data. The terrestrial data used in this study, characterized by consistent gravity and height values, were exploited for the first time over the Egyptian territory.

The developed combined gravity model brings together the useful aspects of both types of data, the high resolution of terrestrial gravity data and the unprecedented homogeneity of GOCE satellite data.

The combined model, which is developed by integrating satellite and terrestrial data via applying the remove-compute-restore (RCR) principle and the least-squares collocation (LSC) procedure, would definitely be of added-value for geophysical and geodetic applications where no or only sparse ground data are available. In addition, the method may be useful when combining other heterogeneous datasets of different resolution, e.g. onshore gravity data with offshore satellite data.

As a second step, the combined regional gravity field model used for building the detailed three-dimensional density model for Egypt. First, The GOCE satellite gravity data was inverted to obtain an initial model by applying the regularized non-linear gravity inversion (Uieda and Barbosa, 217). Then, the 3D gravity model was constrained using the available deep seismic profiles, receiver functions, and geological information in order to produce a regional model of the crustal thickness for the continental part of Egypt. The developed Moho depths model was compared with compilations of the seismic estimates showing good agreements as well as high levels of consistency.

The resulting crustal thickness correlates better with the geological and tectonic structure. The results show crustal thicknesses ranging from 25 km to 40 km. More

specifically, crustal thickness ranges from 36 km to 40 km in the southern portion of the Egyptian territory, which can be associated with the modification of the crust that occurred during the collision between East Gondwana and the Sahara Metacraton along the Keraf suture zone during the final assembly of Gondwana in the Neoproterozoic. The crustal thickness along the rifted margins of the Red Sea ranging between 25 km and 30 km, then becomes thinner toward the Mediterranean Sea.

The crustal model presented here studying the 3D density structure of geologically-interesting formations, where the Bouguer anomaly data is combined with a priori information retrieved from petrophysical (e.g., density values) and seismic datasets. Compared to previous studies, the developed gravity-based Moho model shows a better match with the available seismic studies than that of the global crustal model (e.g., the CRUST1.0 and GEMMA), in which the interpolation of such global models on local scales might produce unrealistic Moho depth values.

Looking much regional, surroundings the Egyptian territory, the lithospheric structure of the Saharan Metacraton are presented. Finally, the 3D lithospheric model of the Saharan Metacraton combines a geophysical, geological, and petrological constraints at various scales into one robust and self-consistent model. The modelling approach calculates the temperature, density, and seismic velocity of the upper mantle as a function of different P-T conditions and petrological composition, aiming to examine the potential existence of three preserved cratonic remnants within the Saharan Metacraton. The resulted lithospheric model able to explain both observed seismic velocities and measured geophysical and geodetic data assuming is uniformly moderately depleted (i.e., typical Proterozoic mantle).

Furthermore, our preferred models suggest that the lithospheric structure of these cratonic remnants is different from that of the main Saharan Metacraton in term of lithospheric thickness. The cratonic remnants are modelled with a relatively thick, and consequently colder and denser SCLM, while the SCLM beneath the remaining Saharan Metacraton is modelled as relatively thin and consequently hotter and less dense.

The models consequently propose that the SCLM of the cratonic remnants has relatively faster S-wave velocities compared to the metacraton in agreement with the seismic tomography models in both regional and local scales. This can be interpreted as localized and partial metacatonization of the ancestral craton of the Saharan Metacraton during Neoproterozoic collisional-related delamination event. The localized modification of the Saharan Metacraton SCLM might have been further enhanced by Phanerozoic events such as Mesozoic-Cenozoic rifting and Cenozoic volcanic activities. The spatial distributions of Cenozoic volcanisms around the cratonic blocks are explained in our model by low velocity and hot temperature associated with a thinner lithosphere, implying mantle upwelling.

In summary, this Thesis has provided new insights on the present-day lithosphere structure of Egypt and the Saharan Metacraton consistently with geological and geophysical data, and seismic tomography models. Hopefully, this work will help to better understand the upper mantle structure and its contribution to the present configuration of the Saharan Metacraton.

5.2 Outlook

The research conducted through this thesis has shown several issues and limitations which should be considered and solved in future research. In this section, some recommendations for future work are addressed.

- The Saharan Metacraton region suffer large data gaps of terrestrial gravity measurements. Filling these gaps with terrestrial/airborne gravity data will be required for the interpretation of the more reliable lithospheric density distribution in the region. Although the latest geopotential model EIGEN-6C4 (Bruinsma et al., 2014) considered as a combined model, but in this area no terrestrial gravity data were available and the model based on fill-in data over this area.

- More seismological data across the region can help to diversify the model's geometry in order to establish different layers with unique borders and set more precise apriori assumptions for each.

- Further geophysical studies such as heat flow data, denser magnetotelluric profiles for the Saharan Metacraton should be addressed in the future in order to obtain better constraints on the deep structure and density of the lithosphere beneath this important region.

- The high-resolution thermochemical modelling of the Saharan Metacraton lithosphere can be imaged by jointly inverting the dispersion curves derived from the recent tomography model of Africa (Emry et al., 2019) with the geoid height, surface heat flow, absolute elevation, and magnetotelluric data with a multi-observable probabilistic inversion method.

- The metacratonization process, actual causes, mechanisms, and extent of the lithospheric modification remain ambiguous. Combining the structural images obtained by present-day high-resolution lithospheric modelling and the geodynamic simulations inspired by numerical modelling, would explain the geodynamic mechanism and the possible scenarios of the Saharan Metacraton modifications.

Appendix A

Appendix A: Effect of Lithospheric Composition Changes

We have tested various lithospheric mantle compositions in order to evaluate the effects of these changes on the modelled geophysical observables (Bouguer anomaly, geoid, and topography) and the predicted temperature, density, and S-wave velocity. We considered two end-member scenarios, in which the SCLM of the entire Saharan Metacraton is either of Archean or Phanerozoic age Griffin et al., 2008.

Several experiments have shown that the Archean SCLM has the highest magnesium and lowest iron content with a moderate magnesium number and the lowest bulk density. Differently, the Phanerozoic SCLM is characterized by lower magnesium number and higher iron content and higher bulk density Djomani et al., 2001; Grad, Tiira, and Group, 2009.

First, we kept the crust and the SCLM geometry and thickness fixed and only changed the petrological composition of the SCLM of B-B profile. We considered the SCLM composition to be either of uniform depleted Archean composition or uniform fertile Phanerozoic composition. Modelling the entire Saharan Metacraton's SCLM as a depleted Archean composition causes major misfit between the observed and the calculated Bouguer anomaly (RMSE = 25 mGal), the geoid (RMSE = 4.5 m) and the topography (RMSE = 242 m). For example, such a scenario would result in the increase of the elevation of the calculated topography by $\sim$ 240 m compared to the observed topography (Fig. A.1-A).

Therefore, it would be very difficult to compensate such mass unbalance by simply modifying the thickness of the crust. Such modifications would require an extremely unrealistic thin crust that should have extremely high density. Therefore, considering the entire SCLM of the Saharan Metacraton to have a uniform depleted Archean composition can be ruled out. Modelling the SCLM beneath the Saharan Metacraton along profile B-B as a uniform fertile Phanerozoic composition (Fig. A.1-B) will also cause major misfit between the observed and the calculated Bouguer anomaly (RMSE = 23 mGal), the geoid (RMSE = 3.0 m) and the topography (RMSE = 306 m). For example, such a scenario will lead to the lowering of the elevation of the calculated topography by $\sim$ 300 m compared to the observed topography (Fig. A.1).

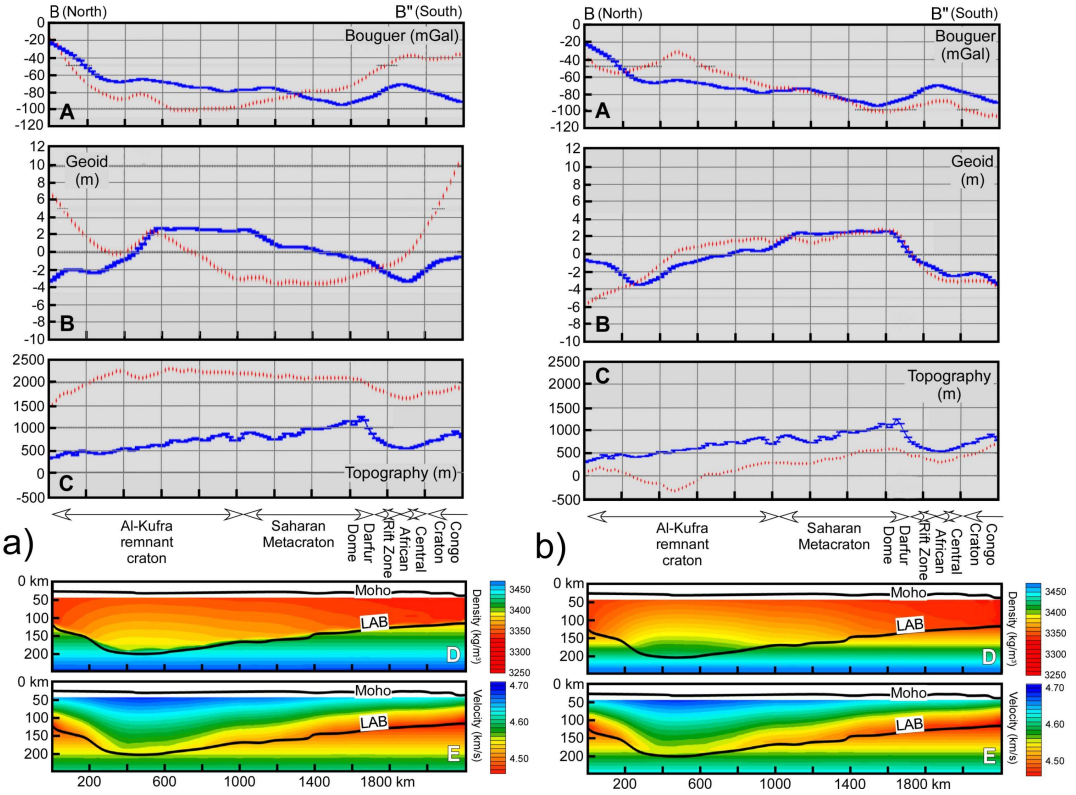

Figure A.1: The modelling results of the Saharan Metacraton considering a) the SCLM of the entire metacraton as a uniform depleted Archean composition along B–B profile, which crosses the Al Kufrah cratonic remnant; b) considering the SCLM of the entire metacraton as a uniform fertile Phanerozoic composition. (A) The Misfit between the observed and the calculated Bouguer anomaly, (B) the geoid, and (C) the topography. (D) The calculated SCLM density. (E) The calculated SCLM S-wave seismic velocities.

Bibliography

Abd-Elmotaal, H. (2008). "Gravimetric geoid for Egypt using high-degree tailored reference geopotential model". In: *NRIAG Journal of Geophysics special issue*, pp. 507–531.

Abd-Elmotaal, H. et al. (2018). "AFRGDB_V2. 0: The gravity database for the geoid determination in Africa". In:

Abdelrahman, E. M., E. M. Refai, and H. M. El-Ghalban (1988). "Gravity models of the Nile Delta basin, Egypt". In: *Egyptian Geological Survey Proceedings of 6^{TH} Annual Meeting*. Vol. 27, p. 33.

Abdelsalam, M. G. and A. S. Dawoud (1991). "The Kabus ophiolitic melange, Sudan, and its bearing on the western boundary of the Nubian Shield". In: *Journal of the Geological Society* 148.1, pp. 83–92. ISSN: 0016-7649. DOI: 10.1144/gsjgs.148.1.0083. eprint: http://jgs.lyellcollection.org/content/148/1/83.full.pdf. URL: http://jgs.lyellcollection.org/content/148/1/83.

Abdelsalam, M. G., S. S. Gao, and J.-P. Liégeois (2011). "Upper mantle structure of the Saharan Metacraton". In: *Journal of African Earth Sciences* 60.5, pp. 328 –336. ISSN: 1464-343X. DOI: https://doi.org/10.1016/j.jafrearsci.2011.03.009. URL: http://www.sciencedirect.com/science/article/pii/S1464343X11000653.

Abdelsalam, M. G., J.-P. Liégeois, and R. J. Stern (2002). "The Saharan Metacraton". In: *Journal of African Earth Sciences* 34.3, pp. 119 –136. ISSN: 1464-343X. DOI: https://doi.org/10.1016/S0899-5362(02)00013-1. URL: http://www.sciencedirect.com/science/article/pii/S0899536202000131.

Abdelsalam, M. G. and R. J. Stern (1996a). "Mapping Precambrian structures in the Sahara Desert with SIR-C/X-SAR radar: The Neoproterozoic Keraf Suture, NE Sudan". In: *J GEOPHYS RES-PLANET* 101.E10, pp. 23063–23076. DOI: https://doi.org/10.1029/96JE01391. eprint: https://agupubs.onlinelibrary.wiley.com/doi/pdf/10.1029/96JE01391. URL: https://agupubs.onlinelibrary.wiley.com/doi/abs/10.1029/96JE01391.

— (1996b). "Sutures and shear zones in the Arabian-Nubian Shield". In: *J AFR EARTH SCI* 23.3. IGCP 348 (Mozambique and Related Belts), pp. 289 –310. ISSN: 1464-343X. DOI: https://doi.org/10.1016/S0899-5362(97)00003-1. URL: http://www.sciencedirect.com/science/article/pii/S0899536297000031.

Abdelsalam, M. G. et al. (1998). "The Neoproterozoic Keraf Suture in NE Sudan: Sinistral Transpression along the Eastern Margin of West Gondwana". In: *J Geol* 106.2, pp. 133–148. DOI: https://doi.org/10.1086/516012. eprint: https://doi.org/10.1086/516012. URL: https://doi.org/10.1086/516012.

Abdelwahed, M. F., S. El-Khrepy, and A. Qaddah (2013). "Three-dimensional structure of Conrad and Moho discontinuities in Egypt". In: *J AFR EARTH SCI* 85, pp. 87 –102. ISSN: 1464-343X. DOI: https://doi.org/10.1016/j.jafrearsci.

2013.04.007. URL: http://www.sciencedirect.com/science/article/pii/S1464343X13000836.

Afonso, J. C. et al. (2008). "Integrated geophysical-petrological modeling of the lithosphere and sublithospheric upper mantle: Methodology and applications". In: *Geochemistry, Geophysics, Geosystems* 9.5. DOI: 10.1029/2007GC001834. eprint: https://agupubs.onlinelibrary.wiley.com/doi/pdf/10.1029/2007GC001834. URL: https://agupubs.onlinelibrary.wiley.com/doi/abs/10.1029/2007GC001834.

Aitken, A. R. A., M. L. Salmon, and B. L. N. Kennett (2013). "Australia's Moho: A test of the usefulness of gravity modelling for the determination of Moho depth". In: *TECTONOPHYSICS* 609. Moho: 100 years after Andrija Mohorovicic, pp. 468 –479. ISSN: 0040-1951. DOI: https://doi.org/10.1016/j.tecto.2012.06.049. URL: http://www.sciencedirect.com/science/article/pii/S0040195112003745.

Al-Damegh, K., E. Sandvol, and M. Barazangi (2005). "Crustal structure of the Arabian plate: new constraints from the analysis of teleseismic receiver functions". In: *EARTH PLANET SCI LETT* 231.3, pp. 177 –196. ISSN: 0012-821X. DOI: https://doi.org/10.1016/j.epsl.2004.12.020. URL: http://www.sciencedirect.com/science/article/pii/S0012821X04007381.

Allen, P. A. and J. R. Allen (2005). *Basin Analysis: Principles and Applications*. Wiley-Blackwell.

Alnaggar, D. (1986). "Determination of the geoid in Egypt using heterogeneous geodetic data". PhD thesis. Ph.D. Dissertation, Cairo University, Egypt.

Alvers, M. R. et al. (2014). "A novel warped-space concept for interactive 3D-geometry-inversion to improve seismic imaging". In: *First Break* 32.4.

Alvers, M. R. et al. (2015). "?' Quo vadis inversión?" In: *First break* 33.4, pp. 65–74.

Amante, C. (2009). "ETOPO1 1 arc-minute global relief model: procedures, data sources and analysis". In: *http://www. ngdc. noaa. gov/mgg/global/global.html*.

André, L., J. Klerkx, and M. T. Busrewil (1991). "Geochemical and Rb–Sr isotopic data on felsic rocks from the Jabal al Awaynat alkaline intrusive complex (SE Libya)". In: *The geology of Libya* 7, pp. 2511–2527.

Arrell, K. et al. (2008). "Spectral filtering as a method of visualising and removing striped artefacts in digital elevation data". In: *Earth Surface Processes and Landforms: The Journal of the British Geomorphological Research Group* 33.6, pp. 943–961.

Artemieva, I. M. (2006). "Global 11 thermal model TC1 for the continental lithosphere: Implications for lithosphere secular evolution". In: *Tectonophysics* 416.1. The Heterogeneous Mantle, pp. 245 –277. ISSN: 0040-1951. DOI: https://doi.org/10.1016/j.tecto.2005.11.022. URL: http://www.sciencedirect.com/science/article/pii/S0040195105006256.

Ashwal, L. D. and K. Burke (1989). "African lithospheric structure, volcanism, and topography". In: *Earth and Planetary Science Letters* 96.1, pp. 8 –14. ISSN: 0012-821X. DOI: https://doi.org/10.1016/0012-821X(89)90119-2. URL: http://www.sciencedirect.com/science/article/pii/0012821X89901192.

Bailey, D. K. (1992). "Episodic alkaline igneous activity across Africa: implications for the causes of continental break-up". In: *Geological Society, London, Special Publications* 68.1, pp. 91–98. ISSN: 0305-8719. DOI: 10.1144/GSL.SP.1992.068.01.06. eprint: http://sp.lyellcollection.org/content/68/1/91.full.pdf. URL: http://sp.lyellcollection.org/content/68/1/91.

Barzaghi, R. et al. (1993). "Spectral techniques in inverse Stokes and overdetermined problems". In: *Surveys in Geophysics* 14.4-5, pp. 461–475.

Baschlin, C. F. (1948). "Lehrbuch der Geodasie". In: *Verlag Orell Fussli, Zurich*.

Bea, F. et al. (2011). "SHRIMP dating and Nd isotope geology of the Archean terranes of the Uweinat-Kamil inlier, Egypt–Sudan–Libya". In: *Precambrian Research* 189.3, pp. 328 –346. ISSN: 0301-9268. DOI: https://doi.org/10.1016/j.precamres.2011.07.017. URL: http://www.sciencedirect.com/science/article/pii/S0301926811001525.

Begg, G. C. et al. (2009). "The lithospheric architecture of Africa: Seismic tomography, mantle petrology, and tectonic evolution". In: *Geosphere* 5.1, pp. 23–50.

Black, R. and J.-P. Liégeois (1993). "Cratons, mobile belts, alkaline rocks and continental lithospheric mantle: the Pan-African testimony". In: *Journal of the Geological Society* 150.1, pp. 89–98. ISSN: 0016-7649. DOI: 10.1144/gsjgs.150.1.0088. eprint: http://jgs.lyellcollection.org/content/150/1/89.full.pdf. URL: http://jgs.lyellcollection.org/content/150/1/89.

Bouman, J. et al. (2015). "GOCE gravity gradient data for lithospheric modeling". In: *INT J APPL EARTH OBS* 35. GOCE earth science applications and models(Based on the ESA GOCE solid earth workshop, 16-17 October 2012), pp. 16 –30. ISSN: 0303-2434. DOI: https://doi.org/10.1016/j.jag.2013.11.001. URL: http://www.sciencedirect.com/science/article/pii/S0303243413001487.

Bouman, J. et al. (2016). "Satellite gravity gradient grids for Geophysics". In: *Scientific reports* 6, p. 21050.

Bowin, C. (2000). "Mass anomalies and the structure of the earth". In: *Physics and Chemistry of the Earth, Part A: Solid Earth and Geodesy* 25.4, pp. 343 –353. ISSN: 1464-1895. DOI: https://doi.org/10.1016/S1464-1895(00)00056-9. URL: http://www.sciencedirect.com/science/article/pii/S1464189500000569.

Braitenberg, C. et al. (2016). "Gravity for Detecting Caves: Airborne and Terrestrial Simulations Based on a Comprehensive Karstic Cave Benchmark". In: *PURE APPL GEOPHYS* 173.4, pp. 1243–1264. ISSN: 1420-9136. DOI: https://doi.org/10.1007/s00024-015-1182-y. URL: https://doi.org/10.1007/s00024-015-1182-y.

Brito Neves, B. B. de and R. A. Fuck (2014). "The basement of the South American platform: Half Laurentian (N-NW)+half Gondwanan (E-SE) domains". In: *Precambrian Research* 244. Precambrian Supercontinents, pp. 75 –86. ISSN: 0301-9268. DOI: https://doi.org/10.1016/j.precamres.2013.09.020. URL: http://www.sciencedirect.com/science/article/pii/S030192681300288X.

Bruinsma, S. L. et al. (2013). "The new ESA satellite-only gravity field model via the direct approach". In: *Geophysical Research Letters* 40.14, pp. 3607–3612.

Bruinsma, S. L. et al. (2014). "EIGEN-6C4 The latest combined global gravity field model including GOCE data up to degree and order 2190 of GFZ Potsdam and GRGS Toulouse". In: *GFZ Data Services* 10.

Burke, K. (1996). "The African plate". In: *South african journal of geology* 99.4, pp. 341–409.

Burke, K. and J. T. Wilson (1976). "Hot spots on the Earth's surface". In: *Scientific American* 235.2, pp. 46–59.

Capponi, M., A. H. Mansi, and D. Sampietro (2018). "Improving the computation of the gravitational terrain effect close to ground stations in the GTE software". In: *STUD GEOPHYS GEOD* 62.2, pp. 206–222. ISSN: 1573-1626. DOI: https://doi.

org/10.1007/s11200-017-0814-3. URL: https://doi.org/10.1007/s11200-017-0814-3.

Christensen, N. I. and W. D. Mooney (1995). "Seismic velocity structure and composition of the continental crust: A global view". In: *J GEOPHYS RES-SOL EA* 100.B6, pp. 9761–9788. DOI: https://doi.org/10.1029/95JB00259. eprint: https://agupubs.onlinelibrary.wiley.com/doi/pdf/10.1029/95JB00259. URL: https://agupubs.onlinelibrary.wiley.com/doi/abs/10.1029/95JB00259.

Connolly, J. A. D. (2005). "Computation of phase equilibria by linear programming: A tool for geodynamic modeling and its application to subduction zone decarbonation". In: *Earth and Planetary Science Letters* 236.1, pp. 524 –541. ISSN: 0012-821X. DOI: https://doi.org/10.1016/j.epsl.2005.04.033. URL: http://www.sciencedirect.com/science/article/pii/S0012821X05002839.

Connolly, J. A. D. and D. M. Kerrick (2002). "Metamorphic controls on seismic velocity of subducted oceanic crust at 100–250 km depth". In: *Earth and Planetary Science Letters* 204.1, pp. 61 –74. ISSN: 0012-821X. DOI: https://doi.org/10.1016/S0012-821X(02)00957-3. URL: http://www.sciencedirect.com/science/article/pii/S0012821X02009573.

Cooper, C. M. and M. S. Miller (2014). "Craton formation: Internal structure inherited from closing of the early oceans". In: *Lithosphere* 6.1, pp. 35–42.

Corchete, V. et al. (2017). "Crustal and upper mantle structure of the north-east of Egypt and the Afro-Arabian plate boundary region from Rayleigh-wave analysis". In: *J AFR EARTH SCI* 129, pp. 195 –201. ISSN: 1464-343X. DOI: https://doi.org/10.1016/j.jafrearsci.2017.01.011. URL: http://www.sciencedirect.com/science/article/pii/S1464343X17300122.

Dave, R. and A. Li (2016). "Destruction of the Wyoming craton: Seismic evidence and geodynamic processes". In: *Geology* 44.11, pp. 883–886.

Dawod, G. M. (2008). "Towards the redefinition of the Egyptian geoid: Performance analysis of recent global geoid and digital terrain models". In: *Journal of Spatial Science* 53.1, pp. 31–42.

Djomani, Y. H. Poudjom et al. (2001). "The density structure of subcontinental lithosphere through time". In: *Earth and Planetary Science Letters* 184.3, pp. 605 –621. ISSN: 0012-821X. DOI: https://doi.org/10.1016/S0012-821X(00)00362-9. URL: http://www.sciencedirect.com/science/article/pii/S0012821X00003629.

Dorre, A. S. et al. (1997). "Crustal thickness of Egypt determined by gravity data". In: *J AFR EARTH SCI* 25.3, pp. 425 –434. ISSN: 1464-343X. DOI: https://doi.org/10.1016/S0899-5362(97)00114-0. URL: http://www.sciencedirect.com/science/article/pii/S0899536297001140.

Drinkwater, M. R. et al. (2003). "VII: CLOSING SESSION: GOCE: ESA's First Earth Explorer Core Mission". In: *Space Science Reviews* 108.1, pp. 419–432. ISSN: 1572-9672. DOI: 10.1023/A:1026104216284. URL: https://doi.org/10.1023/A:1026104216284.

Ebinger, C. J and N. H. Sleep (1998). "Cenozoic magmatism throughout east Africa resulting from impact of a single plume". In: *Nature* 395.6704, p. 788.

EL-Hadidy, S. (1995). "Crustal Structure and its Related Causative Tectonics in Northern Egypt using Geophysical Data, Egypt". PhD thesis. Ain Shans University.

El-Isa, Z. et al. (1987). "A crustal structure study of Jordan derived from seismic refraction data". In: *TECTONOPHYSICS* 138.2, pp. 235 –253. ISSN: 0040-1951. DOI:

https://doi.org/10.1016/0040-1951(87)90042-4. URL: http://www.sciencedirect.com/science/article/pii/0040195187900424.

El-Khrepy, S. (2008). "Detailed Study of the Seismic Waves Velocity and Attenuation Models Using Local Earthquakes in the Northeastern Part of Egypt, Mansoura, Egypt". PhD thesis. Mansoura University.

El-Khrepy, S. A. F. (2001). "Tomographic Modeling of Dahshour Area Local Earthquakes, Northern Egypt". In: *M.Sc. thesis, Ain Shams University*.

Emry, E. L. et al. (2019). "Upper Mantle Earth Structure in Africa From Full-Wave Ambient Noise Tomography". In: *Geochemistry, Geophysics, Geosystems* 0.0. DOI: 10.1029/2018GC007804. eprint: https://agupubs.onlinelibrary.wiley.com/doi/pdf/10.1029/2018GC007804. URL: https://agupubs.onlinelibrary.wiley.com/doi/abs/10.1029/2018GC007804.

Eriksson, P. G. et al. (2009). "A Kaapvaal craton debate: Nucleus of an early small supercontinent or affected by an enhanced accretion event?" In: *Gondwana Research* 15.3. Special Issue: Supercontinent Dynamics, pp. 354 –372. ISSN: 1342-937X. DOI: https://doi.org/10.1016/j.gr.2008.08.001. URL: http://www.sciencedirect.com/science/article/pii/S1342937X08001421.

Exxon (1985). "Tectonic Map Series of the World". In: *Exxon Production Research Company, Houston, TX, USA*.

Fairhead, J. D. (1979). "A gravity link between the domally uplifted Cainozoic volcanic centres of North Africa and its similarity to the East African Rift System anomaly". In: *Earth and Planetary Science Letters* 42.1, pp. 109 –113. ISSN: 0012-821X. DOI: https://doi.org/10.1016/0012-821X(79)90195-X. URL: http://www.sciencedirect.com/science/article/pii/0012821X7990195X.

Fairhead, J. D. et al. (1988). "African gravity project". In: *GETECH, Department of Earth Sciences, University of Leeds*.

Farr, T. G. et al. (2007). "The shuttle radar topography mission". In: *Reviews of geophysics* 45.2.

Fezaa, A. et al. (2010). "Late Ediacaran geological evolution (575–555Ma) of the Djanet Terrane, Eastern Hoggar, Algeria, evidence for a Murzukian intracontinental episode". In: *Precambrian Research* 180.3, pp. 299 –327. ISSN: 0301-9268. DOI: https://doi.org/10.1016/j.precamres.2010.05.011. URL: http://www.sciencedirect.com/science/article/pii/S0301926810001257.

Fischer, K. M. et al. (2010). "The Lithosphere-Asthenosphere Boundary". In: *Annual Review of Earth and Planetary Sciences* 38.1, pp. 551–575. DOI: 10.1146/annurev-earth-040809-152438. eprint: https://doi.org/10.1146/annurev-earth-040809-152438. URL: https://doi.org/10.1146/annurev-earth-040809-152438.

Fishwick, S. (2010). "Surface wave tomography: Imaging of the lithosphere–asthenosphere boundary beneath central and southern Africa?" In: *Lithos* 120.1. The lithosphere/asthenosphere boundary: Nature, formation and evolution, pp. 63 –73. ISSN: 0024-4937. DOI: https://doi.org/10.1016/j.lithos.2010.05.011. URL: http://www.sciencedirect.com/science/article/pii/S0024493710001453.

Fishwick, S. and I. D. Bastow (2011). "Towards a better understanding of African topography: a review of passive-source seismic studies of the African crust and upper mantle". In: *Geological Society, London, Special Publications* 357.1, pp. 343–371. ISSN: 0305-8719. DOI: 10.1144/SP357.19. eprint: http://sp.lyellcollection.org/content/357/1/343.full.pdf. URL: http://sp.lyellcollection.org/content/357/1/343.

Forsberg, R. (1984). *A study of terrain reductions, density anomalies and geophysical inversion methods in gravity field modelling*. Tech. rep. OHIO STATE UNIV COLUMBUS DEPT OF GEODETIC SCIENCE and SURVEYING.

Föster, D. A. et al. (2006). "Proterozoic evolution of the western margin of the Wyoming craton: implications for the tectonic and magmatic evolution of the northern Rocky Mountains". In: *Canadian Journal of Earth Sciences* 43.10, pp. 1601–1619. DOI: 10.1139/e06-052. eprint: https://doi.org/10.1139/e06-052. URL: https://doi.org/10.1139/e06-052.

Fullea, J. et al. (2009). "LitMod3D: An interactive 3-D software to model the thermal, compositional, density, seismological, and rheological structure of the lithosphere and sublithospheric upper mantle". In: *Geochemistry, Geophysics, Geosystems* 10.8. DOI: 10.1029/2009GC002391. eprint: https://agupubs.onlinelibrary.wiley.com/doi/pdf/10.1029/2009GC002391. URL: https://agupubs.onlinelibrary.wiley.com/doi/abs/10.1029/2009GC002391.

Ganade, C. E. et al. (2016). "Tightening-up NE Brazil and NW Africa connections: New U–Pb/Lu–Hf zircon data of a complete plate tectonic cycle in the Dahomey belt of the West Gondwana Orogen in Togo and Benin". In: *Precambrian Research* 276, pp. 24 –42. ISSN: 0301-9268. DOI: https://doi.org/10.1016/j.precamres.2016.01.032. URL: http://www.sciencedirect.com/science/article/pii/S030192681600053X.

Gatti, A., M. Reguzzoni, and G. Venuti (2013). "The height datum problem and the role of satellite gravity models". In: *Journal of Geodesy* 87.1, pp. 15–22.

Gatti, A. et al. (2016). "Computation and assessment of the fifth release of the GOCE-only space-wise solution". In: *The 1st Joint Commission 2 and IGFS Meeting*. DOI: 10.13140/RG.2.2.28625.94569.

Gaulier, J. M. et al. (1988). "Seismic study of the crust of the northern Red Sea and Gulf of Suez". In: *TECTONOPHYSICS* 153.1. The gulf of Suez and red sea rifting, pp. 55 –88. ISSN: 0040-1951. DOI: https://doi.org/10.1016/0040-1951(88)90007-8. URL: http://www.sciencedirect.com/science/article/pii/0040195188900078.

Gilardoni, M., M. Reguzzoni, and D. Sampietro (2012). "A least-squares collocation procedure to merge local geoids with the aid of satellite-only global gravity models: the Italian-Swiss geoid case study". In: *EGU General Assembly Conference Abstracts*. Vol. 14, p. 8061.

— (2016). "GECO: a global gravity model by locally combining GOCE data and EGM2008". In: *Studia Geophysica et Geodaetica* 60.2, pp. 228–247.

Ginzburg, A. and Z. Ben-Avraham (1987). "The deep structure of the central and southern Levant continental margin". In: *Annales Tectonicae*. Vol. 1. 2, pp. 105–115.

Ginzburg, A. et al. (1981). "The structure of the crust and upper mantle in the Dead Sea rift". In: *TECTONOPHYSICS* 80.1. The Dead Sea Rift, pp. 109 –119. ISSN: 0040-1951. DOI: https://doi.org/10.1016/0040-1951(81)90144-X. URL: http://www.sciencedirect.com/science/article/pii/004019518190144X.

Girdler, R. W. (1975). "The great negative Bouguer gravity anomaly over Africa". In: *Eos, Transactions American Geophysical Union* 56.8, pp. 516–519. DOI: 10.1029/EO056i008p00516. eprint: https://agupubs.onlinelibrary.wiley.com/doi/pdf/10.1029/EO056i008p00516. URL: https://agupubs.onlinelibrary.wiley.com/doi/abs/10.1029/EO056i008p00516.

Globig, J. et al. (2016a). "New insights into the crust and lithospheric mantle structure of Africa from elevation, geoid, and thermal analysis". In: *J GEOPHYS RES-SOL EA* 121.7, pp. 5389–5424. DOI: https://doi.org/10.1002/2016JB012972. eprint: https://agupubs.onlinelibrary.wiley.com/doi/pdf/10.1002/2016JB012972. URL: https://agupubs.onlinelibrary.wiley.com/doi/abs/10.1002/2016JB012972.

Globig, J. et al. (2016b). "New insights into the crust and lithospheric mantle structure of Africa from elevation, geoid, and thermal analysis". In: *Journal of Geophysical Research: Solid Earth* 121.7, pp. 5389–5424. DOI: 10.1002/2016JB012972. eprint: https://agupubs.onlinelibrary.wiley.com/doi/pdf/10.1002/2016JB012972. URL: https://agupubs.onlinelibrary.wiley.com/doi/abs/10.1002/2016JB012972.

GOCE, H. P. F. (2010). *GOCE Level 2 Product Data Handbook*. Tech. rep. Technical Report GO-MAHPF-GS-0110, GOCE High Level Processing Facility.

Godah, W. and J. Krynski (2015). "Comparison of GGMs based on one year GOCE observations with the EGM08 and terrestrial data over the area of Sudan". In: *International Journal of Applied Earth Observation and Geoinformation* 35, pp. 128–135.

Götze, H.-J. (2020). "Potential Methods and Geoinformation Systems". In: *Handbook of Geomathematics*. Ed. by W. Freeden, M.Z. Nashed, and T. Sonar. Berlin, Heidelberg: Springer Berlin Heidelberg, pp. 1–21. ISBN: 978-3-642-27793-1. DOI: https://doi.org/10.1007/978-3-642-27793-1_52-2. URL: https://doi.org/10.1007/978-3-642-27793-1_52-2.

Götze, H.-J. and B. Lahmeyer (1988). "Application of three-dimensional interactive modeling in gravity and magnetics". In: *Geophysics* 53.8, pp. 1096–1108.

Götze, H.-J. and B. Lahmeyer (1988). "Application of three-dimensional interactive modeling in gravity and magnetics". In: *Geophysics* 53.8, pp. 1096–1108. DOI: https://doi.org/10.1190/1.1442546. eprint: https://doi.org/10.1190/1.1442546. URL: https://doi.org/10.1190/1.1442546.

Grad, M., T. Tiira, and ESC Working Group (2009). "The Moho depth map of the European Plate". In: *Geophysical Journal International* 176.1, pp. 279–292. ISSN: 0956-540X. DOI: 10.1111/j.1365-246X.2008.03919.x. eprint: http://oup.prod.sis.lan/gji/article-pdf/176/1/279/5923435/176-1-279.pdf. URL: https://dx.doi.org/10.1111/j.1365-246X.2008.03919.x.

Grand, S. P. (2002). "Mantle shear–wave tomography and the fate of subducted slabs". In: *Philosophical Transactions of the Royal Society of London A: Mathematical, Physical and Engineering Sciences* 360.1800, pp. 2475–2491.

Gray, D. R et al. (2008). "A Damara orogen perspective on the assembly of southwestern Gondwana". In: *Geological Society, London, Special Publications* 294.1, pp. 257–278.

Griffin, W. L. et al. (1999). "The Siberian lithosphere traverse: mantle terranes and the assembly of the Siberian Craton". In: *Tectonophysics* 310.1, pp. 1 –35. ISSN: 0040-1951. DOI: https://doi.org/10.1016/S0040-1951(99)00156-0. URL: http://www.sciencedirect.com/science/article/pii/S0040195199001560.

Griffin, W. L. et al. (2003). "The origin and evolution of Archean lithospheric mantle". In: *Precambrian Research* 127.1. Archaean Tectonics, Volume 1, pp. 19 –41. ISSN: 0301-9268. DOI: https://doi.org/10.1016/S0301-9268(03)00180-3. URL: http://www.sciencedirect.com/science/article/pii/S0301926803001803.

Griffin, W. L. et al. (2004). "Lithosphere mapping beneath the North American plate". In: *Lithos* 77.1. Selected Papers from the Eighth International Kimberlite Conference. Volume 2: The J. Barry Hawthorne Volume, pp. 873 –922. ISSN: 0024-4937. DOI: https://doi.org/10.1016/j.lithos.2004.03.034. URL: http://www.sciencedirect.com/science/article/pii/S002449370400088X.

Griffin, W. L. et al. (2008). "The Composition and Evolution of Lithospheric Mantle: a Re-evaluation and its Tectonic Implications". In: *Journal of Petrology* 50.7, pp. 1185–1204. ISSN: 0022-3530. DOI: 10.1093/petrology/egn033. eprint: http://oup.prod.sis.lan/petrology/article-pdf/50/7/1185/4345721/egn033.pdf. URL: https://dx.doi.org/10.1093/petrology/egn033.

Guy, A., N. Holzrichter, and J. Ebbing (2017). "Moho depth model for the Central Asian Orogenic Belt from satellite gravity gradients". In: *Journal of Geophysical Research: Solid Earth* 122.9, pp. 7388–7407. DOI: 10.1002/2017JB014120. eprint: https://agupubs.onlinelibrary.wiley.com/doi/pdf/10.1002/2017JB014120. URL: https://agupubs.onlinelibrary.wiley.com/doi/abs/10.1002/2017JB014120.

Hackney, R.I. and W.E. Featherstone (2003). "Geodetic versus geophysical perspectives of the 'gravity anomaly'". In: *GEOPHYS J INT* 154.1, pp. 35–43. DOI: https://doi.org/10.1046/j.1365-246X.2003.01941.x. URL: http://dx.doi.org/10.1046/j.1365-246X.2003.01941.x.

Hanafy, M. S. and M. A. El Tokhey (1993). "Simulation studies for improving the geoid in Egypt". In: *Geodesy and Physics of the Earth*. Springer, pp. 153–158.

Hansen, S. E. et al. (2013). "Investigating the P wave velocity structure beneath Harrat Lunayyir, northwestern Saudi Arabia, using double-difference tomography and earthquakes from the 2009 seismic swarm". In: *Journal of Geophysical Research: Solid Earth* 118.9, pp. 4814–4826. DOI: 10.1002/jgrb.50286. eprint: https://agupubs.onlinelibrary.wiley.com/doi/pdf/10.1002/jgrb.50286. URL: https://agupubs.onlinelibrary.wiley.com/doi/abs/10.1002/jgrb.50286.

Hantschel, T. and A. I. Kauerauf (2009). *Fundamentals of basin and petroleum systems modeling*. Springer Science & Business Media.

Harris, N. B. W., C. J. Hawkesworth, and A. C. Ries (1984). "Crustal evolution in north-east and east Africa from model Nd ages". In: *Nature* 309.5971, p. 773.

Heine, C. et al. (2008). "Subsidence in intracontinental basins due to dynamic topography". In: *Physics of the Earth and Planetary Interiors* 171.1. Recent Advances in Computational Geodynamics: Theory, Numerics and Applications, pp. 252 –264. ISSN: 0031-9201. DOI: https://doi.org/10.1016/j.pepi.2008.05.008. URL: http://www.sciencedirect.com/science/article/pii/S0031920108001040.

Henry, B. et al. (2009). "Repeated granitoid intrusions during the Neoproterozoic along the western boundary of the Saharan metacraton, Eastern Hoggar, Tuareg shield, Algeria: An AMS and U–Pb zircon age study". In: *Tectonophysics* 474.3, pp. 417 –434. ISSN: 0040-1951. DOI: https://doi.org/10.1016/j.tecto.2009.04.022. URL: http://www.sciencedirect.com/science/article/pii/S0040195109002339.

Hinze., W. J. et al. (2005). "New standards for reducing gravity data: The North American gravity database". In: *Geophysics* 70.4, J25–J32. DOI: https://doi.org/10.1190/1.1988183. eprint: https://doi.org/10.1190/1.1988183. URL: https://doi.org/10.1190/1.1988183.

Holt, P. J. et al. (2010). "Lithospheric cooling and thickening as a basin forming mechanism". In: *Tectonophysics* 495.3, pp. 184 –194. ISSN: 0040-1951. DOI: https://doi.

org/10.1016/j.tecto.2010.09.014. URL: http://www.sciencedirect.com/science/article/pii/S0040195110003641.

Holzrichter, N., W. Szwillus, and J. Ebbing (2016). "Importance of far-field topographic and isostatic corrections for regional density modelling". In: *Geophysical Journal International* 207.1, pp. 274–287. ISSN: 0956-540X. DOI: 10.1093/gji/ggw270. eprint: http://oup.prod.sis.lan/gji/article-pdf/207/1/274/7966944/ggw270.pdf. URL: https://dx.doi.org/10.1093/gji/ggw270.

Hosny, A. and A. Nyblade (2014). "Crustal structure in southeastern Egypt: Symmetric thinning of the northern Red Sea rifted margins". In: *GEOLOGY* 42.3, p. 219. DOI: https://doi.org/10.1130/G34726.1. URL: http://dx.doi.org/10.1130/G34726.1.

— (2016). "The crustal structure of Egypt and the northern Red Sea region". In: *TECTONOPHYSICS* 687, pp. 257 –267. ISSN: 0040-1951. DOI: https://doi.org/10.1016/j.tecto.2016.06.003. URL: http://www.sciencedirect.com/science/article/pii/S0040195116302104.

Jacobs, J. A., R. D.. Russell, and J. T. Wilson (1959). *Physics and GEOLOGY*. McGraw-Hill Book Co., New York.

Kaban, M. K. et al. (2016). "3D density model of the upper mantle of Asia based on inversion of gravity and seismic tomography data". In: *GEOCHEM GEOPHY GEOSY* 17.11, pp. 4457–4477. DOI: https://doi.org/10.1002/2016GC006458. eprint: https://agupubs.onlinelibrary.wiley.com/doi/pdf/10.1002/2016GC006458. URL: https://agupubs.onlinelibrary.wiley.com/doi/abs/10.1002/2016GC006458.

Kaula, W. M. (1966). "Theory of satellite geodesy, Blaisdell Publ". In: *Co., Waltham, Mass*.

Klerkx, J. and S. Deutsch (1977). "Resultats preliminaires obtenus par la methode Rb/Sr sur l'age des formations Precambriennes de la region d'Uweinat (Libye)". In: *Musee Royal de l'Afrique Centrale. Déepartement Géeologie Minéeralogie Rapport Annuel*, pp. 83–94.

Knapmeyer-Endrun, B., F. Krüger, and T. P. W. Group (2014). "Moho depth across the Trans-European Suture Zone from P- and S-receiver functions". In: *GEOPHYS J INT* 197.2, pp. 1048–1075. DOI: https://doi.org/10.1093/gji/ggu035. URL: http://dx.doi.org/10.1093/gji/ggu035.

Knudsen, P. (1987). "Estimation and modelling of the local empirical covariance function using gravity and satellite altimeter data". In: *Bulletin Geodesique* 61.2, pp. 145–160.

Kobussen, A. F. et al. (2008). "Ghosts of lithospheres past: Imaging an evolving lithospheric mantle in southern Africa". In: *Geology* 36.7, pp. 515–518.

Krarup, T. (1969). "A contribution to the mathematical foundation of physical geodesy." In: *Geod. Inst. Copenhagen, Medd., No. 44, 80 p.* 44.

Kreh, M. (2012). "Bessel functions". In: *Lecture Notes, Penn State-Göttingen Summer School on Number Theory* 82.

Kröner, A. and R. J. Stern (2005). "AFRICA | Pan-African orogeny". In: *Encyclopedia of geology*. Ed. by R.C. Selley. London: Elsevier Academic, pp. 1–12.

Kusky, T. M. et al. (2014). "Flat slab subduction, trench suction, and craton destruction: Comparison of the North China, Wyoming, and Brazilian cratons". In: *Tectonophysics* 630, pp. 208 –221. ISSN: 0040-1951. DOI: https://doi.org/10.1016/j.tecto.2014.05.028. URL: http://www.sciencedirect.com/science/article/pii/S0040195114003011.

LaFehr, T. R. (1991). "An exact solution for the gravity curvature (Bullard B) correction". In: *Geophysics* 56.8, pp. 1179–1184. DOI: https://doi.org/10.1190/1.1443138. eprint: https://doi.org/10.1190/1.1443138. URL: https://doi.org/10.1190/1.1443138.

Laske, G. (1997). "A global digital map of sediment thickness". In: *EOS TRANS AM GEOPHYS UNION* 78, F483.

Laske, G. et al. (2013). "Update on CRUST1. 0—A 1-degree global model of Earth's crust". In: *GEOPHYS RES ABSTR*. Vol. 15, p. 2658.

Lemnifi, A. A. et al. (2017). "Crustal Thickness Beneath Libya and the Origin of Partial Melt Beneath AS Sawda Volcanic Province From Receiver Function Constraints". In: *Journal of Geophysical Research: Solid Earth* 122.12, pp. 10,037–10,051. DOI: 10.1002/2017JB014291. eprint: https://agupubs.onlinelibrary.wiley.com/doi/pdf/10.1002/2017JB014291. URL: https://agupubs.onlinelibrary.wiley.com/doi/abs/10.1002/2017JB014291.

Lesquer, A. et al. (1990). "Geophysical and petrological evidence for the presence of an "anomalous" upper mantle beneath the Sahara basins (Algeria)". In: *Earth and Planetary Science Letters* 96.3, pp. 407 –418. ISSN: 0012-821X. DOI: https://doi.org/10.1016/0012-821X(90)90016-Q. URL: http://www.sciencedirect.com/science/article/pii/0012821X9090016Q.

Li, X. and H.-J. Götze (2001). "Ellipsoid, geoid, gravity, geodesy, and geophysics". In: *Geophysics* 66.6, pp. 1660–1668. DOI: https://doi.org/10.1190/1.1487109. eprint: https://doi.org/10.1190/1.1487109. URL: https://doi.org/10.1190/1.1487109.

Liégeois, J.-P. et al. (1994). "Early and late Pan-African orogenies in the Aïr assembly of terranes (Tuareg shield, Niger)". In: *Precambrian Research* 67.1, pp. 59 –88. ISSN: 0301-9268. DOI: https://doi.org/10.1016/0301-9268(94)90005-1. URL: http://www.sciencedirect.com/science/article/pii/0301926894900051.

Liégeois, J.-P. et al. (2003). "The LATEA metacraton (Central Hoggar, Tuareg shield, Algeria): behaviour of an old passive margin during the Pan-African orogeny". In: *Journal of African Earth Sciences* 37.3. The Precambrian of Hoggar, Tuareg Shield-Dedicated to Louis Latouche, pp. 161 –190. ISSN: 1464-343X. DOI: https://doi.org/10.1016/j.jafrearsci.2003.05.004. URL: http://www.sciencedirect.com/science/article/pii/S0899536203000988.

Liégeois, J.-P. et al. (2013). "Metacraton: Nature, genesis and behavior". In: *Gondwana Research* 23.1. Construction and Destruction of Cratons, pp. 220 –237. ISSN: 1342-937X. DOI: https://doi.org/10.1016/j.gr.2012.02.016. URL: http://www.sciencedirect.com/science/article/pii/S1342937X12000573.

Liégeois, J.-P. et al. (2005). "The Hoggar swell and volcanism: Reactivation of the Precambrian Tuareg shield during Alpine convergence and West African Cenozoic volcanism". In: *Plates, plumes and paradigms*. Geological Society of America. DOI: 10.1130/0-8137-2388-4.379. URL: https://dx.doi.org/10.1130/0-8137-2388-4.379.

Lithgow-Bertelloni, C. and L. Stixrude (2011). "Thermodynamics of mantle minerals - II. Phase equilibria". In: *Geophysical Journal International* 184.3, pp. 1180–1213. ISSN: 0956-540X. DOI: 10.1111/j.1365-246X.2010.04890.x. eprint: http://oup.prod.sis.lan/gji/article-pdf/184/3/1180/27638878/184-3-1180.pdf. URL: https://dx.doi.org/10.1111/j.1365-246X.2010.04890.x.

Makris, J. (1983). "Crustal structure at the northwestern region of the Arabian shield and its transition to the Red Sea". In: *Bulletin of the Faculty of Earth Sciences, King Abdulaziz University* 6, pp. 435–447.

Makris, J. and R. Rihm (1991). "Shear-controlled evolution of the Red Sea: pull apart model". In: *TECTONOPHYSICS* 198.2. Red Sea: Birth and Early History of a New Oceanic Basin, pp. 441 –466. ISSN: 0040-1951. DOI: https://doi.org/10.1016/0040-1951(91)90166-P. URL: http://www.sciencedirect.com/science/article/pii/004019519190166P.

Makris, J., R. Rihm, and A. Allam (1988). "Some geophysical aspects of the evolution and structure of the crust in Egypt". In: *The Pan-African Belt of Northeast Africa and Adjacent Area: Tectonic Evolution and Economic Aspects of a Late Proterozoic Orogen*, pp. 345–369.

Makris, J. et al. (1979). "Deep seismic sounding in Egypt, Part I: The Mediterranean Sea between Crete, Sidi Barani, and the coastal area of Egypt". In: *Unpublished report, National Research Institute of Astronomy and Geophysics, Helwan, Egypt*.

Makris, J. et al. (1982). *Deep Seismic Soundings in Egypt, Part 1: The Mediterranean Sea between Crete-Sidi Barrani and the coastal areas of Egypt*. Tech. rep. Technical Report University of Hamburg, FRG.

Makris, J. et al. (1991). "The gravity field of the Red Sea and East Africa". In: *TECTONOPHYSICS* 198.2. Red Sea: Birth and Early History of a New Oceanic Basin, pp. 369 –381. ISSN: 0040-1951. DOI: https://doi.org/10.1016/0040-1951(91)90161-K. URL: http://www.sciencedirect.com/science/article/pii/004019519190161K.

Makris, J. et al. (1994). *Geological structure of the Northeastern Mediterranean:(Cruise 5 of the Research Vessel Akademik Nikolaj Strakhov)*. Geologicheskii Institut Akademiia Nauk Sssr, pp. 87–98.

Mansi, A. H. (2016). "Airborne gravity field modelling". PhD thesis. Politecnico di Milano. URL: https://www.politesi.polimi.it/handle/10589/116547.

Mansi, A. H., M. Capponi, and D. Sampietro (2018). "Downward continuation of airborne gravity data by means of the change of boundary approach". In: *PURE APPL GEOPHYS* 175.3, pp. 977–988. ISSN: 1420-9136. DOI: https://doi.org/10.1007/s00024-017-1717-5. URL: https://doi.org/10.1007/s00024-017-1717-5.

Marzouk, I. (1988). "Crustal structure of Egypt deduced from deep seismic and gravity data". In: *Ph.D. dissertation, Univ. of Hamburg* 118.

Mayer-Güerr, T. (2015). "The combined satellite gravity field model GOCO05s". In: *EGU general assembly conference abstracts*. Vol. 17.

McDonough, W.F. and S. s. Sun (1995). "The composition of the Earth". In: *Chemical Geology* 120.3. Chemical Evolution of the Mantle, pp. 223 –253. ISSN: 0009-2541. DOI: https://doi.org/10.1016/0009-2541(94)00140-4. URL: http://www.sciencedirect.com/science/article/pii/0009254194001404.

Mechie, J. et al. (2005). "Crustal shear velocity structure across the Dead Sea Transform from two-dimensional modelling of DESERT project explosion seismic data". In: *GEOPHYS J INT* 160.3, pp. 910–924. DOI: https://doi.org/10.1111/j.1365-246X.2005.02526.x. URL: http://dx.doi.org/10.1111/j.1365-246X.2005.02526.x.

Meert, J. G. and B. S. Lieberman (2008). "The Neoproterozoic assembly of Gondwana and its relationship to the Ediacaran–Cambrian radiation". In: *Gondwana Research* 14.1. Snowball Earth to Cambrian Explosion, pp. 5 –21. ISSN: 1342-937X.

DOI: https://doi.org/10.1016/j.gr.2007.06.007. URL: http://www.sciencedirect.com/science/article/pii/S1342937X07001360.

Mikuška, J., R. Pašteka, and I. Marušiak (2006). "Estimation of distant relief effect in gravimetry". In: *Geophysics* 71.6, J59–J69. DOI: https://doi.org/10.1190/1.2338333. eprint: https://doi.org/10.1190/1.2338333. URL: https://doi.org/10.1190/1.2338333.

Moritz, H. (1972). *Advanced least-squares methods*. Vol. 175. Ohio State University Research Foundation.

— (1978). "Least-squares collocation". In: *Reviews of geophysics* 16.3, pp. 421–430.

— (1980). "Advanced physical geodesy". In: *Advances in Planetary Geology*.

— (1989). "Advanced physical geodesy 2nd edn". In: *Wichmann, Karlsruhe*.

Naudy, H. and R. Neumann (1965). "Sur la définition de l'anomalie de Bouguer et ses conséquences pratiques". In: *GEOPHYS PROSPECT* 13.1, pp. 1–11.

Ngalamo, J. F. Goussi et al. (2017). "Geophysical imaging of metacratonizaton in the northern edge of the Congo craton in Cameroon". In: *Journal of African Earth Sciences* 129, pp. 94 –107. ISSN: 1464-343X. DOI: https://doi.org/10.1016/j.jafrearsci.2016.12.010. URL: http://www.sciencedirect.com/science/article/pii/S1464343X16304174.

Nyblade, A. A. et al. (1996). "Terrestrial heat flow in the Sirt Basin, Libya, and the pattern of heat flow across northern Africa". In: *J. Geophys. Res* 101.B8, pp. 17737–17746.

O'Reilly, S. Y. and W. L. Griffin (2006). "Imaging global chemical and thermal heterogeneity in the subcontinental lithospheric mantle with garnets and xenoliths: Geophysical implications". In: *Tectonophysics* 416.1. The Heterogeneous Mantle, pp. 289 –309. ISSN: 0040-1951. DOI: https://doi.org/10.1016/j.tecto.2005.11.014. URL: http://www.sciencedirect.com/science/article/pii/S0040195105006013.

Pail, R. et al. (2010). "GOCE gravity field model derived from orbit and gradiometry data applying the time-wise method". In: *Proceedings of the ESA Living Planet Symposium, ESA Publication SP-686*.

Pail, R. et al. (2011). "First GOCE gravity field models derived by three different approaches". In: *Journal of Geodesy* 85.11, p. 819.

Pail, R. et al. (2016). "The experimental gravity field model XGM2016". In: *International Symposium on Gravity, Geoid and Height System 2016-1st Joint Commission 2 and IGFS Meeting*.

Pavlis, N. K. et al. (2008). "An earth gravitational model to degree 2160: EGM2008". In: *EGU General Assembly* 10, pp. 13–18.

Pik, R., B. Marty, and D. R. Hilton (2006). "How many mantle plumes in Africa? The geochemical point of view". In: *Chemical Geology* 226.3. Special Issue in Honour of R.K. O'Nions, pp. 100 –114. ISSN: 0009-2541. DOI: https://doi.org/10.1016/j.chemgeo.2005.09.016. URL: http://www.sciencedirect.com/science/article/pii/S0009254105004225.

Pin, C. and J. L. Poidevin (1987). "U-Pb zircon evidence for a pan-african granulite facies metamorphism in the central african republic. a new interpretation of the high-grade series of the northern border of the congo craton". In: *Precambrian Research* 36.3, pp. 303 –312. ISSN: 0301-9268. DOI: https://doi.org/10.1016/0301-9268(87)90027-1. URL: http://www.sciencedirect.com/science/article/pii/0301926887900271.

Pollack, H. N., S. J. Hurter, and J. R. Johnson (1993). "Heat flow from the Earth's interior: Analysis of the global data set". In: *Reviews of Geophysics* 31.3, pp. 267–280. DOI: 10.1029/93RG01249. eprint: https://agupubs.onlinelibrary.wiley.com/doi/pdf/10.1029/93RG01249. URL: https://agupubs.onlinelibrary.wiley.com/doi/abs/10.1029/93RG01249.

Prodehl, C. and J. Mechie (1991). "Crustal thinning in relationship to the evolution of the Afro-Arabian rift system: a review of seismic-refraction data". In: *TECTONOPHYSICS* 198.2. Red Sea: Birth and Early History of a New Oceanic Basin, pp. 311 –327. ISSN: 0040-1951. DOI: https://doi.org/10.1016/0040-1951(91)90158-O. URL: http://www.sciencedirect.com/science/article/pii/004019519190158O.

Rabbel, W., M. Kaban, and M. Tesauro (2013). "Contrasts of seismic velocity, density and strength across the Moho". In: *TECTONOPHYSICS* 609. Moho: 100 years after Andrija Mohorovicic, pp. 437 –455. ISSN: 0040-1951. DOI: https://doi.org/10.1016/j.tecto.2013.06.020. URL: http://www.sciencedirect.com/science/article/pii/S0040195113003855.

Radivojević, M. et al. (2015). "Neogene to Quaternary basalts of the Jabal Eghei (Nuqay) area (south Libya): Two distinct volcanic events or continuous volcanism with gradual shift in magma composition?" In: *Journal of Volcanology and Geothermal Research* 293, pp. 57 –74. ISSN: 0377-0273. DOI: https://doi.org/10.1016/j.jvolgeores.2015.02.003. URL: http://www.sciencedirect.com/science/article/pii/S0377027315000360.

Reguzzoni, M. and D. Sampietro (2015). "GEMMA: An Earth crustal model based on GOCE satellite data". In: *INT J APPL EARTH OBS* 35. GOCE earth science applications and models(Based on the ESA GOCE solid earth workshop, 16-17 October 2012), pp. 31 –43. ISSN: 0303-2434. DOI: https://doi.org/10.1016/j.jag.2014.04.002. URL: http://www.sciencedirect.com/science/article/pii/S0303243414000865.

Reguzzoni, M., D. Sampietro, and F. Sansò (2013). "Global Moho from the combination of the CRUST2.0 model and GOCE data". In: *Geophysical Journal International* 195.1, pp. 222–237. ISSN: 0956-540X. DOI: 10.1093/gji/ggt247. eprint: http://oup.prod.sis.lan/gji/article-pdf/195/1/222/17052527/ggt247.pdf. URL: https://dx.doi.org/10.1093/gji/ggt247.

Reigber, C., P. Schwintzer, and H. Lühr (1999). "The CHAMP geopotential mission". In: *Boll. Geof. Teor. Appl* 40, pp. 285–289.

Rihm, R. (1984). "Seismische Messungen im Roten Meer und ihre Interpretation". PhD thesis. Inst. für Geophysik Univ. Hamburg.

Rihm, R., J. Makris, and L. Moller (1991). "Seismic surveys in the Northern Red Sea: asymmetric crustal structure". In: *TECTONOPHYSICS* 198.2. Red Sea: Birth and Early History of a New Oceanic Basin, pp. 279 –295. ISSN: 0040-1951. DOI: https://doi.org/10.1016/0040-1951(91)90156-M. URL: http://www.sciencedirect.com/science/article/pii/004019519190156M.

Rodriguez, E., C. S. Morris, and J. E. Belz (2006). "A global assessment of the SRTM performance". In: *PHOTOGRAMM ENG REM S* 72.3, pp. 249–260.

Rummel, R. (2015). "GOCE: gravitational gradiometry in a satellite". In: *Handbook of Geomathematics*, pp. 211–226.

Said, R. (1962). *The GEOLOGY of Egypt*. Eisvier, Amsterdam-New York.

Salah, M. K. (2011). "Crustal structure beneath Kottamiya broadband station, northern Egypt, from analysis of teleseismic receiver functions". In: *J AFR EARTH*

SCI 60.5, pp. 353 –362. ISSN: 1464-343X. DOI: https://doi.org/10.1016/j.jafrearsci.2011.04.002. URL: http://www.sciencedirect.com/science/article/pii/S1464343X11000902.

Saleh, S. (2012). "3D crustal structure and its tectonic implication for nile delta and greater cairo regions, egypt, from geophysical data". In: *ACTA GEOD GEOPHYS HU* 47.4, pp. 402–429. DOI: https://doi.org/10.1556/AGeod.47.2012.4.3. eprint: https://doi.org/10.1556/AGeod.47.2012.4.3. URL: https://doi.org/10.1556/AGeod.47.2012.4.3.

Saleh, S. et al. (2006). "Crustal evaluation of the northern Red Sea rift and Gulf of Suez, Egypt from geophysical data: 3-dimensional modeling". In: *J AFR EARTH SCI* 45.3, pp. 257 –278. ISSN: 1464-343X. DOI: https://doi.org/10.1016/j.jafrearsci.2006.02.001. URL: http://www.sciencedirect.com/science/article/pii/S1464343X06000343.

Sampietro, D., A. H. Mansi, and M. Capponi (2018a). "A New Tool for Airborne Gravimetry Survey Simulation". In: *GEOSCIENCES* 8.8, pp. 292–301. DOI: https://doi.org/10.3390/geosciences8080292. URL: http://www.mdpi.com/2076-3263/8/8/292/htm.

— (2018b). "Moho Depth and Crustal Architecture Beneath the Levant Basin from Global Gravity Field Model". In: *GEOSCIENCES* 8.6, pp. 200–214. ISSN: 2076-3263. DOI: https://doi.org/10.3390/geosciences8060200. URL: http://www.mdpi.com/2076-3263/8/6/200.

Sampietro, D. et al. (2016). "GTE: a new software for gravitational terrain effect computation: theory and performances". In: *PURE APPL GEOPHYS* 173.7, pp. 2435–2453. ISSN: 1420-9136. DOI: https://doi.org/10.1007/s00024-016-1265-4. URL: https://doi.org/10.1007/s00024-016-1265-4.

Sampietro, D. et al. (2017). "Space-Wise approach for airborne gravity data modelling". In: *J GEODESY* 91.5, pp. 535–545. ISSN: 1432-1394. DOI: https://doi.org/10.1007/s00190-016-0981-y. URL: https://doi.org/10.1007/s00190-016-0981-y.

Sansò, F. and M. G. Sideris (2016). *Geodetic boundary value problem: the equivalence between Molodensky's and Helmert's solutions*. Springer.

Santosh, M. (2010). "Assembling North China Craton within the Columbia supercontinent: The role of double-sided subduction". In: *Precambrian Research* 178.1, pp. 149 –167. ISSN: 0301-9268. DOI: https://doi.org/10.1016/j.precamres.2010.02.003. URL: http://www.sciencedirect.com/science/article/pii/S0301926810000446.

Schaeffer, A. J. and S. Lebedev (2013a). "Global shear speed structure of the upper mantle and transition zone". In: *GEOPHYS J INT* 194.1, pp. 417–449. DOI: https://doi.org/10.1093/gji/ggt095. URL: http://dx.doi.org/10.1093/gji/ggt095.

— (2013b). "Global shear speed structure of the upper mantle and transition zone". In: *Geophysical Journal International* 194.1, pp. 417–449. ISSN: 0956-540X. DOI: 10.1093/gji/ggt095. eprint: http://oup.prod.sis.lan/gji/article-pdf/194/1/417/5898775/ggt095.pdf. URL: https://dx.doi.org/10.1093/gji/ggt095.

Schmidt, S., L. Barrio-Alvers, and H.-J. Götze (2015). *IGMAS+: Interactive Geophysical Modelling ASistant. Software tutorial*.

Schmidt, S. et al. (2010). "IGMAS+: a new 3D gravity, FTG and magnetic modeling software". In: *GEO-INFORMATIK Die Welt im Netz, edited by: Zipf, A. and Behncke,*

K. and Hillen, F. and Scheffermeyer, J. and Akademische Verlagsgesellschaft AKA GmbH, Heidelberg, Germany, pp. 57–63.

Sebai, A. et al. (2006). "Anisotropic structure of the African upper mantle from Rayleigh and Love wave tomography". In: *Physics of the Earth and Planetary Interiors* 155.1, pp. 48 –62. ISSN: 0031-9201. DOI: https://doi.org/10.1016/j.pepi.2005.09.009. URL: http://www.sciencedirect.com/science/article/pii/S0031920105002281.

Seber, D. et al. (2000). "Design and development of information systems for the geosciences: an application to the Middle East". In: *GEOARABIA* 5.2, pp. 269–296.

Sebera, J. et al. (2014). "Iterative Spherical Downward Continuation Applied to Magnetic and Gravitational Data from Satellite". In: *Surveys in Geophysics* 35.4, pp. 941–958. ISSN: 1573-0956. DOI: 10.1007/s10712-014-9285-z. URL: https://doi.org/10.1007/s10712-014-9285-z.

Segev, A. et al. (2006). "The structure, isostasy and gravity field of the Levant continental margin and the southeast Mediterranean area". In: *TECTONOPHYSICS* 425.1, pp. 137 –157. ISSN: 0040-1951. DOI: https://doi.org/10.1016/j.tecto.2006.07.010. URL: http://www.sciencedirect.com/science/article/pii/S0040195106003611.

Shih, H.-C. et al. (2015). "High-resolution gravity and geoid models in Tahiti obtained from new airborne and land gravity observations: data fusion by spectral combination". In: *Earth, Planets and Space* 67.1, p. 124.

Sicilia, D. et al. (2008). "Upper mantle structure of shear-waves velocities and stratification of anisotropy in the Afar Hotspot region". In: *Tectonophysics* 462.1. Seismic Anisotropy and Geodynamics of the Lithosphere-Asthenosphere System, pp. 164 –177. ISSN: 0040-1951. DOI: https://doi.org/10.1016/j.tecto.2008.02.016. URL: http://www.sciencedirect.com/science/article/pii/S0040195108003673.

Silva, J. B. C., D. F. Santos, and K. P. Gomes (2014a). "Fast gravity inversion of basement relief". In: *Geophysics* 79.5, G79–G91. DOI: https://doi.org/10.1190/geo2014-0024.1. eprint: https://doi.org/10.1190/geo2014-0024.1. URL: https://doi.org/10.1190/geo2014-0024.1.

— (2014b). "Fast gravity inversion of basement relief". In: *Geophysics* 79.5, G79–G91. DOI: 10.1190/geo2014-0024.1. eprint: https://doi.org/10.1190/geo2014-0024.1. URL: https://doi.org/10.1190/geo2014-0024.1.

Sobh, M. et al. (2018). "Regional Gravity Field Model of Egypt Based on the Satellite and Ground-Based Data". In: *PURE APPL GEOPHYS* 2018, pp. 1–20. DOI: https://doi.org/10.1007/s00024-018-1982-y. URL: https://link.springer.com/article/10.1007\%2Fs00024-018-1982-y.

Sobh, M. et al. (2019). "Inverse and 3D forward gravity modelling for the estimation of the crustal thickness of Egypt". In: *Tectonophysics* 752, pp. 52 –67. ISSN: 0040-1951. DOI: https://doi.org/10.1016/j.tecto.2018.12.002. URL: http://www.sciencedirect.com/science/article/pii/S0040195118304153.

Stern, R. J. and D. W. Scholl (2010). "Yin and yang of continental crust creation and destruction by plate tectonic processes". In: *International Geology Review* 52.1, pp. 1–31. DOI: 10.1080/00206810903332322. eprint: https://doi.org/10.1080/00206810903332322. URL: https://doi.org/10.1080/00206810903332322.

Stern, R. J. et al. (1994). "Precambrian basement around Wadi Halfa, Sudan: a new perspective on the evolution of the East Saharan Craton". In: *Geologische Rundschau* 83.3, pp. 564–577. ISSN: 1432-1149. DOI: 10.1007/BF01083228. URL: https://doi.org/10.1007/BF01083228.

Stixrude, L. and C. Lithgow-Bertelloni (2005). "Thermodynamics of mantle minerals — I. Physical properties". In: *Geophysical Journal International* 162.2, pp. 610–632. ISSN: 0956-540X. DOI: 10.1111/j.1365-246X.2005.02642.x. eprint: http://oup.prod.sis.lan/gji/article-pdf/162/2/610/5963861/162-2-610.pdf. URL: https://dx.doi.org/10.1111/j.1365-246X.2005.02642.x.

Szwillus, W., J. Ebbing, and N. Holzrichter (2016). "Importance of far-field topographic and isostatic corrections for regional density modelling". In: *GEOPHYS J INT* 207.1, pp. 274–287. DOI: https://doi.org/10.1093/gji/ggw270. URL: http://dx.doi.org/10.1093/gji/ggw270.

Taadiniyah, Hayah al-Misriyah al-Ammah lil-Misahah al-Jiyulujiyah wa al Mashruaat al (1981). *Geologic map of Egypt*. English. Map; Map/Single map.

Tahir, N. El et al. (2013). "Crustal structure of the Khartoum Basin, Sudan". In: vol. 593, pp. 151 –160. DOI: https://doi.org/10.1016/j.tecto.2013.02.032. URL: http://www.sciencedirect.com/science/article/pii/S004019511300142X.

Tapley, B. D. et al. (2004). "The gravity recovery and climate experiment: Mission overview and early results". In: *Geophysical Research Letters* 31.9.

Tealeb, A. A., A. A. Gharib, and A. I. Hussein (2003). "Crustal and upper mantle structure beneath Al-Fayum short-period station from spectral analysis of P-wave amplitude ratios". In: *NRIAG-JAG* 2.1, pp. 27–49.

Thorpe, R. S. and K. Smith (1974). "Distribution of Cenozoic volcanism in Africa". In: *Earth and Planetary Science Letters* 22.1, pp. 91 –95. ISSN: 0012-821X. DOI: https://doi.org/10.1016/0012-821X(74)90068-5. URL: http://www.sciencedirect.com/science/article/pii/0012821X74900685.

Tokam, A.-P. K. et al. (2010). "Structure of the crust beneath Cameroon, West Africa, from the joint inversion of Rayleigh wave group velocities and receiver functions". In: *Geophysical Journal International* 183.2, pp. 1061–1076. ISSN: 0956-540X. DOI: 10.1111/j.1365-246X.2010.04776.x. eprint: http://oup.prod.sis.lan/gji/article-pdf/183/2/1061/17361199/183-2-1061.pdf. URL: https://dx.doi.org/10.1111/j.1365-246X.2010.04776.x.

Toteu, S. F. et al. (2006). "U–Pb dating of plutonic rocks involved in the nappe tectonic in southern Cameroon: consequence for the Pan-African orogenic evolution of the central African fold belt". In: *Journal of African Earth Sciences* 44.4. The Precambrian of Central Africa, pp. 479 –493. ISSN: 1464-343X. DOI: https://doi.org/10.1016/j.jafrearsci.2005.11.015. URL: http://www.sciencedirect.com/science/article/pii/S1464343X05002141.

Tscherning, C. C. (1985). "Local approximation of the gravity potential by least squares collocation". In: *Proc, Int. Summer School on Local Gravity Field Approximation*, pp. 277–362.

— (1992). "The GRAVSOFT package for geoid determination". In: *Proc 1st IAG Continental Workshop of the Geoid in Europe, Prague, 1992*.

Tugume, F. et al. (2013). "Crustal shear wave velocity structure and thickness for Archean and Proterozoic terranes in Africa and Arabia from modeling receiver functions, surface wave dispersion, and satellite gravity data". In: *Tectonophysics* 609, pp. 250–266.

Uieda, L. and V. C. F. Barbosa (2017). "Fast nonlinear gravity inversion in spherical coordinates with application to the South American Moho". In: *GEOPHYS J INT* 208.1, pp. 162–176. DOI: https://doi.org/10.1093/gji/ggw390. URL: http://dx.doi.org/10.1093/gji/ggw390.

Uieda, L., V. C. F. Barbosa, and C. Braitenberg (2016). "Tesseroids: Forward-modeling gravitational fields in spherical coordinatesTesseroids: Modeling in spherical coordinates". In: *Geophysics* 81.5, F41. DOI: https://doi.org/10.1190/geo2015-0204.1. URL: http://dx.doi.org/10.1190/geo2015-0204.1.

Walker, W. S., J. M. Kellndorfer, and L. E. Pierce (2007). "Quality assessment of SRTM C-and X-band interferometric data: Implications for the retrieval of vegetation canopy height". In: *Remote Sensing of Environment* 106.4, pp. 428–448.

Watson, G. N. (1995). *A treatise on the theory of Bessel functions*. Cambridge university press.

Webb, S. J. et al. (2004). "Gravity modeling of Bushveld Complex connectivity supported by Southern African Seismic Experiment results". In: *S AFR J GEOL* 107.1-2, p. 207. DOI: https://doi.org/10.2113/107.1-2.207. URL: http://dx.doi.org/10.2113/107.1-2.207.

Wilson, M. and R. Guiraud (1992). "Magmatism and rifting in Western and Central Africa, from Late Jurassic to Recent times". In: *Tectonophysics* 213.1. Geodynamics of Rifting, Volume II Case History Studies on Rifts: North and South America and Africa, pp. 203 –225. ISSN: 0040-1951. DOI: https://doi.org/10.1016/0040-1951(92)90259-9. URL: http://www.sciencedirect.com/science/article/pii/0040195192902599.

Yang, J.-H. et al. (2008). "Mesozoic decratonization of the North China block". In: *Geology* 36.6, pp. 467–470.

Yoder, C. F. et al. (1983). "Secular variation of Earth's gravitational harmonic J2 coefficient from Lageos and nontidal acceleration of Earth rotation". In: *Nature* 303.5920, p. 757.

Zaki, A. et al. (2018a). "Comparison of Satellite Altimetric Gravity and Global Geopotential Models with Shipborne Gravity in the Red Sea". In: *MAR GEOD* 41.3, pp. 258–269. DOI: https://doi.org/10.1080/01490419.2017.1414088. eprint: https://doi.org/10.1080/01490419.2017.1414088. URL: https://doi.org/10.1080/01490419.2017.1414088.

Zaki, A. et al. (2018b). "Validation of Recently Released GOCE-Based Satellite-Only Global Geopotential Models over the Red Sea Using Shipborne Gravity data". In: *B GEOFIS TEOR APPL* 59.3, pp. 267–284. DOI: https://doi.org/10.4430/bgta0242. URL: http://www3.ogs.trieste.it/bgta/pdf/bgta0242_Zaki.pdf.

Zhai, M.-G. and M. Santosh (2011). "The early Precambrian odyssey of the North China Craton: A synoptic overview". In: *Gondwana Research* 20.1. Precambrian geology and tectonic evolution of the North China Craton, pp. 6 –25. ISSN: 1342-937X. DOI: https://doi.org/10.1016/j.gr.2011.02.005. URL: http://www.sciencedirect.com/science/article/pii/S1342937X11000402.

Zhang, H.-F. et al. (2011). "Phanerozoic reactivation of the Archean North China Craton through episodic magmatism: Evidence from zircon U–Pb geochronology and Hf isotopes from the Liaodong Peninsula". In: *Gondwana Research* 19.2, pp. 446 –459. ISSN: 1342-937X. DOI: https://doi.org/10.1016/j.gr.2010.09.002. URL: http://www.sciencedirect.com/science/article/pii/S1342937X10001747.

Zhang, Z. et al. (2014). "Geophysical transect across the North China Craton: A perspective on the interaction between Tibetan eastward escape and Pacific westward flow". In: *Gondwana Research* 26.1, pp. 311 –322. ISSN: 1342-937X. DOI: https://doi.org/10.1016/j.gr.2013.07.004. URL: http://www.sciencedirect.com/science/article/pii/S1342937X1300230X.

Zhao, D. (2007). "Seismic images under 60 hotspots: Search for mantle plumes". In: *Gondwana Research* 12.4, pp. 335 –355. ISSN: 1342-937X. DOI: https://doi.org/10.1016/j.gr.2007.03.001. URL: http://www.sciencedirect.com/science/article/pii/S1342937X0700055X.

Zhao, G. and M. Zhai (2013). "Lithotectonic elements of Precambrian basement in the North China Craton: Review and tectonic implications". In: *Gondwana Research* 23.4, pp. 1207 –1240. ISSN: 1342-937X. DOI: https://doi.org/10.1016/j.gr.2012.08.016. URL: http://www.sciencedirect.com/science/article/pii/S1342937X12002936.